Engineering and Applied Science Theses & Dissertations

McKelvey School of Engineering

Winter 12-15-2016

Towards clinical photoacoustic imaging: developing next-generation endoscopy systems and exploring new contrast agents

Chiye Li
Washington University in St. Louis

Follow this and additional works at: https://openscholarship.wustl.edu/eng_etds

Part of the Engineering Commons

Recommended Citation

Li, Chiye, "Towards clinical photoacoustic imaging: developing next-generation endoscopy systems and exploring new contrast agents" (2016). *Engineering and Applied Science Theses & Dissertations*. 207.
https://openscholarship.wustl.edu/eng_etds/207

WASHINGTON UNIVERSITY IN ST. LOUIS

School of Engineering and Applied Sciences
Department of Biomedical Engineering

Dissertation Examination Committee:
Lihong V. Wang, Chair
Samuel Achilefu
Mark A. Anastasio
James G. Miller
Lan Yang

Towards Clinical Photoacoustic Imaging: Developing Next-generation Endoscopy Systems and

Exploring New Contrast Agents

by
Chiye Li

A dissertation presented to
The Graduate School
of Washington University in
partial fulfillment of the
requirements for the degree
of Doctor of Philosophy

December 2016
St. Louis, Missouri

Table of Contents

List of Figures

iii

iv

<u>Acknowledgments</u>

I would like to express my sincere gratitude to my advisor, Professor Lihong Wang, for his guidance and inspiration during my Ph.D. study. I gratefully thank my colleagues in Optical Imaging Laboratory for their assistance with this work. My thanks also go to Professor James Ballard, who helped me edit my research manuscripts.

Chiye Li

Washington University in St. Louis

December 2016

ABSTRACT OF THE DISSERTATION

Towards Clinical Photoacoustic Imaging: Developing Next-generation Endoscopy Systems and

Exploring New Contrast Agents

by

Chiye Li

Doctor of Philosophy in Biomedical Engineering

Washington University in St. Louis, 2016

Professor Lihong Wang, Chair

Photoacoustic imaging holds great clinical promise because it achieves high-resolution tomographic imaging at depths. Moreover, its strong spectroscopic imaging capability provides a wealth of molecular and functional information based on. Still, despite recent advances, existing photoacoustic systems cannot be readily applied in the clinical environment. This dissertation aims to push the frontier of clinical photoacoustic imaging from both technological and applicational perspectives.

The first part of this dissertation describes the development of photoacoustic endoscopy (PAE) systems for imaging human Barrett's esophagus and studying preterm birth. We have developed optical resolution-PAE, which significantly improved lateral resolutions, laparoscopic-PAE, which can guide minimally-invasive surgeries, and catheter-based-PAE, which opens up new opportunities to image the human esophagus. For each system, we tested and optimized the imaging performance in phantom and animal experiments, and then validated them in humans.

The second part of the dissertation describes advanced photoacoustic imaging aided by contrast agents. Specifically, gold nanoparticles were used to quantify biological diffusion

photoacoustically. In addition, ion nanosensors were applied for continuously monitoring therapeutic lithium concentration in deep tissue *in vivo*.

Chapter 1: Introduction

1.1 Photoacoustic Endoscopy

Photoacoustic tomography (PAT) is performed by detecting the acoustic wave generated through photoacoustic (PA) effect from laser-irritated light absorbers and the reconstruction of the absorbers' distribution. By choosing the appropriate laser illumination wavelength, many physiological and biological constituents can be differentiated, and many types of functional parameters also can be measured through an endogenous contrast mechanism [1]. Moreover, a variety of exogenous contrast agents and multi-functional molecular probes can be used to visualize specific structures or biomarkers [2,3]. PAT can acquire important physiological parameters such as hemoglobin concentration, oxygen saturation of hemoglobin, blood flow speed, and metabolic rate of oxygen [4]. This information from PAT can contribute to detection and diagnosis of disease, especially to those of cancer. It has been demonstrated that glucose metabolism and micro-hemodynamics can be monitored *in vivo* [1,4]. As many neoplasms are associated with angiogenesis and show abnormal metabolic rates, the disease-relevant information provided by PAT can potentially facilitate accurate diagnoses.

Photoacoustic endoscopy (PAE) embodies a PAT system in a miniaturized probe to enable high-resolution imaging of internal organs [5]. It has been used to provide structural and functional information by visualizing blood vasculature as well as dye-labeled lymph nodes and vessels in the gastrointestinal tract [6–8] *in vivo*.

So far, many imaging modalities have been investigated in various endoscopic areas [9,10]. However, the development of associated PAE devices is still at an immature stage because of technical challenges. Unlike existing ultrasound (US) [11] or optical endoscopic probes [12], PAE requires the integration of both optical and acoustic elements in a small space. Also, in the case of a single element-based mechanical scanning endoscope, its internal space must be filled with an acoustic matching medium whose acoustic and optical properties must be considered carefully. Such requirements present challenges in the development of a suitable probe.

1.2 Motivation

Diseases of internal organs are difficult to visualize or exam by non-ionizing radiation from outside, which has limited penetration depth in biological tissue. Therefore, endoscopic imaging devices are needed. Colorectal cancer is the third most common cancer in males and second in females. As to uterine cancer, the prevalence of cervix uteri cancer ranks third and corpus uteri ranks six among all types of cancers in the female patients. It is estimated that there are 1.2 million new cases of colorectal cancer and 600 thousands deaths in 2008 [13]. Mortality rates continue to increase in some countries that have limited resources. As people live longer, cancer will become a worse public health problem. Diagnosis at early stage would reduce the possibility of death. Novel imaging is in need to image and characterize diseases of internal organs for precise assessment and early diagnosis.

Tumor tissue has distinctive structures and a reprogrammed metabolism, replacing those in normal tissue, in order to most effectively support its intensive physiological operations. One well-known characteristic structure is angiogenesis, which initiates early during the tumor development and is believed to be a hallmark of cancer [14]. Blood vessels supplying tumor are

usually marked by convoluted and excessive vessel branching, tortuous and enlarged vessels, differentiating them from their normal counterparts. Sometimes it is accompanied by microhemorrhages and leakiness [15]. The alternative metabolism includes switching or fluctuation in nutrient fueling, oxygen transportation and consumption [16,17]. Other changes induced by neoplastic proliferation include the collapse of intratumoral lymphatic vessels and growth of the lymphatics at the peripheries of tumors [14]. Because of its spectroscopic and angiographic imaging ability, photoacoustic imaging, especially photoacoustic endoscopy, could be a powerful tool in tumor study. In addition to tumor site and size, different vascular structure may be used to distinguished adenomas and carcinomas by their different growth patterns, rates of development, and degrees of maturity.

Preterm birth, with a 9.6% rate in the United States [18], is the leading cause of perinatal morbidity and mortality. Premature cervix remodeling is believed to contribute to preterm birth [19]. Assessment of cervix will help us understand the causes of preterm birth and also provide clinical diagnostic evidence. High-resolution endoscopic imaging technologies that obtain anatomic, functional, and metabolic information about the cervical microenvironment will permit early detection of preterm birth.

Chapter 2: Photoacoustic Endoscopy Systems

2.1 Proximally Actuated Urogenital Photoacoustic Endoscopy System

Background Because of the inadequacy of current tools and techniques for diagnosing diseases of urogenital diseases [20], such as endometrial cancer, cervical cancer, and prostate cancer, more effective means are desired to achieve accurate medical assessments.

In recent years, a number of miniaturized PA imaging probes have been reported for various endoscopic applications, such as intravascular [10], urogenital [21,22], and gastrointestinal tract [7] imaging. Among them, however, only two imaging probes that use a micromotor-based mechanical scanning mechanism have demonstrated *in vivo* imaging with fully encapsulated probe implementations and suitable diameters for endoscopy [7,8]; other imaging probes are not fully encapsulated and/or have not demonstrated *in vivo* imaging. However, the imaging probes reported in Refs. [7,8] may not be suited for clinical urogenital imaging due to their nonrigidity and slow imaging speed (4 Hz).

The diameter of endoscopic probes for imaging the uterus or prostate are not tightly restricted, as various forms of large-diameter ultrasound probes (usually ~1 cm in diameter) are widely used for many urogenital disease diagnoses in a stand-alone form [23], i.e., without the incorporation with a video endoscopic function. In this study, seeking to apply PAE for diagnosing urogenital diseases, we have implemented a new endoscopic probe with improved imaging speed and a specifically designed probe structure. The key strategy was to use parabolic acoustic reflector-

4

based mechanical scanning with a proximal actuation mechanism, and construct the probe with a durable and safe structure.

Methods   Figure 2.1(a) shows photos of the side-viewing PA endoscopic probe. The entire endoscopic probe is rigid for convenient handling, and a dome-shaped distal end enables smooth cavity introduction. To encapsulate all endoscope components, we fabricated the probe housing from a medical-grade stainless steel tube (MicroGroup) with an outer diameter of 12.7 mm and a length of ~50 cm. For the mechanical scanning, we employ a scanning head comprised of two key components, a parabolic acoustic reflector (10 mm diameter, nickel substrate, Optiforms) and an optical prism (3 mm diameter, altered from #45-525, Edmund). The scanning head is actuated by a step motor located at the proximal end. The parabolic reflector enables acoustic focusing with a lower geometric aberration than our previous acoustic lens-based focusing method [7,8], while providing a high acoustic numerical aperture (~0.48). Via the prism and parabolic reflector, laser pulses and acoustic waves are delivered coaxially to achieve an efficient overlap of the illumination and acoustic detection over a large depth range.

An ultrasonic (US) transducer (LiNbO$_3$, ~40 MHz, unfocused) generates US pulses and detects both PA and US pulse-echo signals. The US transducer's piezo-element is a ring with an outer diameter of 8 mm and an inner diameter of 3 mm. The inner diameter matches the diameter of the round optical prism located at the center of the parabolic reflector [Figure 2.1(a)]; reducing the transducer's surface area is also beneficial to the electric impedance matching between the transducer and a signal amplifier. To support the US transducer, we fabricated a bridge-shape stainless steel frame and mounted the transducer at the distal end of the frame. The US transducer's signal wire (~1 mm thick) passes through the stainless steel bridge, along the 50 cm long probe housing, and is statically connected to a US pulser-receiver (5072PR, Olympus).

5

Because of the bridge section, the angular field-of-view (FOV) of the endoscope is partially blocked, by ~100°.
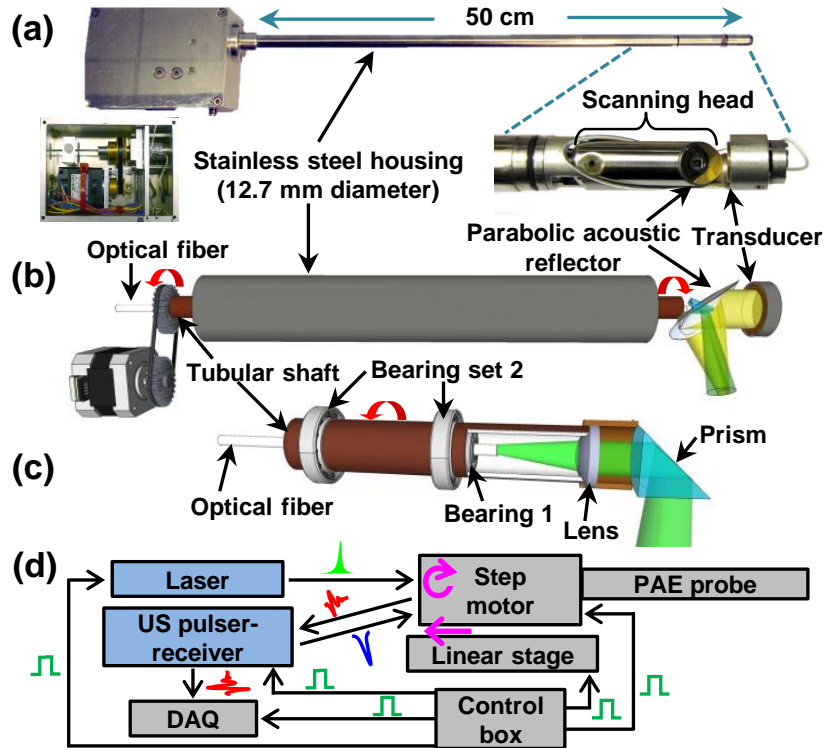
Figure 2.1. Photo **(a)** and schematic **(b)** of the PA endoscopic probe developed for human urogenital system imaging. **(c)** Schematic of the rotary junction (Bearing 1) and light guiding optics. **(d)** Block diagram showing the peripheral systems.

In Figure 2.1(b), we present a schematic to illustrate the principle of the mechanical scanning and the configuration of the optical and acoustic components. Inside the stainless steel housing, we coaxially placed a tubular rigid shaft to transfer mechanical torque to the scanning head. However, inside the tubular shaft, we placed a multimode optical fiber (UM22-600, Thorlabs) which is positioned statically along the axis of the endoscope. Thus, only the tubular shaft rotates between the housing and the innermost optical fiber. The main advantage of employing the tubular shaft is that it permits torque transmission without mechanical jitter and eventually enables rotational scanning with a uniform angular step size for the scanning mirror. Also, by

6

employing a step motor that can provide fast and stable rotation, the endoscope achieves much faster mechanical scanning than previous micromotor-based endoscopes.

As shown in Figure 2.1(c), we formed a rotary junction (i.e., Bearing 1) near the coupling point between the tubular shaft and scanning head [Figure 2.1(a)] to provide a free rotation only to the scanning head, separating it from the optical fiber. The center position of the shaft to the probe housing is sustained by multiple ball bearings (Bearing set 2) placed at the space between the housing and the shaft, over the 50 cm long tubular section; Bearing 1 placed inside the shaft is necessary to make the optical fiber static. Hence, an optical lens (#65-270, Edmund) and the prism inside the scanning head rotate together during the mechanical scanning. Given the optical configuration, the laser beam diameter for PA imaging is ~2.3 mm when it passes through an optically and acoustically transparent polyethylene terephthalate membrane (103-0227, Advanced Polymers). The membrane forms an imaging window and seals the inner cavity of the endoscope, which is filled with de-ionized water. As laser beams are sent to target tissue without optical focusing, the endoscope's spatial resolution is determined by the geometry of the parabolic reflector and acoustic parameters of the US transducer. For this prototype imaging probe, we set the working distance at ~3.5 mm apart from the probe surface to image endometrial cancer in the uterus, which typically has a wall thickness of ~10 mm.

Figure 2.1(d) shows the endoscope's peripheral systems, comprised of a light source, a US pulser-receiver, and a data acquisition (DAQ) system. The light source is a solid-state, diode-pumped Nd:YVO$_4$ laser (INNOSLAB IS811-E, EdgeWave) providing a 532 nm wavelength (~5 ns pulse width). For PA imaging, laser pulses are coupled to the endoscope's multimode optical fiber (~5 m), which is extended to the distal end of the probe [Figure 2.1(b)]. After exiting the optical fiber, they are reflected by the prism and sent to the target tissue to generate PA signals.

We applied the total internal reflection effect, and, to maintain the effect after the chamber is filled with acoustic coupling water, we sealed a thin air layer outside the hypotenuse of the prism. The generated PA waves reflected by the parabolic reflector are detected by the US transducer. To record PA and US signals, we utilize a high-speed digitizer (PCI-5124, National Instruments). We also constructed a control box using a multifunction data acquisition card (PCI-6221, National Instruments) to control and synchronize the peripheral systems. Considering the large probe diameter of 12.7 mm, we record 800 A-lines per B-scan, which yields an angular step size of 0.45° for the scanning mirror.
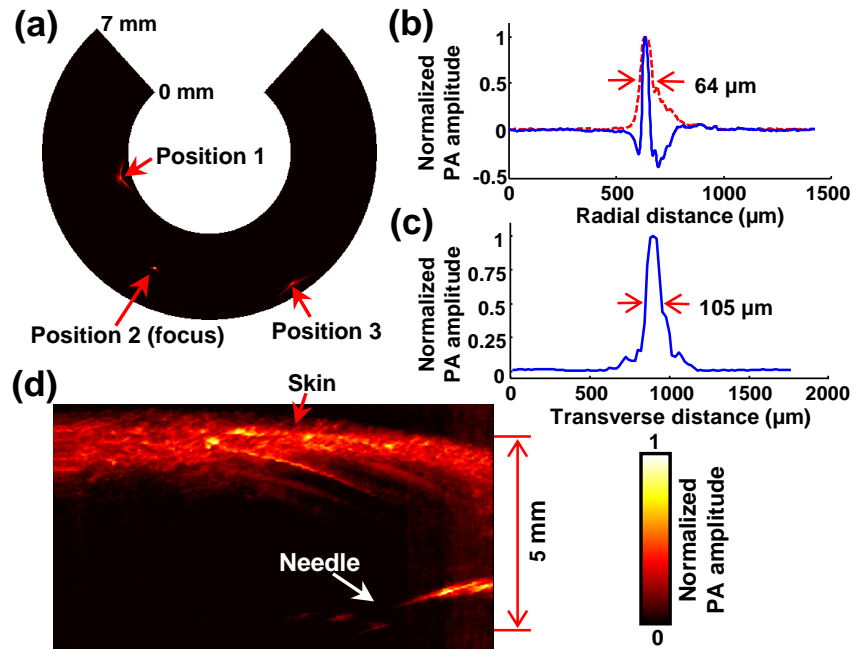
Figure 2.2. **(a)** PA B-scan image of the 20 µm thick tungsten wire imaged at three locations. **(b)** Typical PA A-line signal (blue) and its Hilbert-transformed signal (i.e., radial LSF) for the tungsten wire target located at the focal point (Position 2). **(c)** Corresponding transverse LSF of the tungsten wire. **(d)** PA image of a black needle inserted into the inner leg of a rat.

Results We tested its imaging performance, including the scanning speed, spatial resolution, and imaging depth. Our endoscope's scanning speed could easily reach 22 Hz, thanks

to the capacity of the motor. In the imaging experiments to be presented later, however, we recorded data with a 6.25 Hz B-scan frame rate because of the limited pulse repetition rate of the laser system (5 kHz). For the resolution measurement, we utilized a ~20 μm thick tungsten wire as a target and imaged it at three different locations in a water medium; we imaged photoacoustically only because the US resolution relies on two-way acoustic focusing and can be inferred from the PA resolution. Since the imaged tungsten wire had a sufficient length with a diameter smaller than the endoscope's spatial resolution, the wire could be treated as a line target. For more accurate measurement of resolution, we recorded 50 B-scan images and then averaged them.

Figure 2.2(a) shows a PA B-scan image that includes the imaged tungsten wire at three different locations. As the target is moved away from the focus (i.e., Positions 1 and 3), the transverse resolution deteriorates. In Figures 2.2(b) and 2.2(c), we present radial and transverse line spread functions (LSFs) for the target located at the focal point (i.e., Position 2). Based on the LSFs, we determined the endoscope's spatial resolutions to be 64 μm and 105 μm in the radial and transverse directions, respectively. These experimental resolutions were worse than the theoretically estimated radial resolution [24] of 39 μm, and 65 μm transverse resolution predicted by Zemax (Radiant Zemax). We speculate that the discrepancies were caused by the distortion of acoustic waves by the optical prism placed at the center of the parabolic reflector. Figure 2.2(d) shows the endoscope's image penetration capability, which was determined by imaging a black needle (21 gauge) inserted into the inner leg of an adult Sprague Dawley rat (~450 g, Harlan) *in vivo*. As shown, the needle was clearly differentiated to a depth of more than 5 mm through the highly scattering tissue, highlighting the endoscope's eligibility for deep tissue imaging.

To demonstrate the endoscope's *in vivo* imaging ability, we imaged the colorectum of a New Zealand White rabbit (Harlan). The rabbit was fasted for ~12 hr before the experiment, to increase the likelihood of an empty colon for imaging. Prior to endoscopic imaging, we anesthetized the animal by injecting 15–25 mg/kg ketamine and 2–3 mg/kg xylazine intramuscularly. We cleansed the rabbit's colon with a saline laxative enema, and spread ultrasound gel into the colon for acoustic coupling. Then, we inserted the probe into the colon and performed endoscopic imaging with a B-scan imaging speed of 6.25 Hz and a laser pulse energy of 0.55 mJ at a 5 kHz repetition rate, which yielded an optical fluence of 13 mJ/cm^2 (65% of the ANSI safety limit at the tissue surface [25]). To achieve volumetric imaging, we recorded B-scan images during the constant pullback translation of the probe (200 μm/s) provided by a motorized translation stage. During the imaging procedure, the anesthesia level of the animal was maintained by continuously supplying ~1.5% isoflurane, and the vital signs were also monitored. After the imaging experiment, the rabbit was euthanized by a 150 mg/kg pentobarbital injection via the marginal ear vein.

Figure 2.3(a) shows a three-dimensionally rendered, coregistered PA and US image from the rabbit colorectum acquired *in vivo* over a scanning time of ~4.5 min. The image was processed from a volumetric data set acquired from a 27 mm diameter and 5.3 cm long image volume. In this experiment, we recorded only data corresponding to a 7 mm imaging depth because the transverse resolutions are degraded in the distant region from the focal point [Figure 2.2(a)]; the working distance is 3.5 mm from the probe surface. As shown in PA and US radial maximum amplitude projection (RMAP) images [Figures 2.3(b) and 2.3(c)], which were produced from the volumetric image [Figure 2.3(a)], the PA signals acquired at the 532 nm wavelength show vasculature distributed in the colorectum and adjacent organs, while the US signals reveal a

10

spine structure very clearly because of the high acoustic reflection caused by tissue density variation near the cavity wall. In Figures 2.3(d) and 2.3(e), we present two combined PA and US B-scan images selected from the marked positions in Figure 2.3(b). To produce the images, we applied time-gain compensation to more clearly visualize PA signals originating from greater depths. PA imaging shows the cross-sections of blood vessels distributed in the intestine wall, which was estimated to be ~1 mm thick, and detects PA signals from a depth of more than 6 mm.
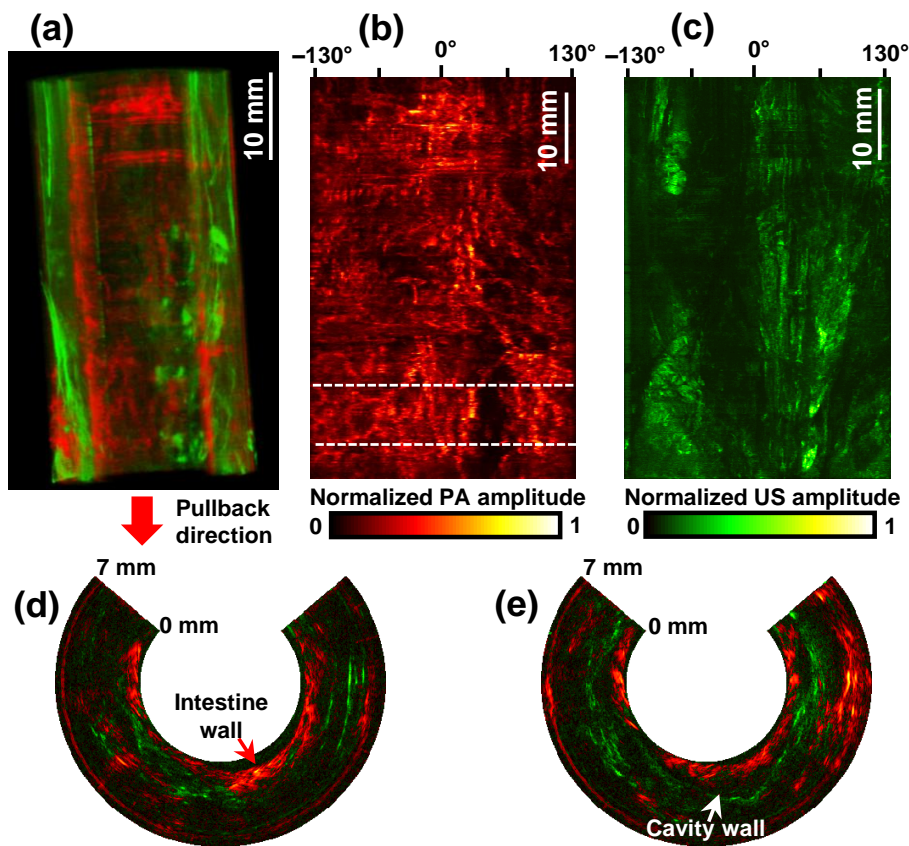
Figure 2.3. **(a)** Coregistered PA and US volumetric image from a rabbit colorectum acquired in *vivo* over a 53 mm range with a 27 mm image diameter. The lower portion of the image corresponds to the anus. **(b, c)** PA- and US-RMAP images of (a). **(d, e)** Representative combined PA and US B-scan images near the location indicated by the dashed line in (b).

Although the PA imaging experiment provided vasculature information in the colorectum, the imaged blood vessels were not clearly visualized as expected from the resolution values

11

presented in Figure 2.2. The endoscope's working distance was about 3.5 mm from the probe surface, while the blood vessels in the imaged colorectum were mostly distributed within ~2 mm of the probe surface [Figures 2.3(d) and 2.3(e)].

To demonstrate the endoscope's full vasculature resolving ability, we designed a simple experiment that imaged blood vessels positioned near the focal distance of the probe. Such an experimental circumstance was intentionally created by inserting a plastic tubular spacer (13 mm inner diameter, 2 mm wall thickness) around the endoscope's housing and then imaging blood vessels distributed on the large intestine surface of a rat which was surgically opened. A portion of the tubular spacer's wall which corresponded to the imaging window of the endoscope was opened to allow PA waves to pass through it, and the gap was filled with ultrasound gel. For this experiment, we utilized the same rat used in the imaging penetration test [Figure 2.2(d)] and performed the experiment *ex vivo* after euthanizing the animal (pentobarbital, 150 mg/kg, IP injection) to avoid distress and possible complications.

The photograph in Figure 2.4(a) shows the surface of the large intestine imaged by the PA endoscopic probe in concert with the spacer. As shown in the acquired PA-RMAP images [Figures 2.4(b) and 2.4(c)], the PA endoscope clearly mapped blood vessels in the intestine wall, as well as neighboring mesenteric tissues (scanning time: ~4 min). Apparent blood vessel diameters in the magnified images are much smaller than those in the PA-RMAP images acquired from the rabbit colorectum *in vivo* [Figure 2.3(b)] and estimated to be as small as ~140 μm, which is comparable with the experimentally quantified spatial resolution value [Figure 2.2] and makes the mesenteric blood vessel pair distinguishable. The angular FOVs of the images presented in Figures 2.4(b) and 2.4(c) are smaller than the actual FOV because a nearly-planar

surface was imaged. All procedures in the animal experiments followed protocols approved by the Institutional Animal Care and Use Committee at Washington University in St. Louis.
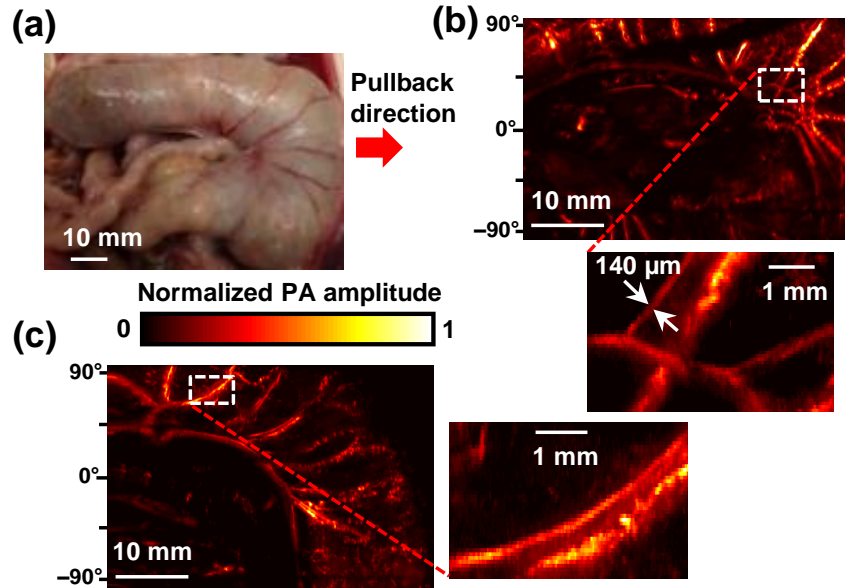
Figure 2.4. (a) Photo of the rat large intestine imaged *ex vivo*. **(b, c)** PA-RMAP images of (a). All the PA signals in the presented images are mapped on a linear scale.

Discussion   In this study, we designed and implemented a dual-mode PA and US rigid probe for comprehensive use in human urogenital imaging, and demonstrated its endoscopic workability through animal experiments. The endoscopic probe enabled simultaneous PA and US imaging with a B-scan frame rate of 6.25 Hz, which is currently limited by the pulse repetition rate of the laser system; we demonstrated that the mechanical rotation speed exceeds 20 Hz. Compared with our previous micromotor-based endoscopes [7,8], the main difference in the probe design is that the locations of the US sensor and mechanical actuation source are switched (Figure 2.1), while the static mounting strategy of the light delivery and acoustic detection units is maintained. By relocating the mechanical source to the proximal part, a space restriction for the motor was eliminated at the distal end; thereby we were able to use a more

13

powerful motor. Although the detailed endoscope's design needs to be modified for specific applications, the general design concept and scanning mechanism presented in this paper may be used for various other applications, such as a hand-held exterior or laparoscopic probe.

One disadvantage of this endoscope is the low depth of focus caused by the high acoustic numerical aperture. For this prototype, we aimed the focal distance at 3.5 mm which renders a poor spatial resolution near the probe surface. Applying the integrated optical- and acoustic-resolution imaging concept [22] could increase the transverse resolution over the entire radial imaging range. Our first clinical goal is to apply this endoscope for imaging uteri with endometrial cancers. As the endoscope provides PA images in a coregistered form with traditional US images, which are familiar to clinicians, it would enable more accurate medical assessments for urogenital diseases.

2.2 Optical-resolution Photoacoustic Endomicroscopy

Background Intravital microscopy (IVM) techniques [26,27] have been opening new research and clinical avenues by providing unprecedented image information on biological processes in vivo. In addition to earlier approaches that imaged the body surfaces of small animals, technical advances in miniaturized imaging devices have now enabled extending IVM to endomicroscopy, which enables the imaging of internal organs. So far, two-photon microscopy [28] and confocal microscopy [29] have been the major technical platforms for this approach. However, in most cases, these techniques are based on complex labeling with fluorescent molecules, which could disturb delicate biological processes. In this regard, PAT-based IVM offers several unique imaging features[5,30] as label-free functional imaging modality.

14

To realize optical-resolution PA IVM, an optical focusing unit must be embodied in a small imaging probe along with an ultrasound detection unit. So far, two groups have reported such endoscopic devices with optical focusing and demonstrated PA images with transverse resolutions of 19.6 μm and 15.7 μm, respectively [31,32]. However, the images were all limited to phantom experiments because the imaging probes were not fully encapsulated, which is crucial for IVM applications, especially for internal organ imaging. In this study, by applying the optical-resolution photoacoustic microscopy (OR-PAM) concept [33] to our recently developed PA endoscopic technique [7], we successfully implemented the first fully encapsulated optical-resolution photoacoustic endomicroscopy (OR-PAEM) system and demonstrated its IVM capability through an *in vivo* animal experiment.

Methods Figure 2.5 shows the OR-PAEM probe [Figures 1(a) and 1(b)] and associated system elements [Figures 2.5(b)–2.5(l)]. For this endomicroscope, we utilized a previously developed stainless steel (SS) tubular housing-based probe encapsulation method [6] as the backbone of the imaging probe [Figures 2.5(a) and 2.5(b)]. We also adopted the scanning mirror and built-in micromotor-based mechanical scanning mechanism [Figure 2.5(e)] because they enable easy integration of the optical and acoustical components and also provide stable mechanical scanning without the nonuniform rotational distortion, which frequently occurs in flexible shaft-based endoscopes [34]. Here, we applied the confocal optical illumination and acoustic detection methods for superior signal sensitivity. Further, to achieve optical-resolution PA imaging, we implemented a new structure for the optical illumination and acoustic detection unit [Figure 2.5(d)].

As shown in Figure 2.5(f), we placed a focused ultrasonic (US) ring transducer (3.0 mm O.D., f = 4.4 mm, 42 MHz, LiNbO3), fabricated through the press-focusing technique [35], inside a 3.4

mm diameter SS housing (altered from a 10 gauge, 200 μm wall thickness hypodermic SS tube, type 304) and then coaxially configured a 1.2-mm outer diameter gradient-index (GRIN) lens unit [Figure 2.5(g)] inside the transducer. The unit had an optical working distance of 6.5 mm in the water medium that filled the imaging probe. We chose the working distance by considering the large path length (3.6 mm) between the transducer and the plastic membrane (i.e., imaging window) at the given probe outer diameter of 3.8 mm, and the optical focal spot was confocally placed within the acoustic focal zone of the transducer, at ~0.8 mm outside the membrane surface. To accommodate the GRIN lens unit inside the transducer while maximizing the effective area of the piezo-electric element, we fabricated the transducer with stepped center hole diameters: a 1.3 mm hole for the installation of the GRIN lens and a 0.9 mm hole for the exit of the laser beam [Figure 2.5(i)].

As shown in Figure 2.5(g), the GRIN lens unit was enclosed in an SS tube (1.2 mm O.D., 1.0 mm I.D.; altered from a 17 gauge, 254 μm wall thickness hypodermic SS tube, type 304) and completely sealed with epoxy at both ends to avoid water permeation. To achieve the maximal optical numerical aperture (NA) at the given working distance, we utilized a custom ordered GRIN lens (0.20 pitch, GRINTECH GmbH) with a 0.5 mm outer diameter and 2.4 mm length. Inside the SS tube, the GRIN lens was coupled with a single-mode optical fiber (SM600, Thorlabs), which guided the laser beam from a light source. The distance between the optical fiber's tip and the beam entrance surface of the GRIN lens was set at 0.8 mm. This distance and the pitch of the GRIN lens were determined from a ZEMAX simulation. Importantly, we chose the above shown [Figure 2.5(g)], glass ferrule-based affixing method to assemble the GRIN lens and optical fiber, instead of directly attaching a GRIN lens with a different pitch, because it is not desirable to have any glued interface along the beam path or an intermediately formed

16

focused zone of the laser beam inside the GRIN lens, owing to the high laser energy flux with a high-pulse repetition rate. After completing the GRIN lens unit [Figure 2.5(g)], we analyzed the output beam profile using a beam profiler (SP620U, OPHIR Beam Gauge) and measured the FWHM-based beam diameter to be ~9.2 μm [Figure 2.5(i)] – this value yields a beam waist size (w_0) of 7.8 μm and an optical NA of ~0.022 under the assumption of a Gaussian beam.
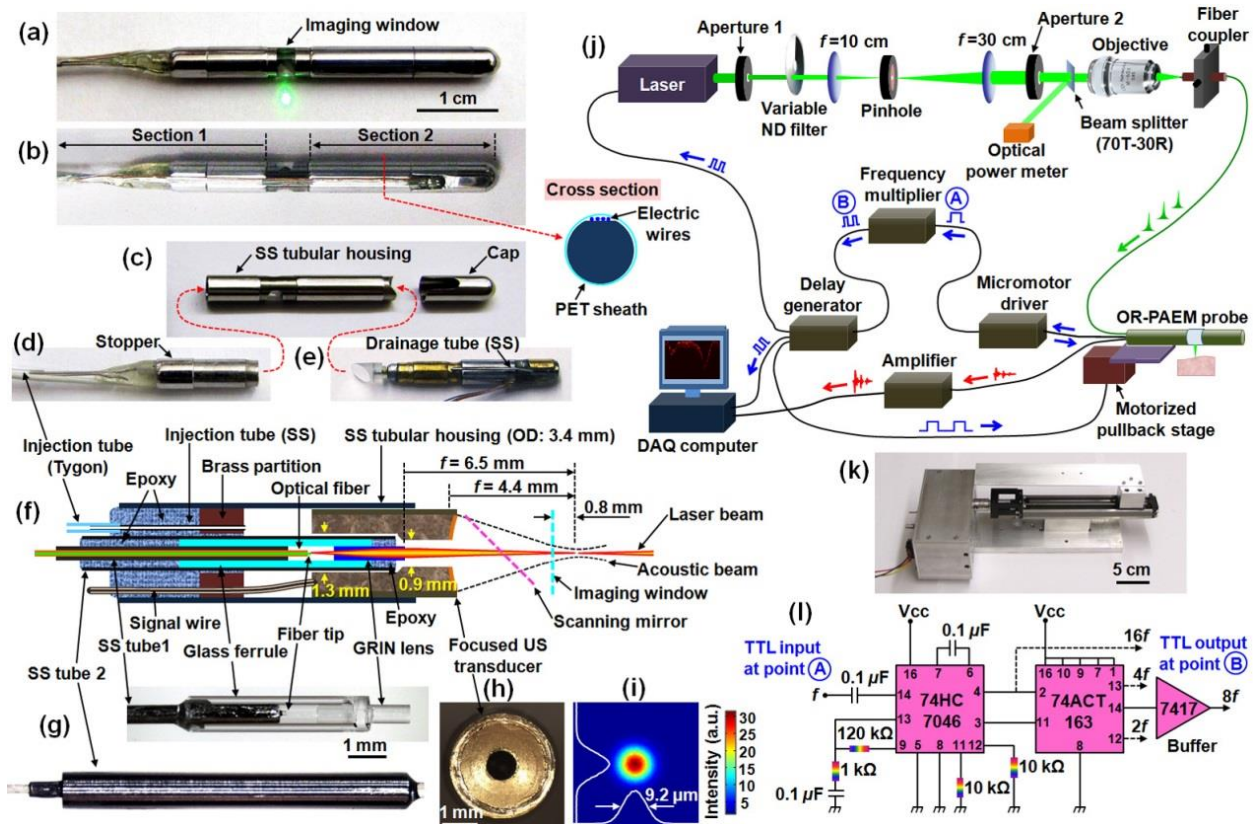
Figure 2.5. OR-PAEM probe and peripheral systems. **(a,b)** Photos of the OR-PAEM probe showing the imaging window side (a) and bridge side (b). **(c)** Photo of the SS tubular housing and distal cap. SS, stainless steel. **(d)** Photo of the optical illumination and acoustic detection unit. **(e)** Photo of the scanning mirror and micromotor unit. **(f)** Schematic of (d). The virtual locations of the scanning mirror and the plastic membrane (imaging window) are indicated by two colored dashed lines. **(g)** Photos of the GRIN lens unit before (upper) and after (lower) being enclosed by a SS tube 2. **(h)** Front view of the US transducer. **(i)** Laser beam intensity profile at the focal distance. **(j)** Schematic of the entire setup. **(k)** Motorized pullback stage. **(l)** Frequency multiplier circuit diagram.

17

In realizing the OR-PAEM probe, one of the most crucial processes was to provide acoustic matching for the inner cavity of the imaging probe to efficiently transmit generated PA waves to the US transducer. Unlike the flexible shaft-based proximal actuation mechanism, which delivers mechanical torque from an external source, the scanning mirror and built-in micromotor-based mechanical scanning mechanism advantageously solves the acoustic matching requirement because all the moving parts of the imaging probe are housed in an isolated space of the distal section [Figure 2.5(a)]. To provide acoustic matching inside the probe, we implemented the probe so that liquid could be injected – in this study, we utilized deionized water as the matching medium because it exhibits both high optical transparency and low acoustic attenuation for high-frequency acoustic waves. As shown in Figures 2.5(d) and 2.5(f), we installed a SS hypodermic tube (28 gauge, 76 µm wall thickness, ~2 cm length, type 304) at the base of the GRIN-lens and transducer unit for water injection, and also installed another SS hypodermic tube (30 gauge, ~1 cm length, 102 µm wall thickness, type 304) at a side of the mechanical unit for water drainage [Figure 2.5(e)], which will be explained later. The water injection SS tube is further extended by a ~50 cm long plastic tube (762 µm O.D., 254 µm I.D., Tygon) along the flexible body section. Thus, the flexible body section of the probe is comprised of the optical fiber (~2 m length), the water injection plastic tube (~50 cm length), the signal wire (38 AWG, 50 Ω, ~1 m length, New England Wire Technologies) of the transducer, the four electric wires of the micromotor (~2 m length), and an additional narrow diameter SS tubular stiffener (30 gauge, ~50 cm length) to reinforce the flexible body section. All of these components are then fully sheathed with a ~30 cm long polyethylene terephthalate (PET, Advanced Polymers) plastic tube (see section 1 in Figure 2.5(b)), with the procedure described below.

The overall structure of the probe and the water injection unit was similar to that of previous PAE probes. However, we improved the overall mechanical performance and the water injection function by modifying the related designs slightly. To fabricate the endomicroscope, we utilized standard size medical grade hypodermic SS tubes purchased from either MicroGroup or McMaster-Carr, and utilized several different medical grade adhesives with different viscosities and curing times, such as M-31CL (Loctite), Loctite 4014 (Loctite), and DP-125 (3M). To form the imaging window of the endomicroscope [Figure 2.5(a)], we utilized a PET heat shrink tube (140150CST, 3.56 mm average expanded diameter, 38 μm wall thickness, Advanced Polymers) because it exhibits good optical and acoustic transparency and also is relatively easy to glue compared to other plastic materials. We used an ordinary UV-curing optical adhesive (NOA68, Norland Products, purchased from Thorlabs) to seal the gap between the tubular imaging window and the SS housing. To form the metal housing of the endomicroscope [Figure 2.5(c)], we utilized 9 gauge (178 μm wall thickness) and 10 gauge (254 μm wall thickness for the imaging window section and 203 μm wall thickness for the mechanical unit adapter installed at the tip of the housing) SS hypodermic tubes (type 304).

For PA imaging, we developed peripheral systems as shown in Figure 2.5(j). We utilized a Q-switched diode-pumped Nd:YAG laser (SPOT 10-200-532, Elforlight) that provided a 532-nm wavelength with a pulse duration of ~1 ns. A portion of the laser beam was selected by an aperture (1.3 mm diameter) and a variable neutral density (ND) filter (NDC-50C-4, Thorlabs), then focused into a 50-μm diameter pinhole (#59-261, Edmund) by a convex lens (f = 10 cm) for spatial filtering. After the filtration, the beam was collimated by a convex lens (f = 30 cm), further shaped by an aperture (4.0 mm diameter), and focused into the input of the endomicroscope's optical fiber by a 10× objective lens. Finally, to generate PA waves, the beam

19

was delivered to the target tissue via the optical fiber, the GRIN lens, and the scanning mirror. Once PA waves were generated, some of them were reflected by the same mirror, sent to the transducer, converted into electrical signals, amplified by an amplifier (5073PR, Panametrics), and digitally recorded by a data acquisition (DAQ) card (200 MHz, NI PCI-5124, National Instruments). Throughout the experiments, the output energy of laser beam at the GRIN lens aperture was regulated to be ~500 nJ/pulse by adjusting the ND filter, based on the readout power value provided by the optical power meter (PM20A, Thorlabs) shown in Figure 2.5(j). Since we knew that the energy delivery efficiency from the output of aperture 2 to the output of the GRIN lens unit was about 35%, and 30% to the optical power meter, we could estimate the output power at the GRIN lens unit. Under the assumption of a Gaussian beam, this energy yields a surface fluence of ~44 mJ/cm^2, which is about two times greater than the ANSI safety limit (20 mJ/cm^2) for allowable skin laser fluence [25] but below the damage threshold (200 mJ/cm^2).

For this endomicroscope, we utilized the same type of micromotor (SBL015-06XXPG254; Namiki Precision) as employed in our previous endoscopic probes [8] because of its superior torque and scanning speed. Also, as before, we used the scanning mirror's angular position-encoded TTL signals (254 pulses at ~1 kHz per one full mirror rotation) to synchronously trigger peripheral systems, such as the laser and the DAQ card [Figure 2.5(j)]. However, because the optical beam diameter determines the transverse resolution of OR-PAEM, it is important to provide a sufficient A-line sampling density for each B-scan such that consecutive optical beams overlap. Therefore, we implemented another circuit that multiplies the original TTL frequency by eight times [Figure 2.5(l)], i.e., 2032 pulses at ~8 kHz for one full mirror rotation. In other words, we performed OR-PAEM imaging with an A-line acquisition rate of ~8 kHz and a B-scan

20

rate of 4 Hz, which is also the rotational speed of the scanning mirror; each B-scan consists of 2032 A-lines.

As discussed earlier, another advantage of the scanning mirror and built-in micromotor-based mechanical scanning mechanism is that it enables static mounting of the optical fiber and signal wires. Thus, it is possible to perform a pullback C-scan over a large interval without the aid of a sophisticated pullback system. In this study, we utilized a previously-constructed motorized pullback system which includes a step motor and a linear motion guide actuator (KR2001A+200L0-0000, THK) with a stroke of ~14 cm [Figure 2.5(k)]. To synchronously control the pullback pitch in accordance with the rotation of the scanning mirror, we utilized the TTL signals provided by the delay generator, in which a counter circuit was also installed to adjust the pullback pitch, as shown in Figure 2.5(j).
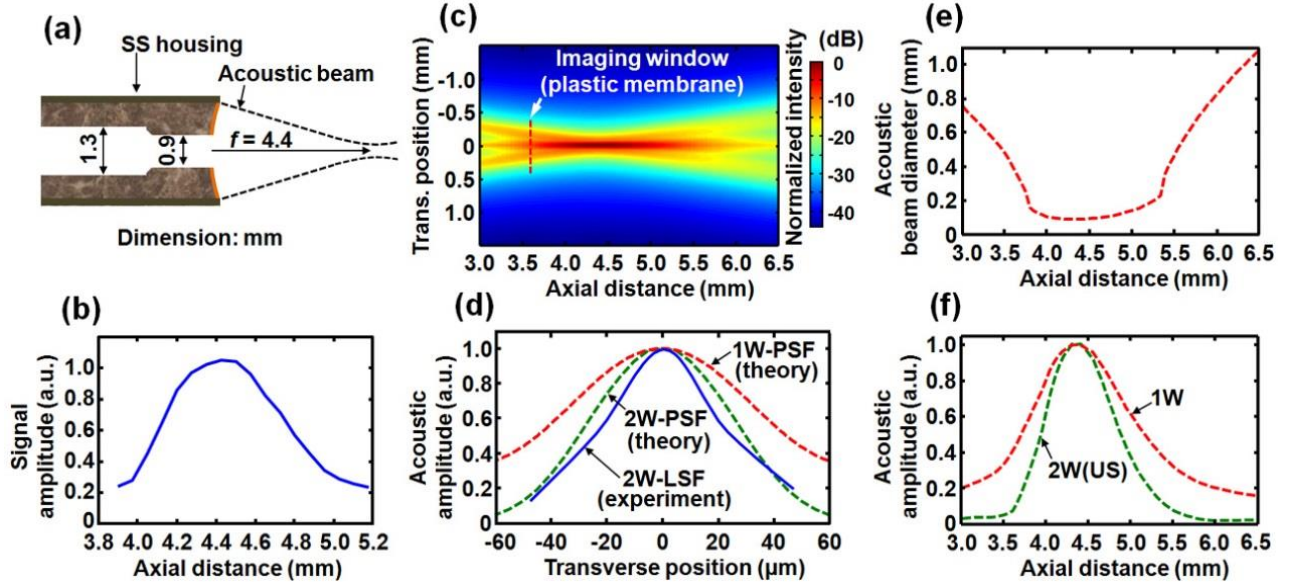
Figure 2.6. Acoustic characteristics of the US transducer. **(a)** Geometry of the transducer (side view). **(b)** Experimentally measured US pulse-echo signal variation. **(c)** Simulated transmission (1W) acoustic intensity map. **(d)** Theoretical transverse 1W- and 2W-PSFs on the focal place, along with an experimentally measured 2W-LSF. **(e)** 1W FWHM-based acoustic beam diameter vs. axial distance. **(f)** 1W and 2W acoustic amplitude variations vs. axial distance.

21

Results In realizing the endomicroscope, to achieve maximum sensitivity, the most critical step was aligning the GRIN lens unit [Figure 2.5(g)] inside the hole of the focused US transducer [Figure 2.5(h)] as accurately as possible. For this reason, we quantified the acoustic performance of the transducer [Figure 2.6(a)] before assembling it with the GRIN lens unit [Figure 2.5(g)]. First, we experimentally determined the focal distance of the transducer by measuring the pulse-echo signals reflected from a quartz block. As shown in the signal amplitude variation graph [Figure 2.6(b)], we observed a peak response at a distance of ~4.4 mm from the transducer. Also, based on the pulse-echo signal, we determined the center frequency (42 MHz) and the fractional bandwidth (~80%) of the transducer. After this experiment, we performed two Field II software [36] simulations to further characterize its acoustic performance.

First, we investigated the transmission acoustic intensity distribution of the transducer and acquired the intensity map presented in Figure 2.6(c). Because this intensity map implies the one-way (1W) sensitivity distribution related with PA signal detection, we extracted from the map a transverse point spread function (PSF) for the focal distance of 4.4 mm [Figure 2.6(d)], which showed a FWHM value of ~86 μm. In general, a 1W-PSF shows a broader distribution than a corresponding US pulse-echo (i.e., two-way: 2W) PSF because only one-way acoustic focusing is involved; the green dotted 2W-PSF curve, which was acquired from another Field II simulation, shows this characteristic. To validate that the theoretical 1W- and 2W-PSFs were reliable data reflecting the true acoustic characteristics of the transducer, we measured a US pulse-echo (2W) LSF, using a ~20 μm diameter tungsten wire. As shown by the blue solid curve [Figure 2.6(d)], the experimentally acquired 2W-LSF agrees well with the theoretical 2W-PSF. From the intensity map [Figure 2.6(c)], we also plotted the variation of the 1W FWHM acoustic beam diameter [Figure 2.6(e)] and acoustic amplitude [Figure 2.6(f)] versus the axial distance;

22

the US pulse-echo (2W) based amplitude variation graph in Figure 2.6(f) was acquired from another Field II simulation.
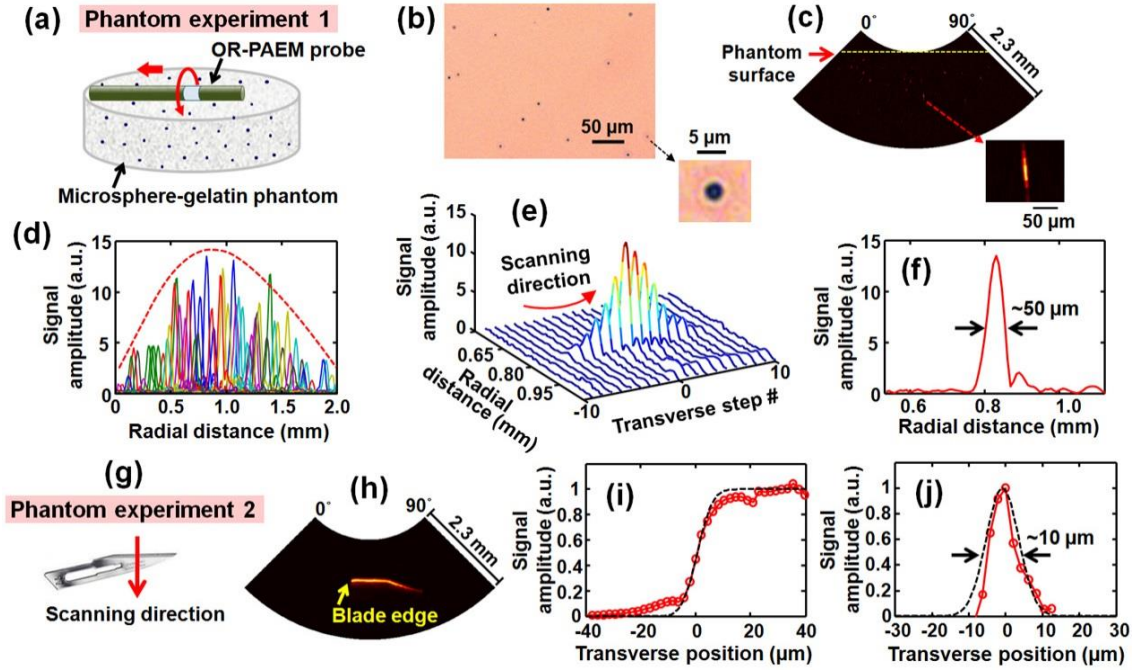
Figure 2.7. Quantification of the system resolutions and sensitivity. **(a)** Schematic rendering of the microsphere-gelatin phantom imaging experiment. **(b)** Light microscopic image of the microsphere-gelatin mixture. **(c)** Representative B-scan image (Hilbert transformed) acquired from the microsphere-gelatin phantom. **(d)** Merged plot of representative A-line signals (Hilbert transformed) generated by microspheres at different depths, which shows a PA signal distribution according to depth (due to the large data size, we plotted only the most prominent microsphere's A-line signal at each depth). **(e)** Plot of sequential A-line signals generated from a microsphere located at the focus. **(f)** Radial and transverse PSFs extracted from (e). **(g)** Photo showing the blade target and scanning direction. **(h)** Averaged B-scan image of the blade (Hilbert transformed). **(i)** ESF extracted from (h). **(j)** LSF derived from (i). In (i) and (j), the dashed curves were fitted with an error function and a Gaussian function, respectively.

We used the analyzed acoustic characteristics of the transducer to guide its assembly with the GRIN lens unit [Figure 2.5(g)]. Because the accurate alignment of the optical and acoustic foci was most critical, we utilized a 100-µm diameter pinhole as an alignment target. In brief, in a water tank, we adjusted the location and orientation of the pinhole to make the transducer's

23

acoustic beam pass through the pinhole; the pinhole could be translated by an X-Y-Z translation stage, while the transducer was firmly fixed. Then we removed the water, inserted the GRIN lens unit into the 1.3-mm diameter hole of the transducer [Figure 2.5(f)], and carefully aligned it so that the transmitted laser beam also passed through the pinhole. We performed the final alignment solely by manually positioning the GRIN lens unit while 5-minutes epoxy spread around the base of the GRIN lens and transducer unit [Figure 2.5(f)] started to cure. A post-assembly measurement showed that the mismatch between the acoustic focus and optical focus was less than 32 µm in the transverse plane. As shown in Figure 2.6(e), the transducer showed a nearly constant maximal focal zone (i.e., a plateau) over a large range, from 3.8 mm to 5.3 mm; just outside these two positions, the acoustic intensity of the side lobes started to become greater than the half values of their maxima (i.e., −6 dB), widening the FWHM beam diameter steeply. The large depth of acoustic focus facilitated the longitudinal alignment of the laser beam and acoustic beam.

First, we imaged an optical phantom made of 3 µm diameter polystyrene black dyed microspheres (#605633, Polysciences) and gelatin (#G2500, Sigma–Aldrich) [Figure 2.7(a)]. In the phantom, the concentrations of the microspheres and gelatin were 0.009% and 10% (w/v), respectively, when they were dissolved in water. Figure 2.7(b) is a light microscopic image (×100) of a drop of the mixture before it hardened. After spreading ultrasound gel on the surface of the phantom for acoustic matching [Figure 2.7(a)], we positioned the endomicroscope, performed a pullback C-scan with a pitch of 1 µm, and recorded 2000 B-scan images during the helical motion of the scanning mirror. For this experiment, however, we did not use the TTL signals provided by the frequency multiplier [Figure 2.7(j)] because the desired transverse step size of the scanning mirror was smaller than the theoretical transverse resolution value of ~9.2

μm. Thus, we utilized a 16-kHz TTL signal provided by a function generator for triggering the DAQ and laser system and also reduced the B-scan speed to 2 Hz, which resulted in an angular step size for the scanning mirror ¼ of the theoretical transverse resolution value.
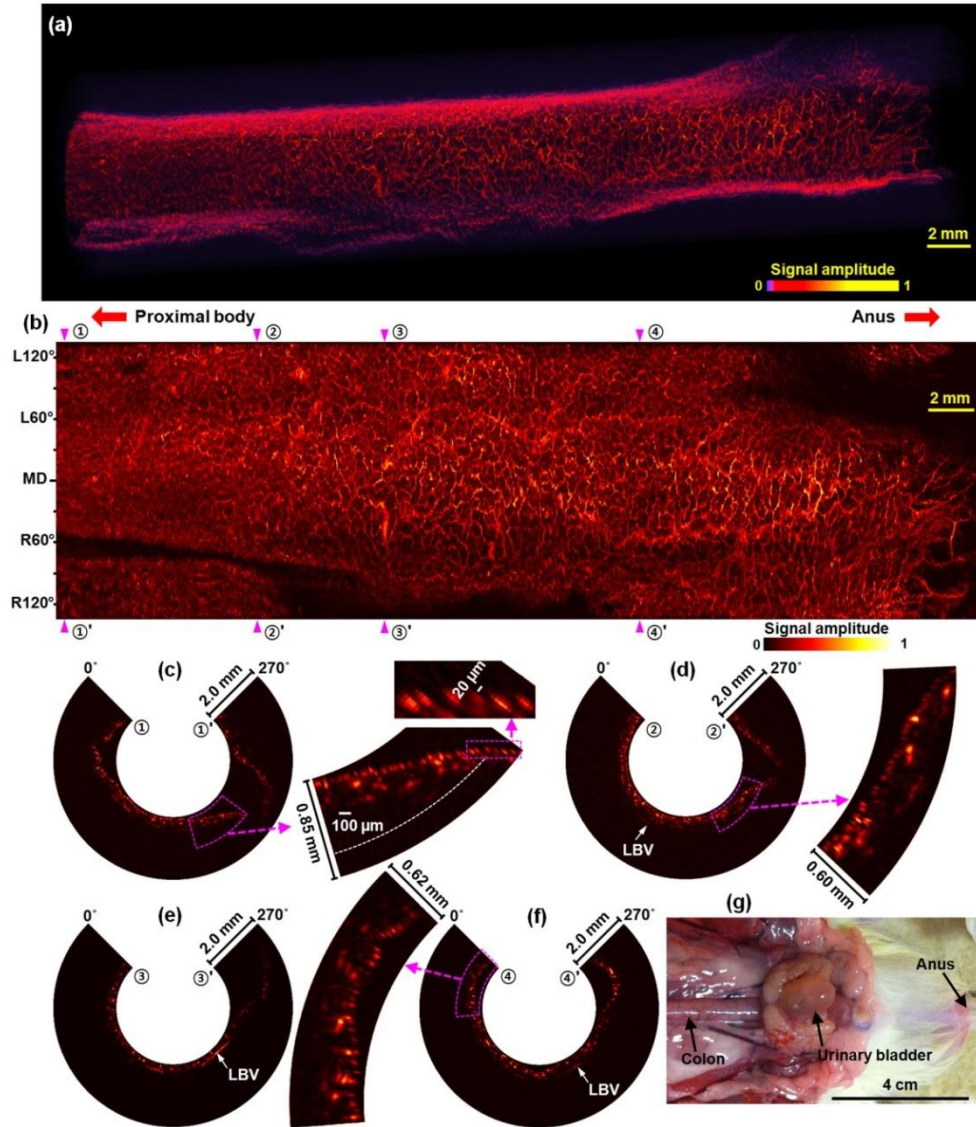
Figure 2.8. Label-free *in vivo* OR-PAEM images of a rat colorectum. **(a)** Volume rendered image (Media 1). The right-hand side corresponds to the anus. **(b)** RMAP image of (a). MD, mid-dorsal; L, left; R, right. **(c–f)** Representative B-scan images (selected from the marked four positions, only ~2.0 mm depths are displayed). In the magnified image of (c), the dashed white arc represents the optical working distance of the probe. LBV, large blood vessel. **(g)** Post-experiment surgical photo.

25

In Figure 2.7(c), we present a B-scan image acquired from the phantom (only a 90° angular region is displayed). As the microspheres were embedded randomly in the phantom, they generated sharp spike signals with different intensities according to depth. So, by plotting all A-line signals that included such spike signals over the entire data set [Figure 2.7(d)], we were able to validate the targeted location of the optical focus and also estimate the sensitivity of the endomicroscope. From the graph, one can see that the signal sensitivities show a clear depth dependency following the diameter variation of the laser beam, and that the strongest signal appeared at the focal distance of the optical illumination (i.e., ~0.8 mm from the probe surface, as we intended), as shown by the manually marked dashed curve. To estimate the radial resolution and signal-to-noise ratio (SNR), we selected a set of PA signals generated by a microsphere located at the focal distance from Figure 2.7(d) and plotted them in Figure 2.7(e). As shown in Figure 2.7(f), from this specific microsphere, the radial resolution was estimated to be ~50 μm, and the SNR appeared to be approximately 29 dB; PA signals from other microspheres also yielded the same radial resolution value.

While the transverse resolution of the endomicroscope also could be estimated from Figure 2.7(e), it might not be accurate because only a few microspheres were located close to the optical focal spot. Thus, to more accurately determine the transverse resolution through an averaging of multiple images, we imaged a surgical blade [Figure 2.7(g)] using the same scanning parameters applied in the previous experiment. After fixing the blade at the focal distance of the endomicroscope [Figure 2.7(g)], we transversely scanned it in the direction of the arrow and acquired 100 B-scan images, from which an ESF could be extracted. Figure 2.7(h) represents an averaged PA image acquired from the blade, and Figure 2.7(i) shows the ESF extracted from the image. To determine the transverse resolution, we took the derivative of the ESF and acquired a

26

LSF [Figure 2.7(i)]. As shown in the fitting curve, the transverse resolution appeared to be ~10 μm, which is close to the beam diameter shown in Figure 2.5(i).

To demonstrate the endomicroscope's IVM capability, we imaged the descending colon of a Sprague Dawley rat (~450 g; Harlan) with the setup shown in Figure 2.5(j). We anesthetized the animal by administrating a cocktail of 87 mg/kg ketamine and 13 mg/kg xylazine (IP) and placed it on a stable stage. Once the animal was properly positioned, we spread medical ultrasound gel into the colon for acoustic matching. Then, we inserted the endomicroscope through the anus, advanced it ~6 cm, and performed a C-scan imaging with a pullback speed of ~40 μm/s and a B-scan speed of 4 Hz. During imaging, anesthesia was maintained with 1.5–2.0% isoflurane supplied through a nose cone. After the experiment, the rat was euthanized by a pentobarbital overdose (150 mg/kg, IP), and subsequently dissected to validate the imaged organ. All procedures in the experiment followed protocols approved by the Institutional Animal Care and Use Committee at Washington University in St. Louis.

In Figure 2.8, we present a volume rendered image [Figure 2.8(a)] and a radial-maximum amplitude projection (RMAP) image [Figure 2.8(b)] acquired from the animal and also display representative B-scan images [Figures 2.8(c)–(f)] and a post-experiment surgical photo [Figure 2.8(g)]. The first two vasculature images were processed from a C-scan data set, 350 pixels deep × 2032 A-lines × 4000 B-scan slices. The images cover a 4 cm long pullback section and 270º angular field of view (in each B-scan image, however, 508 A-lines corresponding to a 90º angular region were removed because they were blocked by the bridge of the SS probe housing). In processing the vasculature images, we applied the Hilbert transformation to the raw data to extract the envelope of the bipolar signal and applied a down sampling algorithm to reduce the data size.
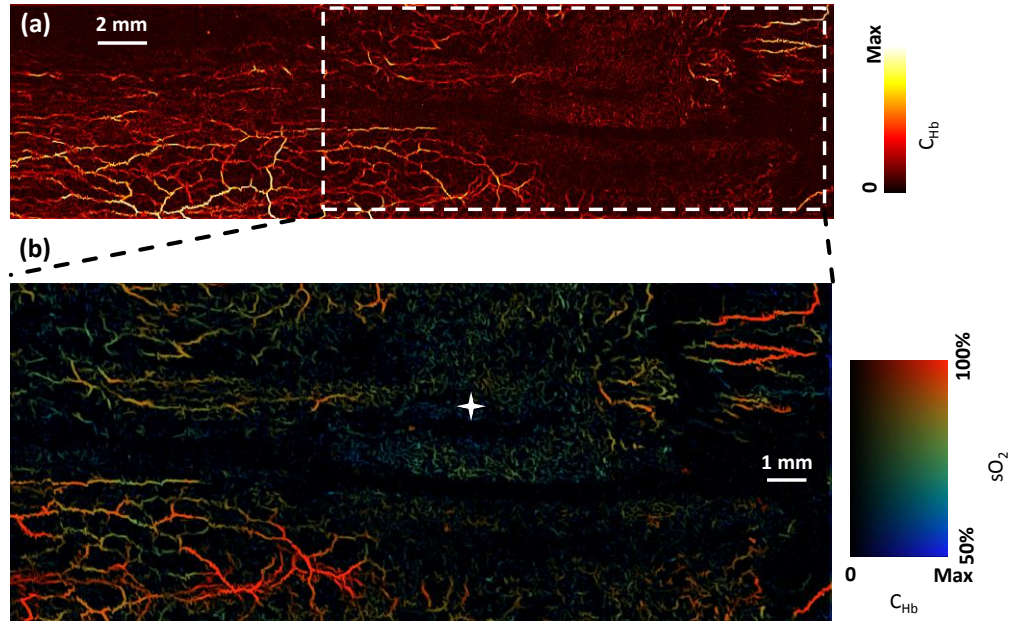
Figure 2.9. (a) Distribution of total hemoglobin contribution of rat colorectum with tumor. **(b)** Oxygen saturation of the tumor region.

As shown in the RMAP image [Figure 2.8(b)], the endomicroscope provided a much clearer view of the colorectal vasculature than the previous acoustic-resolution PA endoscopic images [37]; based on the estimation of apparent blood vessel diameters, approximately a 10-fold improvement in spatial resolution was achieved. Also, the capillaries distributed in the inner wall of the colorectum were clearly differentiated [Figure 2.8(c)] with the full resolving power presented in Figure 2.7. Due to motion artifacts and the large variation in colorectal wall distances [Figure 2.8(c)], however, the apparent resolution in the RMAP image was slightly degraded during the composition of individual B-scan slices. Nevertheless, the prototype probe imaged the colorectal vasculature with an apparent resolution of less than 30 µm.

With the current sensitivity of the transducer and a laser power of 500 nJ, we were able to detect PA signals from a ~500 µm depth, which was enough to encompass the entire thickness of the colorectal wall (~400 µm) and visualize some of neighboring large blood vessels (LBVs)

28

[Figures 2.8(d)–(f)] which are assumed to be the blood vessels connecting the colorectum and mesenteric tissue. The 500-nJ pulse energy was somewhat higher than the values typically utilized in OR-PAM systems. However, the laser beam diameter at the focal distance was also correspondingly larger; the low optical NA of 0.022 was also advantageous in maintaining the optical resolving power over a large depth range.
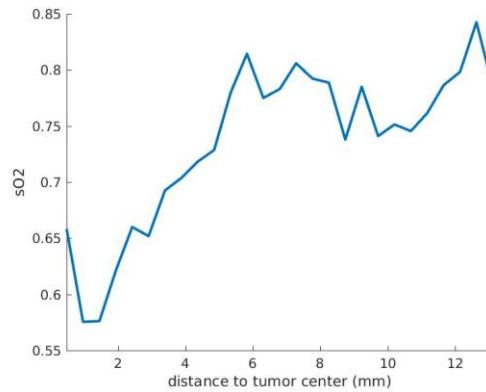
Figure 2.10. Average sO$_2$ at different distance from tumor center (marked with white star in Figure 2.9(b)).

With the improved resolution, we can use the PAEM to study pathological changes with a lot of details. We imaged a rat colorectum tumor with laser beams of two wavelengths and analyzed the oxygen saturation. The image shows convoluted, tortuous, and excessive vessel branching at the tumor region [Figure 2.9(a)]. The tumor also shows lower overall oxygen saturation compared to normal tissue, i.e. the tumor is hypoxemia [Figures 2.9(b), 2.10].

Discussion   In this study, we showed the feasibility of PAT-based IVM for the first time by implementing a fully-encapsulated OR-PAEM probe and imaging the microvasculature of a rat colorectum. With an optical NA of 0.022, we achieved a transverse resolution as fine as 10 μm, the finest among reported optical-resolution endoscopic PA images [31,32], and an SNR of 29

dB from a 3-µm diameter microsphere illuminated by a 500-nJ pulse energy in a beam 9.2 µm in diameter. As demonstrated in the in vivo experiment, the major benefit of OR-PAEM over existing IVM techniques is that it enables high-resolution angiographic imaging without using a contrast agent. Although other groups have achieved comparable resolutions [31,32], their image demonstrations were limited to only phantom experiments because their probes are not fully encapsulated. We achieved the first in vivo OR-PAEM imaging by combining the confocal focused-optical illumination and acoustic detection scheme with our established probe encapsulation and acoustic matching strategy, which is one of the most important technical elements.

Although the acoustic matching and probe sheathing method presented here is not simple and requires a long preparation time (40–60 minutes), we believe it could be a valuable technical basis for developing more advanced PA endoscopic systems. For example, the water injection strategy and associated system elements could be applied to using such an OR-PAEM probe with a medical balloon, which is frequently utilized for mitigating motion artifacts [38] in various clinical environments. One possible option for slightly reducing the long assembly time is to build the GRIN lens and transducer unit [Figure 2.5(d)] without the gap within them [Figure 2.5(f)], by which one can skip the long (~15 minutes) water injection time. However, as we discussed in our recent report [7], the entire acoustic matching and probe sheathing process could be completely avoided if the corrosive water-based matching medium could be replaced with an oil-based medium which could be retained in the probe perpetually. So far, we have tried a silicone oil-based medium. However, we found that, although silicone oil was superior in terms of optical transparency, it turned out to be inapplicable to the current probe configuration because the large travel distance (3.6 mm) from the membrane to the transducer caused large

acoustic attenuation of high-frequency acoustic waves. Thus, high optical transparency and low acoustic attenuation must be considered as key requirements for PA endoscopy.

To make the developed technique more broadly applicable, several additional technical advances should be achieved. The first is to embody a multi-wavelength OR-PAEM system. In this study, we demonstrated the vasculature imaging capability of the implemented endomicroscope by using a 532 nm laser wavelength. We chose the wavelength due to the availability of laser sources with a high pulse-repetition rate (~8 kHz). For *in vivo* vasculature imaging, however, other wavelengths, such as 542 nm and 576 nm, are known to be generally better in terms of the SNR of detected PA signals at a given pulse energy because oxy-hemoglobin shows high optical absorption at those wavelengths. Also, one can choose other wavelengths for visualizing various functional information, such as the oxygen saturation of hemoglobin, or molecular information, such as the distribution of various contrast agents or molecular probes. In general, PAT systems are developed for imaging objects over large depths. Thus, one can choose an optimal wavelength to increase the imaging depth. However, OR-PAM or OR-PAEM is not noted for their depth capability: their typical imaging depth is ~1 mm, and they are more affected by optical scattering. Thus, one can choose the wavelength according to the optical absorption peak of the contrast agent of interest, either endogenous or exogenous.

The second important task is to increase the sensitivity of the imaging probe. In this study, we achieved an adequate SNR with an optical energy of ~500 nJ/pulse, which yields a surface fluence of ~44 mJ/cm^2, about two times greater than the ANSI safety limit (20 mJ/cm^2) for allowable skin laser fluence [25]. Although this value is lower than the damage threshold of general tissue (200 mJ/cm^2), it would not be desirable to use for internal organ imaging, especially for clinical applications (currently there is no explicit and specific reference on the

pulsed laser beam dose to use with PAT. However, we observed no damage with the typical fluence applied to human skin). We believe that the laser dose can be substantially reduced by employing more sensitive ultrasound detectors, such as lead magnesium niobate-lead titanate (PMN-PT)-based US transducer [39] or optical ultrasound detectors [40].

To use OR-PAEM as an even higher resolution IVM imaging tool, the third task is to increase the spatial resolution. Although we showed the feasibility of OR-PAEM imaging, the resolution benefit was limited to only the transverse direction, and the radial (depth) resolution was still limited by the acoustic parameters of the employed US transducer. Thus, in the *in vivo* rat colorectum imaging [Figure 2.8], we were not able to clearly differentiate blood vessels in different layers of the colorectum. Consequently, increasing the radial resolution could be an interesting research subject. It is a well-known fact that achieving high-radial resolution with PAT is relatively difficult compared to other optical microscopy techniques, such as two-photon microscopy. However, a recent study reported by Wang et al. demonstrated that it could be feasible in OR-PAM [41]. In an *in vitro* condition, they achieved a 2.3 μm radial resolution. Also, one can increase the transverse resolution by increasing the optical NA, at the expense of the depth of focus, and optimize the working distance depending on target applications. To acquire high resolution PA images, however, the imaging speed should be increased together with resolution, because motion artifacts deteriorate the apparent resolution.

In this study, we implemented the first OR-PAEM system with a full IVM imaging capability and achieved a transverse resolution as low as 10 μm, the finest among reported optical-resolution endoscopic PA images, and an SNR of 29 dB for a 3-μm diameter microsphere illuminated by a 500-nJ pulse energy in a beam of 9.2 μm in diameter. Also, by using a 532-nm laser wavelength, we acquired the first *in vivo* OR-PAEM image from a rat colorectum and

produced a three-dimensional vasculature image with an apparent resolution of less than 30 µm. As the system can be utilized in small animals and also can potentially accommodate many other multi-functional molecular probes, it could be a useful tool in many biological experiments, such as tumor and metabolic disease studies. Moreover, the OR-PAEM's unique label-free imaging capability would enhance IVM's role in such clinical circumstances where the uses of contrast agents are undesired.

2.3 Catheter-based Photoacoustic Endoscope for Human Esophagus Imaging

Background In 2009, our group implemented a 4.2 mm diameter PA endoscope and demonstrated its feasibility for PAE [6]. To solve the aforementioned technical issues, we employed a rotating scanning mirror driven by a built-in micromotor. The main advantage of this probe configuration is that it enables static mounting of the optical fiber and signal wires, thereby facilitating the optical and acoustical integration and providing a simple solution to the acoustic matching requirement. As the performance of the prototype endoscope was satisfactory, we developed a 3.8 mm diameter probe [7] with the same probe configuration. In addition to reducing the size of the probe, we also improved the image resolution by using a focused US transducer. With this probe, we demonstrated simultaneous dual-wavelength PA and US endoscopy for the first time through *in vivo* animal experiments. After the *in vivo* demonstration, we proceeded to develop a 2.5 mm diameter miniprobe to increase the clinical applicability of the PAE technique [8]. Our goal was to use the miniprobe for imaging human upper gastrointestinal (GI) tracts with Barrett's esophagus via the 3.7 mm diameter instrument channel of a clinical video endoscope. However, the sharply bent section of the entry port precluded

normal insertion of the 35 mm long rigid distal section, which includes a micromotor. To avoid this bend, the probe had to be inserted in reverse through the exit port. Thus, we concluded that the probe was suitable only for lower GI tract imaging.

For imaging the human esophagus, it is essential to use a video endoscope for image guidance to approach the target organ safely. Thus, the PAE probe must be narrow and flexible to pass through the instrument channel of the video endoscope freely. The probe also must be fully encapsulated to avoid direct contact of the scanning tip with the target tissue during mechanical scanning. To meet these technical requirements, we have designed and implemented a new catheter-based PAE system and demonstrated its endoscopic functionality through the instrument channel. This endoscopic system is based on mechanical scanning of a single-element US transducer. Its flexible catheter section, 3.2 mm in outer diameter and 2.5 m in length, can be inserted into a 3.7-mm diameter instrument channel. This prototype features a flexible shaft-based proximal actuation mechanism, like commercial endoscopic ultrasound miniprobes, and a laser beam delivery through a rotary junction, like most endoscopic optical coherence tomography catheters. To the best of our knowledge, this is the first PAE system that has been fully encapsulated in a plastic catheter and sufficiently miniaturized to be usable for imaging via the instrument channel of a standard clinical endoscope. Here, we describe the detailed structure and fabrication of the new PAE system and present experimental results demonstrating its full intra-instrument channel workability and in vivo imaging capability.

Methods   Figure 2.11 shows schematic diagrams and photos of the implemented PAE system. As presented in Figure 2.11(a), the endoscopic system is comprised of a proximal actuation unit, a ~2.5 m long flexible body section sheathed with a plastic catheter, and a rigid distal section that includes a scanning mirror. A step motor installed in the proximal actuation

unit provides torque. The torque is transferred to a hollow metal shaft supported by two ball bearings through a timing belt and pulleys, and further transmitted to the scanning mirror through the 2.5-m long flexible shaft (TC+2113-70-2600-01, Asahi Intecc). Finally, the scanning mirror receives the torque and performs side-view rotational scanning.
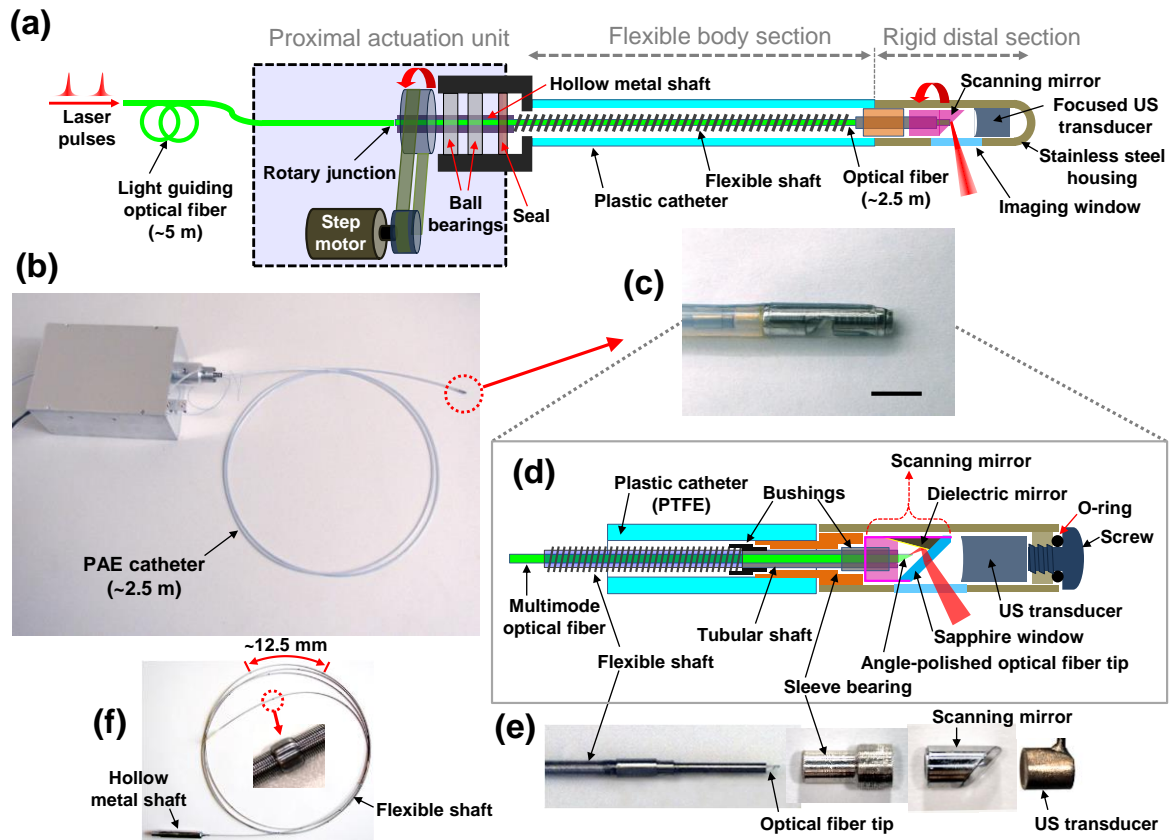
Figure 2.11. **(a)** Schematic of the catheter-based PAE system. **(b)** Photo of the entire endoscopic system. **(c)** Photo of the rigid distal section. **(d)** Schematic showing the detailed structure of the rigid distal section presented in (c). **(e)** Photos of the flexible shaft and optical fiber tip, the bronze sleeve bearing, the scanning mirror, and the focused US transducer. **(f)** Photo of the 2.5-m long flexible shaft connected to the hollow metal shaft depicted in (a). The inset represents a magnified sleeve bearing.

For PA imaging, a pulsed laser beam from a laser source (Nd:YVO4, INNOSLAB IS811-E, EdgeWave) is guided by a multimode optical fiber (~5 m long, 0.22 NA, 365 μm core diameter, BFL22-365, Thorlabs), transferred via a rotary junction [Figure 2.11(a)] to the endoscope's

optical fiber (same type, ~2.5 m long) located inside the flexible shaft, sent to the target tissue by the optics located in the scanning mirror to generate PA waves. The generated PA waves that propagate to the scanning mirror are reflected to a focused US transducer (1.7 mm aperture, f = 5 mm, NA = 0.17, 40 MHz) and converted into electrical signals. Figures 2.11(b) and (c) show the entire endoscopic system and the distal section of the probe.

In Figures 2.11(d) and (e), we present a more detailed structure of the rigid distal section [Figure 2.11(c)] and photos of several key components, respectively. The rigid distal section is ~16 mm long, and its housing was fabricated from a 3.05 mm diameter stainless steel tube (wall thickness: 0.33 mm). Inside the housing, the scanning mirror (2.1 mm outer diameter) and the focused US transducer (2.1 mm outer diameter) are encapsulated as shown in Figure 2.11(d). To provide smooth rotation to the scanning mirror, we utilized a bronze sleeve bearing, and placed bushings at the sleeve bearing's ends to eliminate longitudinal movement of the scanning mirror. The bronze sleeve bearing also acts as a joint connecting the rigid distal section and the plastic catheter (3.18 mm outer diameter, and 1.59 mm inner diameter) made of polytetrafluoroethylene (PTFE, ZEUS). The scanning mirror is mechanically coupled to the flexible shaft via a narrow-diameter stainless steel tubular shaft (~0.81 mm outer diameter).

The optical fiber's tip [Figure 2.11(d)] is polished at an ~30° angle, and the scanning mirror's inner space is filled with air, so that the laser beam that impinges on the polished fiber surface experiences an optical total internal reflection (TIR) and it exits the fiber with an oblique angle of ~43°. The laser beam is then reflected by a dielectric-coated borofloat mirror (altered from #45-596, Edmund) and finally sent to the target tissue after passing through an optically transparent sapphire window (altered from #43-627, Edmund) and an optically clear PET plastic membrane (~3 mm inner diameter, ~25 μm wall thickness, 103-0380, Advanced Polymers). The

PET membrane, a medical grade plastic, forms an imaging window by sealing the inner cavity of the stainless steel housing.

To provide acoustic matching from the imaging window to the US transducer [Figure 2.11(d)], we filled the inner cavity of the endoscope with de-ionized water. Also, we used sapphire for the optical window of the scanning mirror because it has an adequate thickness (0.5 mm) and high acoustic impedance (44.3 MRayl) for perfect TIR of the approaching acoustic waves within the acceptance angle of the US transducer. The 0.5-mm thickness is ~1.8 times larger than the wavelength of the 40 MHz acoustic waves, and the ratio of sound propagation speeds in water and sapphire is 1.5/11.1 for longitudinal waves.

In Figure 2.11(e), we show the components of the rigid distal section, including the flexible shaft and optical fiber tip, the bronze sleeve bearing, the scanning mirror, and the focused US transducer. Figure 2.11(f) shows the entire flexible shaft; its proximal end is connected to the hollow metal shaft [Figure 2.11(a)], and its distal end, which corresponds to the optical fiber tip, is shown in Figure 2.11(e). As shown in the inset, we affixed stainless steel sleeve bearings around the surface of the flexible shaft at ~12.5 cm intervals to minimize mechanical friction during its rotation. To assemble the components, we utilized medical grade epoxies, such as M-31CL (Loctite) and DP-125 (3M).

Figure 2.12 shows the interior of the proximal actuation unit [Figure 2.11(a)]. To control the step motor's rotation speed, we employ a function generator (SFG-2110, GWInstek) which provides TTL signals with a continuously variable frequency. The function generator's TTL signals trigger the step motor's driver circuit as well as the laser system and a data acquisition (DAQ) card (NI PCI-5124, National Instruments). Once an endoscopic imaging session is initiated, we

slowly dial the function generator's TTL frequency to a desired value and then transmit the TTL signals to the laser system and immediately activate our DAQ program. The acquired PA images are displayed on the computer screen in real time. For PA imaging, we utilized a 532-nm laser wavelength (~10 ns pulse duration) with a pulse energy of ~0.25 mJ. The laser beam delivered by the 5-m long guiding optical fiber was coupled to the endoscope's 2.5-m long optical fiber via the rotary junction. The inset shows the rotary junction, in which one can see two glass ferrules that enclose the 2.5 m and 5 m optical fibers. We set the number of A-lines for one full B-scan to be 400, which yields an angular step size of 0.9°.
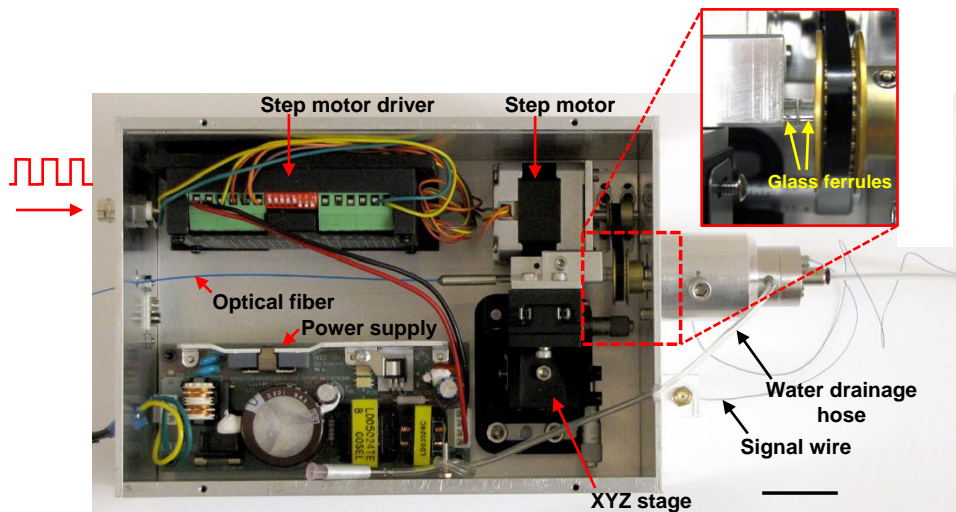
Figure 2.12. Photos of the proximal actuation unit. The inset shows a magnified view of the rotary junction formed for coupling the two multimode optical fibers. The optical fibers are placed inside the two glass ferrules.

To induce PA signals, an adequate level of laser energy must be delivered to the target tissue via the narrow area of the scanning mirror. As a high laser flux and a high pulse repetition rate can result in gradual degradation of the optical components, the optics needs to be carefully designed. In addition, it is important to configure the optical illumination and acoustic detection units of the rigid distal section appropriately to optimize the signal detection sensitivity over a

large depth range. Considering these issues, we designed and implemented the units as shown in Figure 2.13.
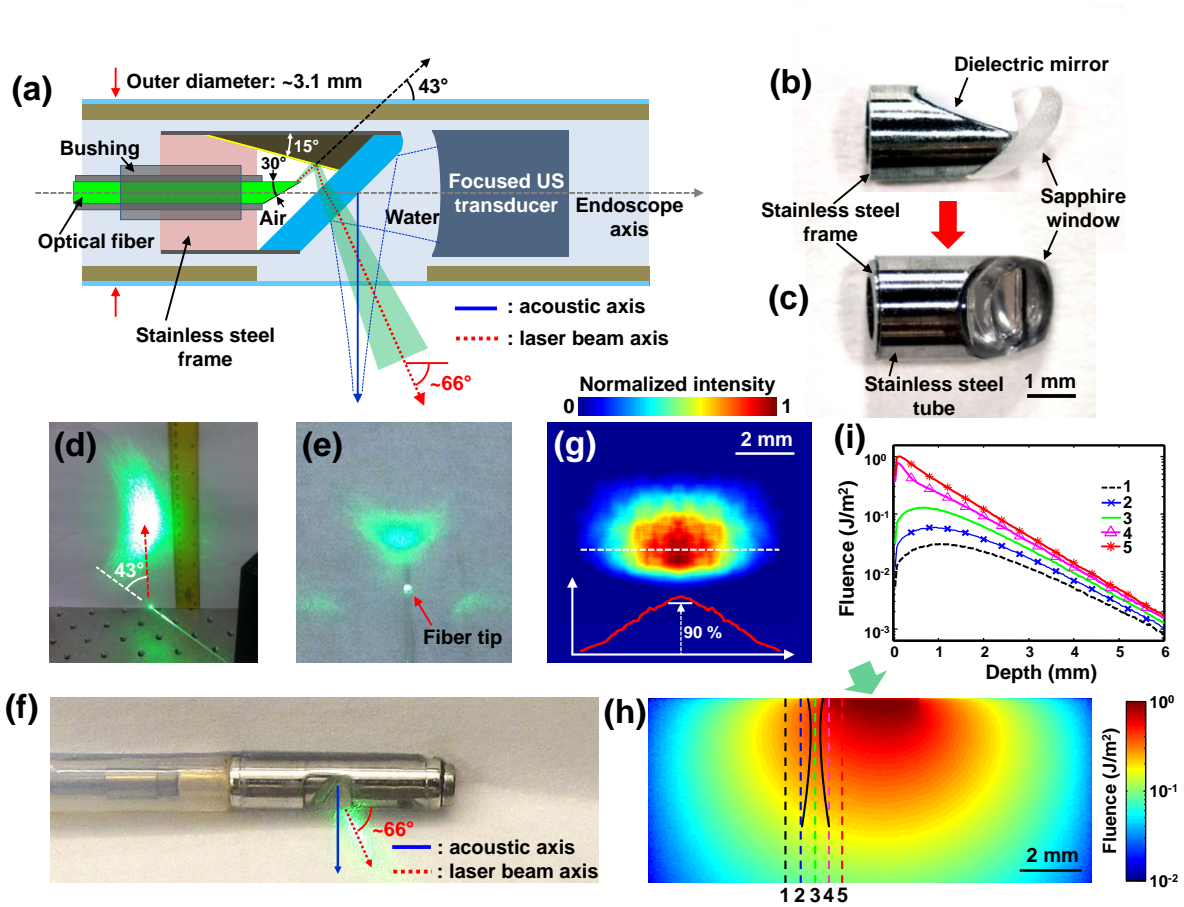
Figure 2.13 (a) Schematic showing the configuration of optical and acoustic components at the distal end. **(b)** Photo of the dielectric mirror and sapphire window attached on a stainless steel frame. **(c)** Photo of the entire scanning mirror encapsulated in a stainless steel tube (rotated by ~90° from (b)). **(d)** Photo of laser beam projected horizontally to a screen with a deflection angle of 43°. **(e)** Top view of the optical fiber tip and beam profile projected to a screen. **(f)** Photo showing the laser beam firing direction and acoustic axis of the endoscope. **(g)** Approximate beam profile of the laser beam exiting the endoscope. To remove the intensity fluctuations caused by speckle, we averaged the original raw data image from the beam profiler. **(h)** Monte Carlo simulated two-dimensional fluence distribution in the plane including the laser beam axis and the acoustic axis. **(i)** Fluence variations along the dotted lines shown in (h). Line #3 indicates the fluence distribution along the acoustic axis.

In determining the beam path, our main goal was to make the laser beam illuminate the target tissue as perpendicular as possible to the axis of the endoscope and to ensure that the laser beam overlapped the acoustic axis of the US transducer, which detects the PA waves reflected by the sapphire window [Figure 2.13(a)]. To achieve this objective, we conceived a laser beam guiding method that uses an angle-polished fiber in combination with a small dielectric mirror, which is attached on the stainless steel frame along with the sapphire window as shown in Figure 2.13(b); Figure 2.13(c) shows the entire scanning mirror encapsulated in a stainless steel tube (outer diameter: 2.1 mm).

As shown in Figure 2.13(a), the laser beam is fired toward the dielectric mirror from the multimode optical fiber (core diameter: 365 µm, n = 1.463 at 532 nm) and then reflected by the dielectric mirror. Because the optical fiber tip was polished at a 30° angle [Figure 2.13(a)], the exiting laser beam is deflected by ~43° (for the chief ray) as shown in Figure 2.13(d); an example of the beam shape exiting the optical fiber is presented in Figure 2.13(e). However, by adding a reflection plane (the dielectric mirror) with a tilt angle of ~15° to the endoscope axis [Figure 2.13(a)], we could increase the laser beam illumination angle to ~66° after it exited the sapphire window (n = 1.768). Figure 2.13(f) shows the final laser beam firing direction and the acoustic axis of the transducer, from which one can see a mismatch, whose effect will be discussed later. The laser beam firing method using an angle-polished optical fiber was first introduced by Karpiouk et al. in their intravascular imaging catheter [42]. However, we added the dielectric mirror to increase the incident angle to the target tissue.

To more accurately analyze the laser beam profile, we utilized a beam profiler (OPHIR Beam Gauge). As presented in Figure 2.13(g), the measured beam profile showed a broad illumination pattern, and the beam area with intensity larger than 90% of the peak value at the central zone

was ~0.64 mm^2 when it passed through the imaging window; ~7.3 % of the total energy was concentrated in this area. Thus, the set 0.25-mJ pulse energy yielded an optical fluence of lower than 3 mJ/cm^2 (i.e., 15% of the ANSI safety limit [25] for allowable skin laser fluence). The image resolution of this endoscopic system is determined by the acoustic parameters of the focused US transducer because no light focusing optics is coupled with the optical fiber. In designing the endoscope, we targeted a working distance of ~2 mm from the endoscope's surface to image human upper GI tracts with Barrett's esophagus in direct contact mode; Barrett's esophagus is a representative esophageal disease developed in the epithelial layer of the lower esophagus and regarded as a precursor of esophageal cancer.

Using the beam profile data [Figure 2.13(g)] and considering the laser beam incident and diverging angles, we performed a Monte Carlo simulation [43] to estimate the optical fluence distribution in target tissue near the acoustic axis. For the simulation, we assumed a semi-infinite medium for the target tissue with a planar and index-matched boundary (relative refractive index n_{rel} = 1) and optical properties of absorption coefficient μ_a = 1.5 cm^{-1}, scattering coefficient μ_s = 200 cm^{-1}, and scattering anisotropy g = 0.908; these optical properties were of human mucosa tissue reported by Bashkatov et al. [44]. As shown in the simulation result [Figure 2.13(h)], the irradiated laser beams [Figure 2.13(g)] quickly diffuse omni-directionally after propagating one transport mean free path (~0.5 mm). The fluence distribution along the acoustic axis is plotted in Figure 2.13(i). Even though there is a mismatch between the laser beam firing direction and the acoustic axis, the endoscope can acquire PA A-line signals over a large depth.

For this endoscope, we implemented a self-focused US transducer (1.7 mm aperture, f = 5 mm) using lithium niobate (LiNbO$_3$) for the piezoelectric material. Figures 2.14(a) and (b) show a schematic and photo of the implemented transducer. The transducer's structure and fabrication

process were similar to those of the transducer previously utilized for the micromotor-based endoscopic probe [8]. However, we achieved the focusing by applying a press-focusing technique [35] that forms the piezo-element's concave shape through a cracking process created by pressure applied to the planar surface of the piezo-element. The pressure was typically applied by a steel bearing ball with the same radius as the desired focal distance (i.e., 5 mm for this case). Compared with the previous lens-based focusing technique, which affixed a plastic acoustic lens to the surface of a flat transducer [8], the press-focusing technique enabled fabrication of a focused US transducer with a higher sensitivity than a lens-based counterpart (i.e., without the acoustic attenuation caused by the plastic lens) and also yielded a higher success rate in the focused transducer fabrication process. We measured the insertion loss of the transducer to be 27.6 dB (water attenuation compensated), which was higher than that of the previous transducer [7] because of the higher electrical impedance mismatch caused by the reduced element area (output impedance: ~300 Ω).
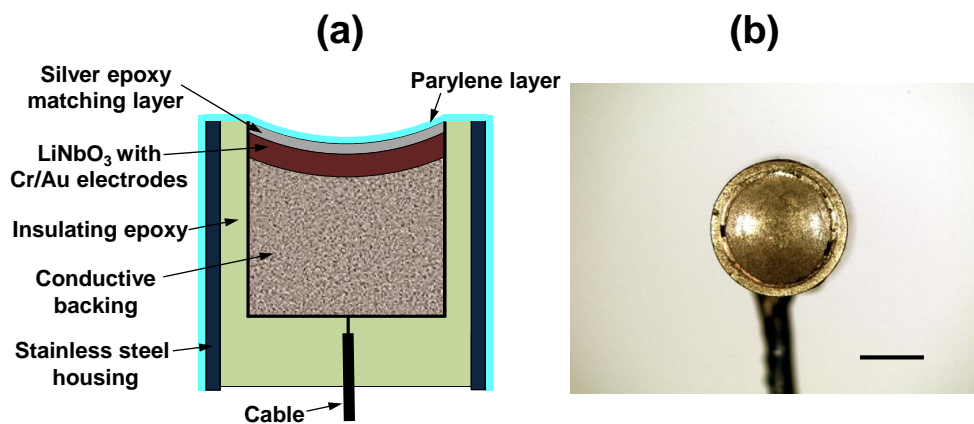

Figure 2.14 Schematic **(a)** and photo **(b)** of the focused US transducer implemented by applying the press-focusing technique.
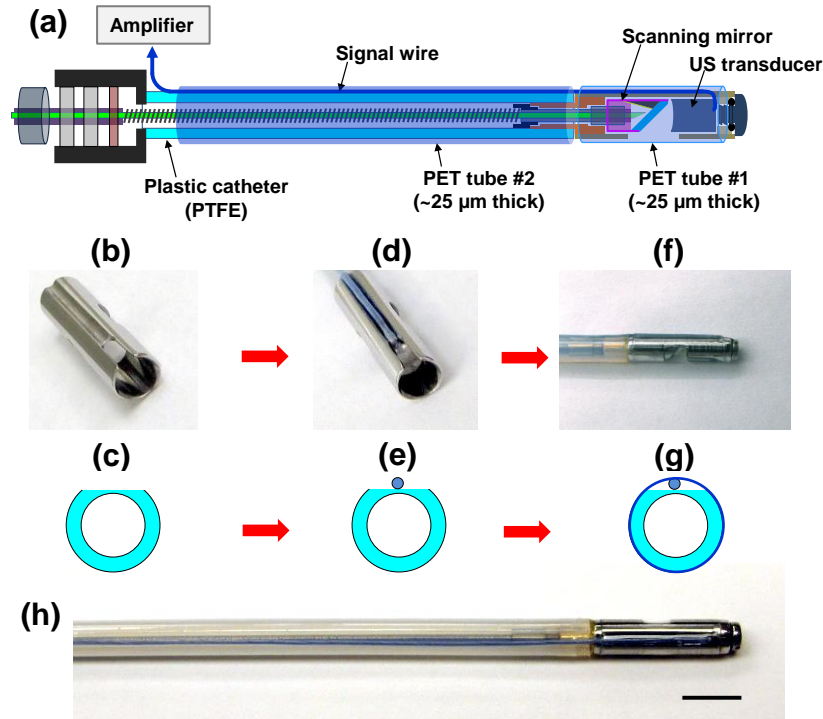
Figure 2.15 (a) Illustration of the affixed US transducer's signal wire. **(b–g)** Procedure for affixing the signal wire at the stainless steel housing (b, d, f) and plastic catheter (c, e, g). **(h)** Photo of the catheter probe after affixing the signal wire.

As the US transducer is spherically focused, its transverse resolution varies with depth from the transducer surface (radial distance); the highest resolution zone of the transducer is located ~2 mm from the imaging window (plastic membrane). In general, a focused US transducer provides excellent transverse resolution in the focal zone, but out of the focal zones, its transverse resolution degrades more quickly than that of an unfocused transducer. Nevertheless, we utilized such a focused type US transducer to resolve blood vessels distributed in the human esophageal wall. We also chose lithium niobate single crystal as the piezo-electric material because it consistently shows high performance for the press-focusing technique.

Unlike in our previous micromotor-based endoscopic probes, the US sensor in this PAE system is placed near the tip of the probe, and the flexible shaft and the scanning mirror are closer to the

proximal part, occupying most of the inner space of the 2.5 m long plastic catheter section. To route the signal wire of the US transducer, we applied a static mounting method, which affixes the signal wire on the outer surface of the PTFE plastic catheter, using two thin PET plastic tubes (~25 µm thickness), as illustrated in Figure 2.15(a). We had applied this static mounting method in our previous endoscopic systems and learned that it minimizes the interference noise that is typically caused by the nearby pulsed laser system. Figures 2.15(b)–5(h) show the detailed procedure for affixing the signal wire.

In this catheter endoscope, we utilized a 0.44 mm diameter coaxial cable (50 Ω, 40232-1-600-S-00000, Hitachi Cable Manchester) for the signal wire of the transducer and a 3.2 mm outer diameter PTFE plastic catheter (wall thickness: 0.80 mm) for the sheath of the flexible shaft. To create a route for the signal wire without exceeding the 3.2 mm probe diameter, we first milled one side of the stainless steel housing as shown in Figure 2.15(b) and also removed ~0.4 mm from one side of the PTFE plastic catheter, as shown in Figure 2.15(c). We then carefully aligned the signal wire along the milled groove [Figure 2.15(d)] and the flat surface [Figure 2.15(e)]. Finally, we secured the wire using two medical-grade PET tubes #1 (103-0380, Advanced Polymers) and #2 (103-0147, Advanced Polymers) over the 16 mm long rigid distal section [Figure 2.15(f)] and the 2.5 m long flexible body section [Figure 2.15(g)]. PET tube #1 is the same as that used to form the imaging window; so it is optically and acoustically transparent and seals the inner space of the probe. Figure 2.15(h) is a photograph of the secured signal wire, and the proximal situation of the wire is shown in Figure 12. Owing to the passage of the signal wire along one side of imaging window, the endoscope's angular field-of-view was limited to ~160°.

Enclosing the signal wire using the PET tubes also provides a simple solution for sterilization of the endoscope. As the PET tubes (#1 and #2) are very strong for their wall thickness (~25 µm),

they safely isolate the inner components from physical contact with the target tissue, and their surface can be easily sterilized with 70% ethanol or ethylene oxide. Also, the thin-wall PET tubes can be easily removed using an ordinary surgical blade and replaced with new ones whenever necessary. Although the replacement work cannot be done quickly in clinical settings, it will definitely benefit hygiene and safety.
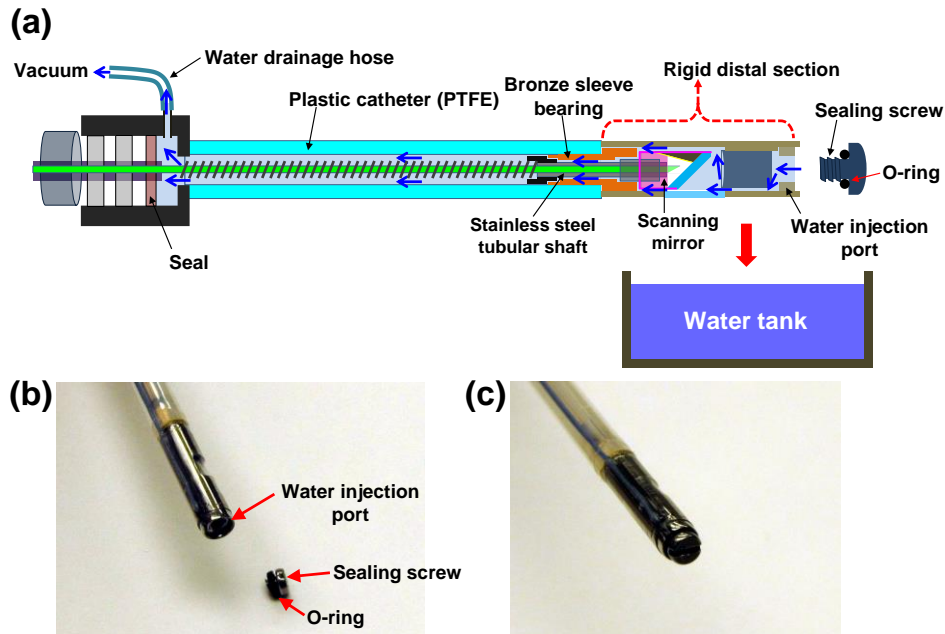
Figure 2.16. (a) Illustration showing a water injection method for providing acoustic matching in the inner cavity of the endoscope. Photos of the inlet with the sealing screw opened **(b)** and closed **(c)**.

As mentioned previously, providing an appropriate acoustic matching medium for the inner cavity of this endoscopic probe is also important to efficiently transmit generated PA waves to the US transducer. In this study, similar to our previous endoscopic systems, we utilized deionized water as the matching medium, which exhibits both high optical transparency and low acoustic attenuation for high-frequency acoustic waves. However, it gradually corrodes the metallic components and degrades the glued points. Thus, to counteract these problems, we added water injection and drainage ports to the endoscopic system. Before each endoscopic

45

experiment, we fill the inner space of the endoscope with deionized water, and drain it after use. Figure 2.16 depicts the water injection procedure and related system components.
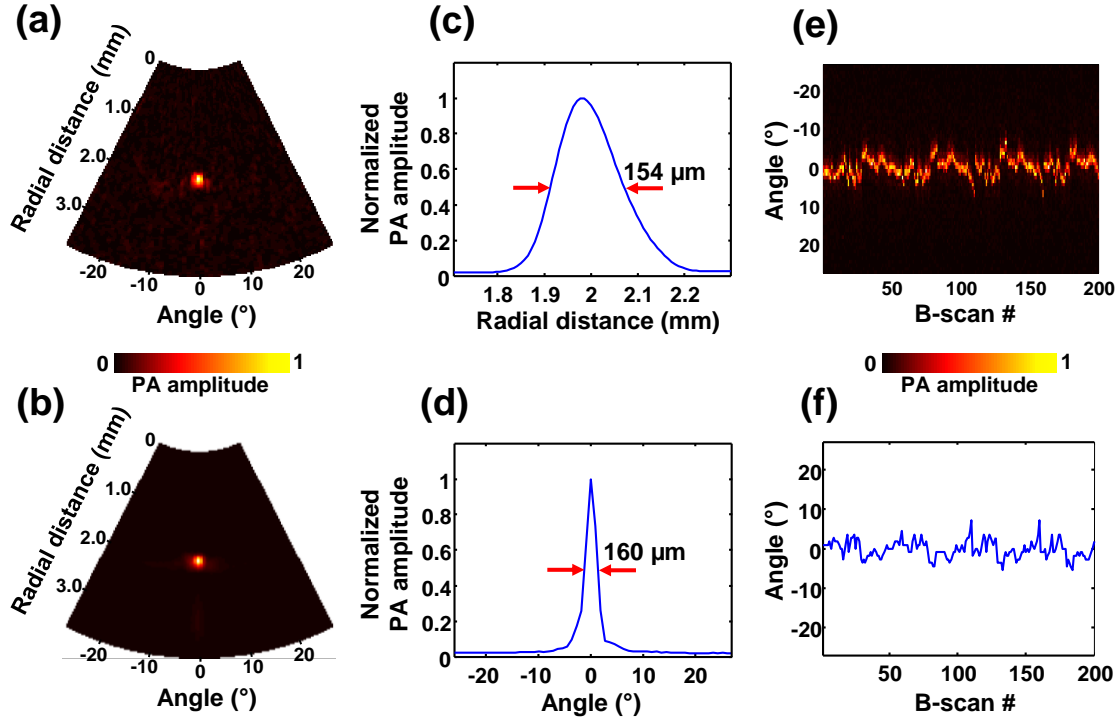
Figure 2.17. (**a**) Experimental setup for quantifying the spatial resolution of the endoscope using a tungsten wire in clear water. (**b**) Typical PAE B-scan image of the 20-µm diameter tungsten wire (only 54° angular FOV is presented). (**c**) Averaged image of the tungsten wire from 200 B-scan images. Radial (**d**) and transverse (**e**) LSFs of the tungsten wire shown in (c). (**f**) Radial-maximum amplitude projection image of the tungsten wire processed from 200 B-scan images. (**g**) Center position graph of the tungsten wire extracted from (f).

For water injection, we open the sealing screw at the distal end of the probe and immerse the water injection port into a tank of deionized water, as shown in Figure 2.16(a). Then, we connect a water drainage hose to a vacuum pump, which sucks up the water. Once the vacuum pump is switched on, the water starts to fill the inner cavity of the distal end by flowing through a narrow channel formed on one side of the US transducer. It then gradually moves to the flexible catheter section via the narrow gap between the stainless steel tubular shaft and the bronze sleeve bearing.

46

It finally exits through the water drainage hose located at the proximal actuation unit [Figure 2.12]. The blue arrows in the diagram show the water flow route. Once the inner cavity is filled with water, the water injection port is blocked using the sealing screw, as presented in Figures 2.16(b)(c). If, on visual inspection under a ~20× microscope, bubbles are seen inside the cavity, the same procedure is repeated until no bubbles appear. Although we inject deionized water, it still has to be drained after the experiment because it gradually becomes ionized, which would corrode the metallic components. For drainage, we open the water injection port and connect the water drainage hose to the same vacuum system. When the water has been drained, we flush the inner cavity several times using 95% ethanol, following the same injection method, then maintain the vacuum connection for several hours to completely remove the ethanol.

Results   After building the system, we tested its mechanical performance and also quantified its image resolution. With the capacity of the employed step motor, the PAE system could reach a maximum B-scan speed of 5 Hz, corresponding to an A-line acquisition rate of 2 kHz; higher scanning speeds were limited by the mechanical friction caused by the long length of the flexible shaft. To analyze the endoscopic probe's spatial resolution and scanning stability, we imaged a ~20 μm diameter tungsten wire in a water tank. We placed the target at the focal position of the endoscope (2 mm from the endoscope surface) and recorded 200 B-scan images. In this phantom experiment, however, we delivered laser pulses to the target using a different light-guiding optical fiber because the experiment was performed in a clear medium which did not scatter the obliquely-fired laser beam to the scanning plane of the transducer. So, as shown in Figure 2.17(a), we connected the light-guiding optical fiber to the coupling optics of the endoscope and performed the B-scan imaging by illuminating the wire target from one side, while keeping all other settings the same. Although we performed this resolution experiment by

47

exciting the target using a different optical fiber, its results are valid because the spatial resolution of this acoustic-resolution PA endoscope is nearly solely determined by the focused US transducer, i.e., not by the optical illumination.

Figure 2.17(b) shows a typical PA B-scan image acquired from the tungsten wire; because PA A-line raw data include negative values, i.e., they are bipolar, we applied the Hilbert transformation to extract the envelope of the signal. To more accurately quantify the resolution, we averaged the 200 B-scan images pixel by pixel. From the averaged image [Figure 2.17(c)], we acquired the radial and transverse LSFs presented in Figures 2.17(d) and (e), respectively. By analyzing the FWHMs of the LSFs, we determined the radial and transverse resolutions to be ~150 μm and ~160 μm, respectively. These experimental resolutions were worse than the theoretically estimated resolution values of 43 μm (radial) and 156 μm (transverse); the large discrepancy in the radial resolution was caused by the electric impedance mismatch between the transducer and the amplifier, which resulted in a narrowed effective bandwidth for the transducer.

Using the 200 B-scan images, we also analyzed the mechanical jitter (or scanning stability) of the scanning mirror. As presented in Figure 2.17(f), which was produced by applying a typical radial maximum amplitude projection process to the 200 B-scan images, the recorded positions of the wire target were not constant and showed a fluctuation in the lateral direction (i.e., in angle), caused by the non-uniform rotation of the scanning mirror. We extracted the center positions of the tungsten wire in angle value [Figure 2.17(g)] and determined the root mean square (rms) lateral fluctuation of the scanning mirror to be ~2.2°.
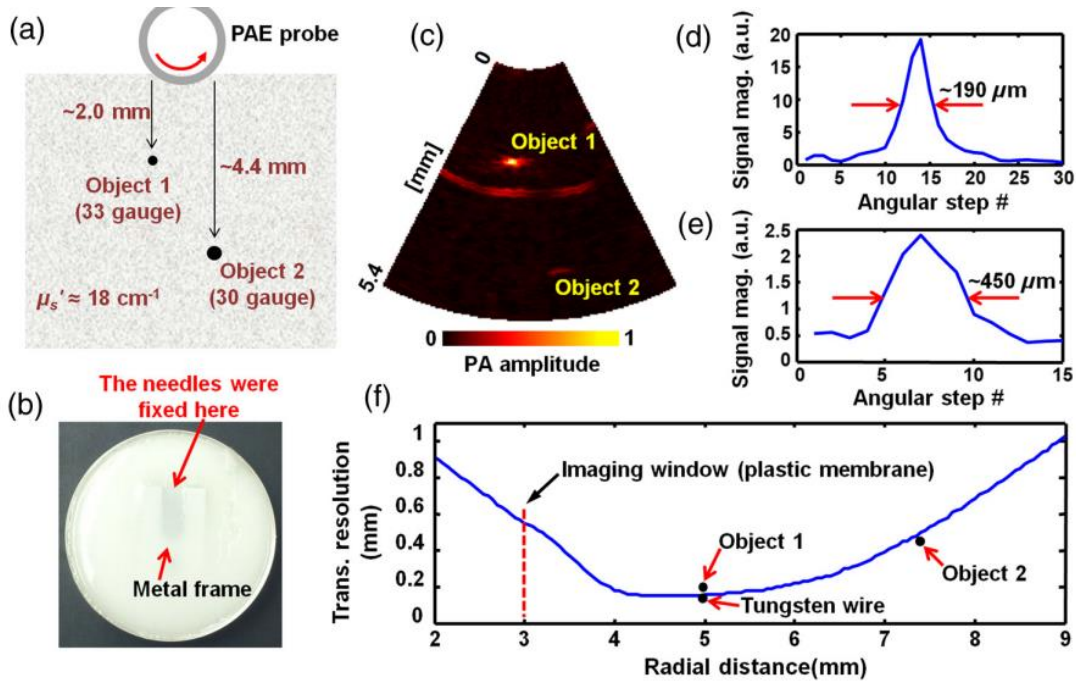
Figure 2.18. **(a)** Structure of the Intralipid-gelatin based tissue mimicking phantom including two metal objects (side view). Objects 1 and 2 are 33 gauge (~210 µm dia.) and 30 gauge (~310 µm dia.) hypodermic needles, respectively. **(b)** Photo of the phantom (top view). **(c)** Typical PAE B-scan image of the two needles (only 54° angular FOV is presented). **(d, e)** Transverse signal variations of the two needles analyzed from (c). **(f)** Transverse resolutions vs. radial distance. The solid line was estimated from the simulation result, and the dots were determined by the experiments.

While the radial resolution of the focused US transducer shows a relatively constant value, its transverse resolution shows a large variation according to depth. To investigate the depth dependence, we imaged two hypodermic needles embedded in an Intralipid-gelatin based tissue mimicking phantom. Figures 2.18(a) and (b) show the structure and photo of the phantom, respectively. In creating the phantom, we utilized a 33 gauge (Object 1, ~210 µm dia.) and a 30 gauge (Object 2, ~310 µm dia.) needle as light absorbing objects and fixed them at ~2.0 mm and 4.5 mm depths from the surface of the phantom using a metal frame [Figure 2.18(b)]. We added 20% Intralipid (Fresenius Kabi, purchased from VWR International, #68100-276) to a gelatin-water solution to mimic the reduced scattering coefficient of typical mucosa tissue (~18 cm^{-1})

[44]. The gelatin was purchased from Sigma-Aldrich (#G2500-1kG; gel strength 300, Type A), and the Intralipid-gelatin-water phantom was made according to the recipe in Reference [45]. In this experiment, we utilized relatively large diameter targets compared with the previous tungsten wire imaging experiment to acquire PA signals with adequate signal-to-noise ratios; as the matrix medium is turbid, the optical fluence near the objects is much weaker than that in the clear medium. Also, the diameters of the two needles were selected according to the theoretical resolution values, although the diameter of Object 1 was ~35% larger than the theoretical resolution value at the position.
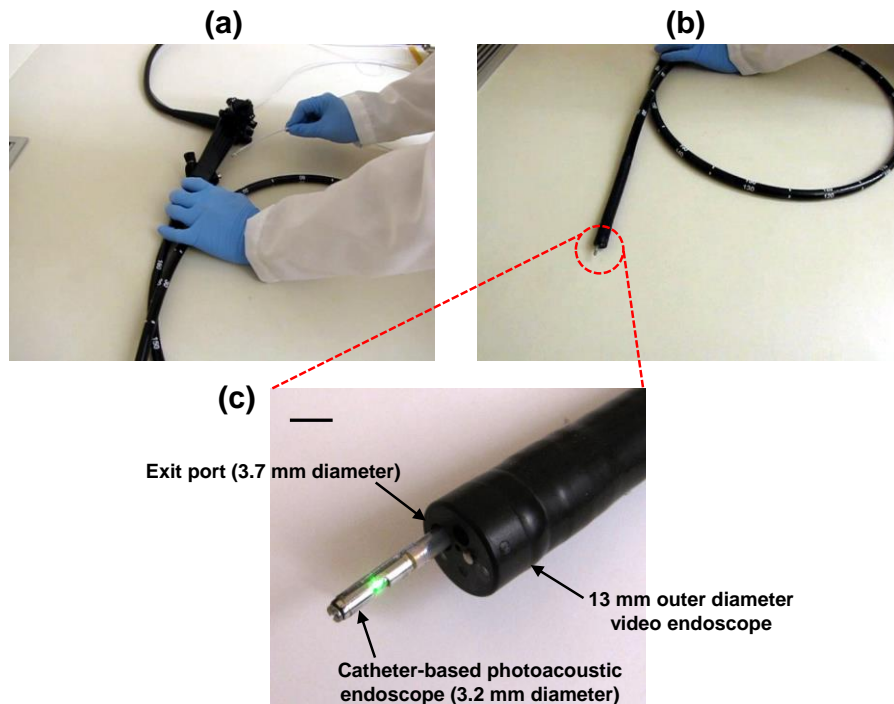
Figure 2.19. Photos of the catheter-based PAE probe positioned fully within **(a)** and projecting from **(b)** the 3.7-mm instrument channel of a clinical video endoscope. **(c)** Magnified view of (b).

Figure 2.18(c) shows a representative B-scan image acquired from the phantom. In this experiment, unlike the previous tungsten wire imaging experiment conducted in a clear medium [Figure 2.17(a)], laser pulses were delivered through the optical fiber enclosed in the catheter

50

endoscope because the targets were embedded in the scattering medium. As shown in the image, we could detect PA signals from the two objects with adequate signal-to-noise ratios. From the image, we plotted the transverse signal variations for the two needles in Figures 2.18(d) and (e). Based on the FWHMs of the two plots, we roughly estimated the transverse resolutions to be ~190 μm and ~450 μm at the two distances, respectively. Because Object 1 has a round surface and it is located at in the focal zone, the FWHM of the graph curve [Figure 2.18(d)] appeared to be even smaller than the actual diameter; one can see that only the areas of the two needle surfaces that were closer to the US transducer were visualized by the endoscope (especially Object 1).

To compare the experimental results with the theoretical values, we present in Figure 2.18(f) the theoretical resolution. As shown, the resolution values estimated by the two needles (Objects 1 and 2) are close to the theoretical values. However, the tungsten wire's resolution value showed a slightly closer agreement with the theoretical value. As the tungsten wire's resolution value was measured in water immersion, like the assumption of the simulation, the high agreement implies that the fabrication of the transducer was nearly ideal. Therefore, we can reasonably estimate the transverse resolution values at other distances from the theoretical curve.

After quantifying the resolution, we also tested the endoscope's intra-instrument channel workability. Because the endoscope's outer diameter is ~3.2 mm, we utilized the 3.7 mm diameter instrument channel of a clinical video endoscope (13911 NKS, Karl Storz). As shown in Figure 2.19(a) and Video 1, we were able to easily insert the catheter endoscope into the entry port of the instrument channel and also perform angulation smoothly along with the video endoscope. Figure 2.19(b) shows the tip of the catheter endoscope projected from the exit port of the video endoscope, and Figure 2.19(c) represents a magnified view of the catheter endoscope

emitting green laser light (532 nm). After performing a course of angulation and mechanical scanning, we were able to retract the probe uneventfully.

To demonstrate the endoscope's *in vivo* imaging capability, we imaged the upper esophagus of a New Zealand white rabbit (~4 kg, female, 7 months old, Harlan Laboratories). Because the typical diameter (~5 mm) of a rabbit's esophagus is much narrower than that of the video endoscope (~13 mm), we imaged the rabbit esophagus using only the PAE probe.

For the experiment, the rabbit was fasted, beginning ~12 hr before the experiments, to reduce the likelihood of ingesta in the stomach and esophagus. The rabbits were anesthetized with 35–50 mg/kg of ketamine and 5–10 mg/kg of xylazine via intramuscular injection. While anesthetized, the rabbit was intubated for maintenance of gas anesthesia (1.5–3.0% isoflurane). An endotracheal tube cuff was inflated to prevent aspiration of water into the lung. The rabbit was placed on an inclined stage (~10°) in supine position. Just before probe insertion, we filled the esophagus with water using an enteral feeding syringe connected to a rubber feeding tube (8–12 F or 2.7–4.0 mm). The water provided the necessary acoustic coupling and functioned as a lubricant during the imaging procedure. After filling the stomach and esophagus with water, we inserted the endoscopic probe through the mouth and advanced it approximately 25 cm, to the point at which the probe could no longer be gently advanced. Then, we performed pullback volumetric scans over a ~6 cm range during constant pullback translation of the probe by a motorized translation stage at a speed of ~150 μm/s. For this animal experiment, we set the gain of a signal amplifier at 40 dB, and acquired about 2000 B-scan slices with a longitudinal spacing of ~30 μm. Throughout the experiment, the rabbit's anesthesia level and vital signs were continuously monitored. After the experiment, the rabbit was euthanized by an overdose of sodium pentobarbital (150 mg/kg) injected in the marginal ear vein. All procedures in the

experiment followed the protocol approved by the Institutional Animal Care and Use Committee at Washington University in St. Louis.

In Figure 2.20, we present several postexperiment-processed PA B-scan images, covering a 160° angular FOV and 5.4 mm imaging depth, plotted on a linear [Figure 2.20(a) − (c)] and a logarithmic [Figure 2.20(d) − (f)] color scale. A partial pullback movie showing 800 B-scan slices is available in Video 3. As shown in the B-scan images [Figure 2.20(d) − (f)], the PAE system provided cross-sectional images of the esophagus and its neighboring anatomic structures. From our previous animal imaging experiments, we learned that the typical wall thickness of a rabbit esophagus is just ~400–600 μm (see the histologic image, Figure 2(i), in Reference [7]), and the neighboring space of the upper esophagus is occupied by the thymus and fat tissues, which are not very light absorptive (see the anatomic image, Supplementary Figure 7(a), in Reference [7]). In Figures 2.20 (d) − (f), we provide several landmarks, such as the esophageal wall, a surface of a neighboring organ [Figure 2.20(d)], and multiple blood vessels (the arrows) distributed in the mediastinum. As the endoscope was designed to work in direct contact mode, we could not detect PA signals when the probe's distance to the esophageal surface increased beyond approximately more than 1.5 mm (see the dotted lines in Figures 2.20(a) and 20(b)); this dead zone was due to the misalignment between the light illumination and acoustic detection [Figure 2.15]. Also, blood vessels in the esophageal wall were not clearly resolved because the acoustic focus was located ~2 mm away from the endoscope surface. If the surface of the esophageal wall, which has a thickness of less than 1 mm, is located at a distance beyond ~1.5 mm, the corresponding scanning area becomes a dead zone. Thus, all the esophageal walls imaged in this experiment were located within the 1.5 mm distance, i.e., out of optimal focus.

53
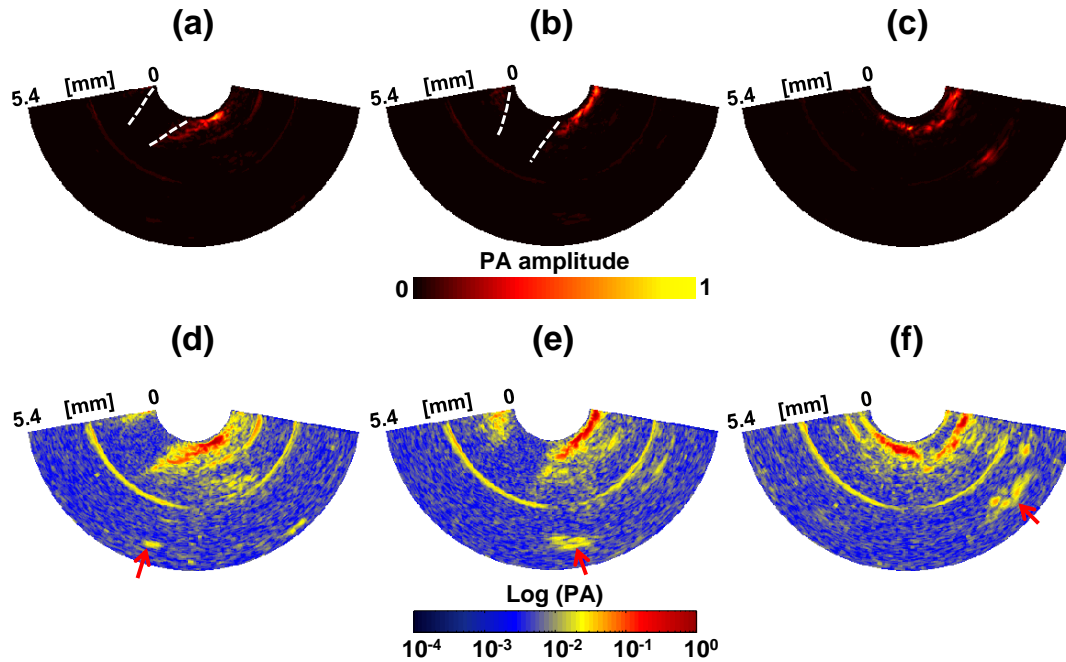
Figure 2.20. Representative PAE B-scan images of a rabbit esophagus acquired *in vivo* shown on **(a)**–**(c)** a linear and **(d)**–**(f)** logarithmic color scale. The images cover a ~14 mm diameter (i.e., ~5.4 mm radial imaging depth) and ~160° angular FOV. The left-hand side and lower portion of each image correspond to the left and the dorsal side of the animal, respectively. BS, bounceback signals; BV, blood vessel; EW, esophageal wall; SNO, surface of a neighboring organ.

In the presented B-scan images, one can also see arc-shape lines at ~3 mm depth; similar lines also appeared in our previous PAE images. From a couple of tests, we found that it is a bounceback signal (i.e., acoustic reflection) of the PA waves generated at the US transducer surface. Because the tip of the angle-polished optical fiber was cracked a little bit during the polishing and assembling process, whenever laser pulses are fired, stray light are generated, and some of them impinge on the transducer surface, which then create PA waves. At the same time, PA waves are also generated at the surface as well as deep regions of the target tissue. Consequently, some portions of the PA waves generated from the two sources started to propagate in opposite directions, and they reached the membrane and transducer surface,

54

respectively, after ~2 μs, which corresponds to the traveling time of acoustic waves for the distance (i.e., ~3 mm) from the plastic membrane to the transducer surface via the scanning mirror. The PA waves originating from the tissue are the true signals that we want to record. However, the PA waves originating from the transducer surface are also recorded after another 2 μs; which corresponds to the return travel time, i.e., from the membrane to the transducer. In the case of the tungsten wire imaging [Figure 2.19(a)], such an arc-shape line was not generated because it was acquired using external illumination, i.e., not using the endoscope's optical fiber.

With this *in vivo* imaging data, we also analyzed the scanning stability of the scanning mirror using the PA signals generated by the stainless steel bridge section [Figure 2.13(c)]; usually metallic objects generate strong PA signals because they are highly light absorbing. The result showed a greater fluctuation (8.6° rms) than the tungsten wire imaging experiment because the endoscope performed mechanical scanning while bent. In addition, we found that the nonuniformity of the rotation of the flexible shaft showed periodic changes in accordance with the respiratory motion of the animal. Due to this nonuniform rotation and the respiratory motion, we were unable to produce a radial maximum amplitude projection or a volumetric image.

With the entire system on a movable cart, we imaged patients and analyzed the oxygen saturation in different blood vessels in their esophagi. To the best of our knowledge, this was the first time PAE images were acquired from human esophagus *in vivo*. Different from pulse oximetry, which measures only the peripheral oxygen saturation of arterial blood, our technology can measure within each local blood vessel, including veins [Figure 2.21]. The result is a more direct indicator of the local metabolic level, and can potentially be used to differentiate between healthy and diseased tissue.
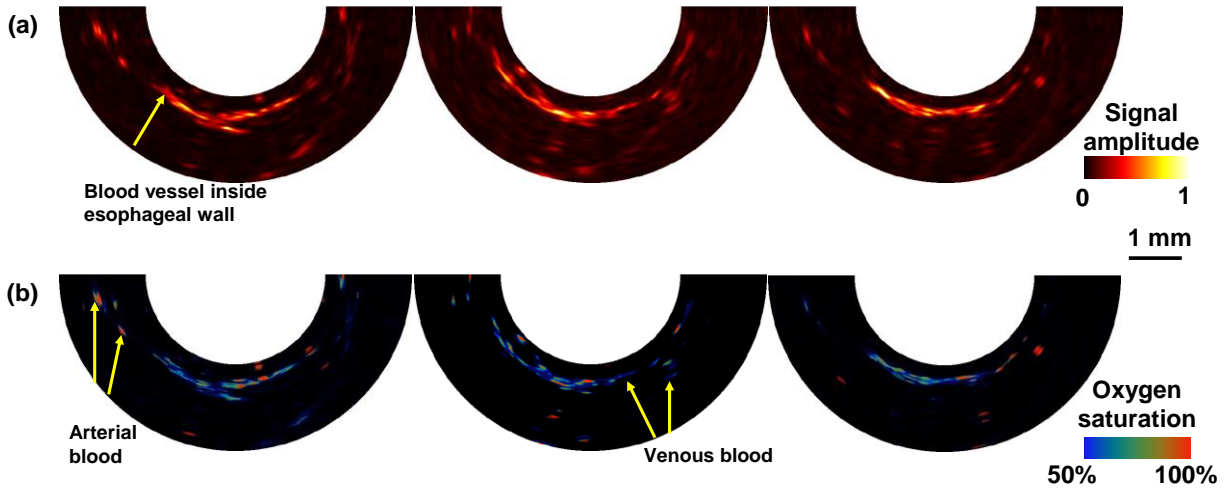
Figure 2.21. (a) PA B-scan images of human esophagus acquired at gastroesophageal junction *in vivo*. **(b)** Oxygen saturation map of esophagus based on multi-wavelength PAE.

Discussion   In this study, we implemented a new catheter-based PAE system and demonstrated its intra-instrument channel workability with a clinical video endoscope and in vivo imaging ability through an animal experiment. Compared with our previous micromotor-based endoscopes, this PAE probe has a more flexible and simplified distal structure with a smaller number of mechanical components, which promotes its clinical applicability. To transmit electric signals from the US transducer while minimizing interference noise, we employed a previously used static mounting method for the signal wire [Figure 2.15(a)]. However, we delivered the laser beam via a rotary junction formed at the proximal unit of the endoscope [Figure 2.11(a)]. Importantly, by using a flexible shaft instead of a micromotor [Figure 2.11(a)], we were able to achieve a rigid distal section length of only 16 mm, two times shorter than the previous micromotor-based endoscope, and to enable the catheter section to pass freely through the 3.7 mm diameter entry port of a video endoscope. Although other PA endoscopic systems [42,46] have been implemented with a similar proximal actuation mechanism, their imaging probes are not sheathed in a plastic tube and/or their in vivo imaging capabilities have not been

56

demonstrated. We believe that the presented PAE system is the first PA endoscopic system that has been implemented in a fully encapsulated form and sufficiently miniaturized to be usable for endoscopic imaging via the standard instrument channel of a clinical video endoscope.

With the prototype imaging system, we achieved a B-scan imaging speed of ~5 Hz (corresponding to an A-line acquisition rate of ~2 kHz and ~400 A-lines/B-scan), which is slightly faster than that (~4 Hz) of our previous micromotor-based endoscopic probes. However, we were not able to produce a volumetric image because of the nonuniform rotation of the scanning mirror; such nonuniform rotation was not a serious issue in the micromotor-based endoscopic probes. The slow scanning speed could be further improved by simply using a higher capacity step motor. However, first the mechanical friction between the shaft and the plastic sheath needs to be reduced to minimize the mechanical stress (torsion) caused by the angular phase delay between the proximal and distal ends of the flexible shaft. As we mentioned in the *in vivo* experiment results [Figure 2.20], the mechanical friction and the corresponding rotational nonuniformity increased as the catheter bent more because of the large thickness of the employed multimode optical fiber. An oil-based matching medium could be helpful in reducing the friction. However, high optical transparency and low acoustic attenuation are needed for a PA endoscope. If these requirements are satisfied, such an oil-based medium would also beneficially eliminate the acoustic matching medium injection and drainage procedure [Figure 2.16] because the medium could be retained in the catheter perpetually.

With the proposed optical design [Figure 2.13], we detected PA signals over a large imaging depth in the *in vivo* rabbit esophagus imaging experiment, although the laser beam firing direction did not coincide with the acoustic axis. However, because of the misalignment, we could not detect PA signals when the probe's distance to the target surface increased beyond

~1.5 mm [Figure 2.20(a) and (b)]; the endoscope must work in a direct contact to the optical scattering tissue. Also, PA images could be distorted when the US transducer's out-of-plane signals are stronger than the real in-plane signals. Thus, the next generation PAE system should improve the light-guiding optics in the scanning mirror to overlap the optical illumination and the acoustic detection, enabling it to cover the entire radial imaging depth. It was difficult to realize this in the current version because the diameter of the beam exiting the multimode optical fiber was very large compared to the available space in the scanning mirror unit. An optical fiber with a narrower diameter, such as a single-mode fiber, would be conducive to aligning the optical illumination and the acoustic detection. Another important challenge is to encase the entire probe in a single length of plastic catheter to increase flexibility. As the presented catheter endoscope system was specifically developed for intra-instrument channel use, this encasing method will make the catheter endoscope more durable and thereby safer.

In this study, we achieved a 3.2 mm probe diameter, allowing insertion of the probe in a 3.7 mm diameter instrument channel of a standard GI video endoscope; the main factor that determined the current probe diameter was the space required to accommodate the large diameter scanning mirror and the spherically-focused US transducer. However, achieving a smaller probe diameter, such as 2.5 mm, will make related PAE imaging probes compatible with even narrower instrument channels, such as 2.7 mm. In recent years, as a method for pursuing higher miniaturization, an optical ultrasound detection [47] and bundle fiber-based optical scanning [48] mechanism has been proposed by other groups. However, the optical signal detection method currently suffers from instability in the probe fabrication as well as the signal detection, and the image FOV of the bundle fiber-based optical scanning endoscope is narrow unless it performs

additional scanning. Nevertheless, those methods could be potentially good options because they can make related probes' design simpler and footprint smaller.

We have successfully implemented a prototype PAE system that has a 3.2-mm diameter and 2.5-m long catheter section, and demonstrated its endoscopic imaging ability through an *in vivo* rabbit esophagus imaging experiment. The endoscopic system can produce PA images with a B-scan frame rate of ~5 Hz and A-line acquisition rate of 2 kHz. Most notably, the 3.2-mm diameter catheter is small enough to pass through the 3.7-mm diameter standard instrument channel of a clinical video endoscope. With this endoscope, we will progress to imaging human subjects with Barrett's esophagus.

2.4   Optical Resolution Photoacoustic Transvaginal Imaging System with a Water-Immersible MEMS Scanning Mirror

Background   Cervical remodeling is a critical process during pregnancy. Premature remodeling of the cervix is linked to spontaneous preterm birth [19]. Current characterization of cervical remodeling is subjective and imprecise. A quantitative, non-invasive technique to measure the micro-structural and functional changes during remodeling would be invaluable in the early diagnosis of incipient preterm birth.

A handheld system for transvaginal imaging of the cervix needs a fast scanning speed. If the scanning speed is low and the scanning time is long, the image results will be affected by subject's or operator's motion. A microelectromechanical system (MEMS) usually performs faster scanning than a mechanical system because it uses resonant angular movement to scan over the field of view. Unlike mechanical raster scaning, MEMS scanning does not require linear movement of a heavy imaging head. Water-immersible MEMS [49] is ideal for PA application

because it can scan light and ultrasound beams at the same time. The optical illumination and acoustic detection remain confocal during scanning, so the system maintains good sensitivity.
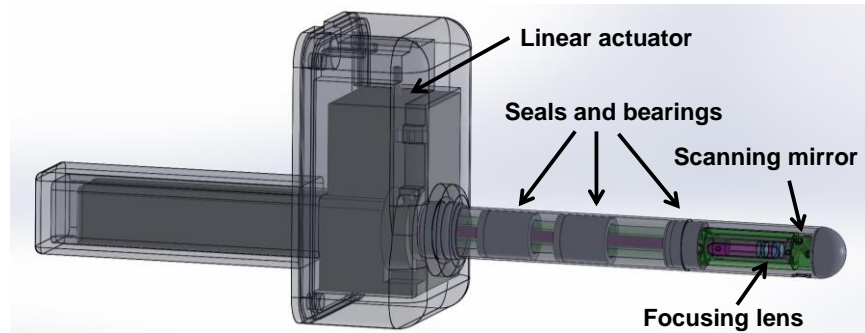

Figure 2.22. Representation of the optical resolution transvaginal imaging probe with a MEMS scanning mirror.

Methods We have designed and built an optical resolution, handheld PA imaging probe, based on a water-immersible MEMS scanning mirror, for transvaginal imaging of the human cervix. It has an outer diameter of 20 mm and a length of 17.5 cm, dimensions similar to those of a standard transvaginal ultrasound probe. Optical units at the distal end of the probe focus the laser beam onto the cervix and achieve optically defined lateral resolution. On the fast axis, it applies a MEMS mirror that scans at a resonant frequency of 220 Hz. Scanning on the slow axis is driven by a linear actuator. A volumetric scan over a 3 mm by 1.5 mm area takes 1.25 s. The probe body can be disinfected like any other transvaginal probe. Its handle is covered by a protective case, which can be disassembled and disinfected separately [Figure 2.22].

We first tested the probe by imaging a metal target and a leaf skeleton. To demonstrate its clinical potential, the imaging probe was then covered with a sterile plastic sheath and applied to human hysterectomy specimens. The sheath was replaced after each imaging session, a necessary procedure for infection prevention during clinical applications.

Results The system's LSF was extracted from the signal profile across a sharp metal edge [Figure 2.23(a)]. The FWHM shows that the system has a spatial resolution of 3.1 μm in the lateral direction. Small features of the metal target [Figure 2.23(b)] and the leaf skeleton phantom [Figure 2.23(c)] were clearly revealed.
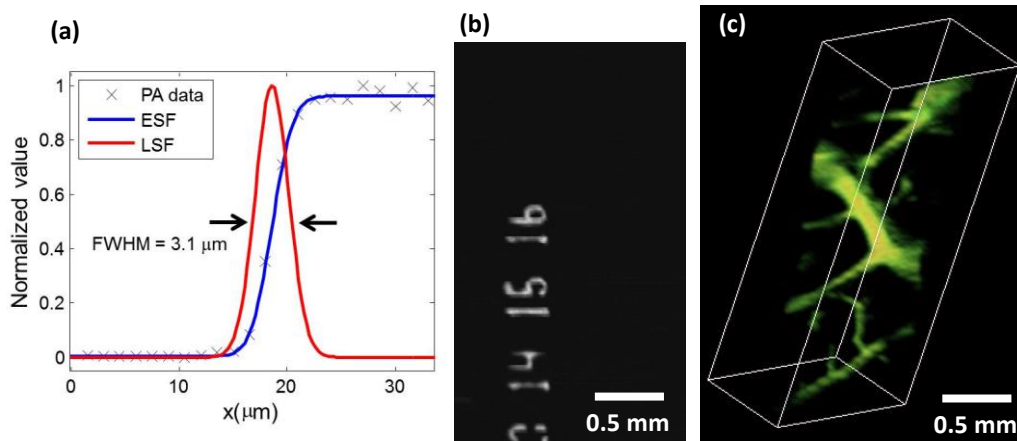
Figure 2.23. Experimental validations of the imaging probe. **(a)** System's ESF acquired by scanning across a sharp metal edge, and the extracted LSF. **(b)** 2D projected image of metal features on a transparent substrate. **(c)** 3D rendering of PA image acquired from a leaf skeleton phantom.

The imaging results from hysterectomy specimens, shown in Figure 2.24, prove that the system can achieve good spatial resolution when covered with a translucent standard transvaginal probe sheath. The PA images show that the uterus has long, straight blood vessels to supply the uterine wall. Blood vessels in the cervix are thinner, with more curves and loop.

Discussion The system demonstrated the ability to image blood vessels in the human cervix, and can be used for longitudinal studies of blood vessel networks during cervical remodeling. With imaging results acquired at different times during pregnancy, we can validate the probe as a non-invasive tool to stage the remodeling process. The result can contribute to detecting incipient preterm birth at an early stage.

Figure 2.24. PA images of human hysterectomy specimens, acquired by the optical resolution transvaginal imaging system, showing blood vessels in the uterine wall and cervix.

Chapter 3: Advanced Photoacoustic Imaging

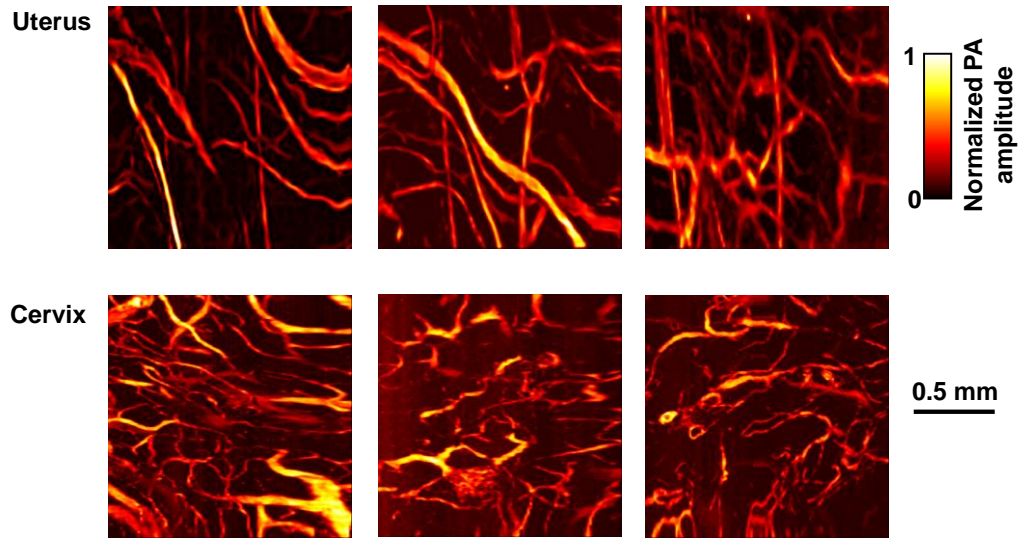## 3.1 Photoacoustic Recovery after Photothermal Bleaching

Background The ability to quantify the diffusion and binding of molecules in living cells provides a deep understanding of cellular dynamics [50,51]. Conventionally such measurements have been implemented mainly via fluorescence recovery after photobleaching (FRAP), a technique that relies on selectively photobleaching the fluorophores within a region of interest by a high intensity laser, followed by monitoring the diffusion of new fluorescent molecules into this bleached area over a period of time with a low intensity excitation [52]. By analyzing the temporal profile of the fluorescence signal recovery, the physical properties of molecules and their surrounding medium can be revealed [53].

One underlying assumption of FRAP is that further photobleaching is negligible during fluorescence recovery. However, since both photobleaching rate and fluorescence emission rate are proportional to the laser fluence [54], the requirement of low-power excitation often results in noisy images, degrading the fidelity of the fluorescence recovery profile. In addition, toxic radicals, such as reactive oxygen species, are generated as side products of photobleaching, a process which may interrupt normal cellular processes and jeopardize a cell's viability [55].

To overcome these limitations, we present an alternative method, photoacoustic recovery after photothermal bleaching (PRAP), for studying the localization, mobility, and transportation of cellular components. PRAP is the counterpart of FRAP in PAM, a high resolution imaging modality that has been widely used to gain a fuller understanding of varying cellular dynamics. The contrast agents in PAM can be either exogenous, such as metal nanoparticles [56,57], or

endogenous, such as hemoglobins [58], cytochromes [59], and DNA/RNA [60]. Analogous to photobleaching in fluorescence microscopy, the contrast agents in PAM can also be intentionally photothermally destroyed using strong excitation light. Upon the intense excitation, the contrast agents may undergo photothermal fragmentation, resulting in a shifted absorption peak and thereby a reduction of PA signals after exposure [61]. PRAP utilizes this effect and measures the recovery of PA signals owing to the diffusion of new absorbers into the bleached region, thus enabling the quantification of particle dynamics at micron scale via PA imaging.

In contrast to photobleaching in fluorescence microscopy, photothermal bleaching in PAM behaves quite differently before and after the absorbers are raised to a critical temperature by the excitation laser pulses. Below the pulse energy threshold corresponding to the critical temperature, the photothermal bleaching rate is small and has weak dependence on laser fluence; above it, the bleaching rate increases rapidly. This property is ideal for PRAP operation – the absorbers can be easily photothermally bleached with a relatively high intensity laser, and readily monitored with negligible bleaching at the stage of recovery using sub-threshold laser pulse energy. Additionally, since photothermal bleaching does not involve chemical destruction of a fluorophore as in FRAP, few reactive oxygen species are generated, much preferred for live cell imaging.

Methods   The PRAP experiments were performed on a previously developed optical-resolution PAM system [62]. PAM is a high resolution imaging technique that provides unique 100% optical absorption contrast [63]. In PAM, the sample is irradiated by a pulsed laser. Upon excitation, a portion of the light is absorbed by the object and partially converted to heat. Assuming thermal and stress confinements, the pressure immediately builds up within the heated

region and propagates as ultrasonic waves via thermoelastic expansion. By detecting the PA waves outside the sample, an optical absorption map inside the sample can be recovered.
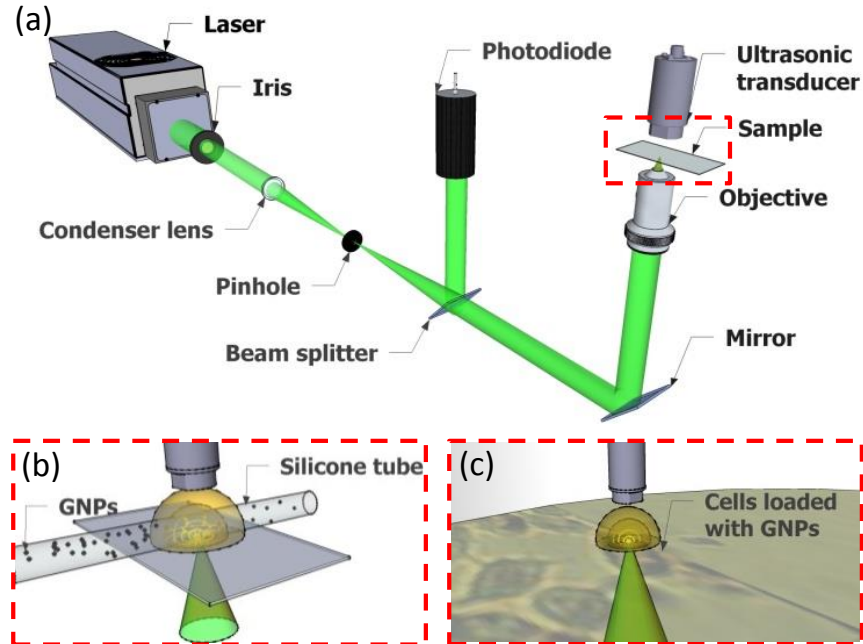
Figure 3.1. (a) Representation of the PAM system. **(b)** Representation of the setup for the phantom experiment. The sample and ultrasound transducer were immersed in water. **(c)** Representation of the setup for the cell experiment. The cells grew on the bottom of a petri dish and were immersed in phenol red-free culture medium.

The system setup is shown in Figure 3.1. A pulsed laser beam (5 ns pulse duration, 1 kHz pulse repetition rate) of 532 nm wavelength is generated by an OPO laser (NT242-SH, Ekspla), then spatially filtered through a pinhole of 50 μm diameter (P50C, Thorlabs). A microscope objective (Phaco1, 0.32 NA, Leitz Wetzlar) focuses the laser beam at the sample to induce PA waves. The PA waves are subsequently measured by a custom-made focused transducer (40 MHz central frequency, 80% bandwidth, 0.5 NA). In order to obtain a volumetric image, the sample is raster scanned in the transverse plane. To maximize sensitivity, the optical illumination and acoustic detection remain coaxial and confocal during scanning. The acquired PA signal is digitalized at

1GS/s by a digital acquisition board (PCI-5152, National Instruments), and corrected for fluence fluctuation pulse by pulse.

NIH 3T3 fibroblast cells were used in this study. The cells were maintained in Dulbecco's Modified Eagle Medium (DMEM) supplemented with 10% fetal bovine serum, 2 mM glutamine, penicillin, and streptomycin. Cells with medium were incubated at 37 C° in 5% CO_2 and divided every ~72 hours. For subculture, after being dispersed in 0.25% EDTA-trypsin, they were seeded at 2–4 $\times 10^4$ cells/cm^2.

24 hours after the cells were seeded to the bottom of culture dishes, 70-nm-diameter gold colloid was added to the culture medium to achieve a final colloidal particle concentration of 6 pM. The cells were incubated with the particles for another 24 hours for uptake.

Before imaging, the cells adhering to the bottom of culture dish were washed with fresh culture medium three times to remove residual particles. Then, to avoid the interference of phenol red in PA measurement as well as to maintain cell viability, the culture medium was switched to phenol red-free DMEM.

Cell slides were stained with LIVE/DEAD Viability kit (L-3224, Life Technologies). The cell slides were first rinsed with phosphate buffered saline (PBS) and then stained by 2 μM calcein AM and 4 μM ethidium homodimer in PBS for 45 minutes. After staining, the cell slides were washed with PBS and imaged with a fluorescence microscope. Green fluorescence images were acquired with a 450-490 nm excitation filter and a 500-550 nm emission filter. Red fluorescence images were acquired with a 530-585 nm excitation filter and a 575-630 nm emission filter.

Results   We validated PRAP first in a simple phantom study, and then in a more complex

diffusion rate measurement involving live cells. Gold nanoparticles (GNPs) were used as PA

imaging contrast agents because they offer superior chemical stability and are used extensively

in live cell imaging [64,65].
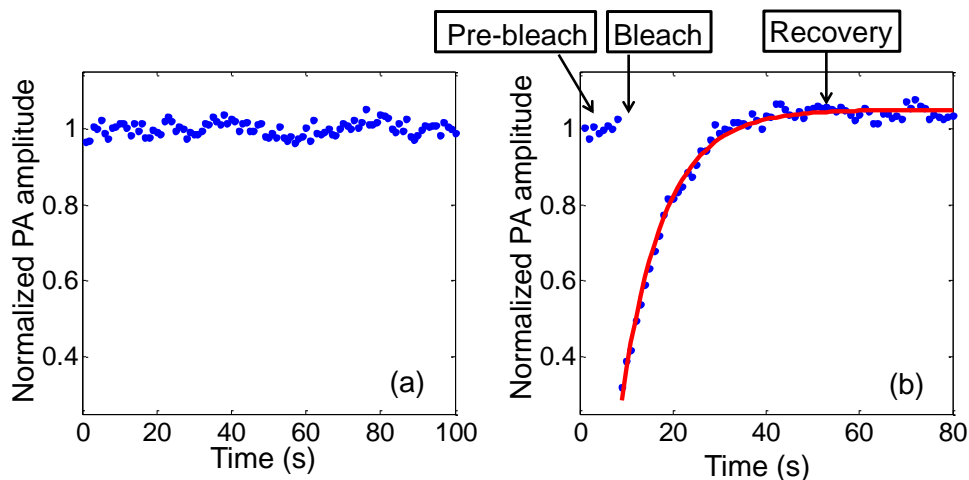
Figure 3.2. (a) PA measurement using low laser energy (~200 nJ/pulse) shows no bleaching effect.
(b) PA amplitude measured during bleaching and recovery of 120 pM, 70 nm colloidal GNPs in
deionized water. The PA signals acquired during photothermal bleaching are omitted in Figure 3.2(b).

We first measured the pulse energy threshold that corresponded to the onset of photothermal

bleaching of 120 pM, 70 nm diameter colloidal GNPs. The laser beam was focused into the

solution held in a silicone tube, and the PA signals were monitored over time to observe the

potential photothermal bleaching. The laser pulse energy was varied from 100 nJ to 800 nJ.

Little photothermal bleaching was observed until the laser pulse energy reached 550 nJ. Based

on the measurement, the pulse energies chosen for photothermal bleaching and PA recovery

measurement were 6000 nJ and 200 nJ, respectively.

The PRAP experiment started with a baseline, where the PA signals from GNPs were monitored

over 100 seconds with a pulse energy of 200 nJ (Figure 3.2(a)). The measured PA signal

amplitude was constant with an SNR of 35 dB. After that, the GNPs were illuminated with high-energy laser pulses for ~2 seconds, and the subsequent PA recovery temporal profile was recorded by PAM with low-energy pulses, as shown in Figure 3.2(b).

Under the assumptions of uniform particle concentration in the infinite surrounding medium and negligible diffusion during photothermal bleaching, the PA signal recovery is governed by

$$P(t) = P_\infty - (P_\infty - P_0)\exp(-kt), \tag{1}$$

where $P(t)$ denotes the time-lapsed PA signal, P_∞ represents the asymptotic value when time t tends to infinity, P_0 is the instantaneous PA amplitude observed immediately after photothermal bleaching, and k is the PA recovery rate. Fitting the PA recovery profile in Figure 3.2(b) by Eq. (1) yielded a k of 0.11 s^{-1}.
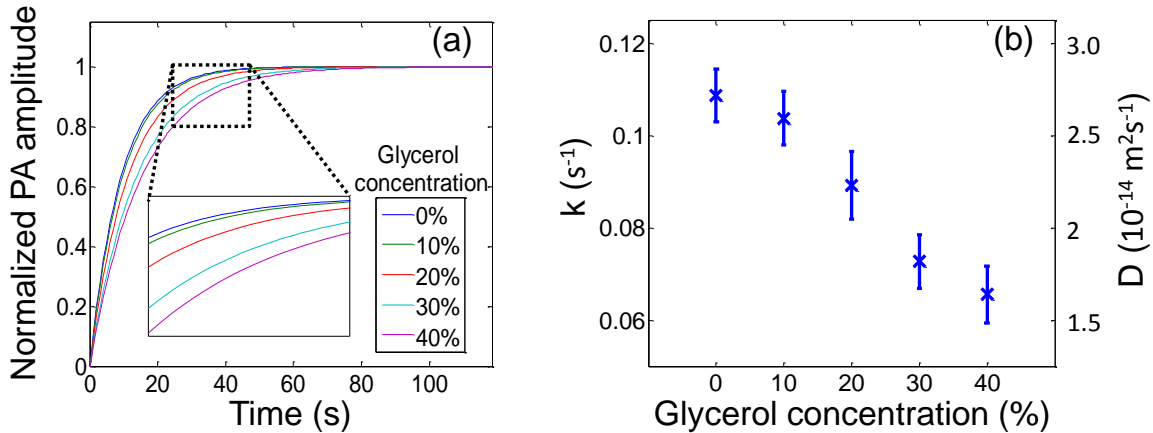
Figure 3.3. **(a)** PRAP in glycerol aqueous solutions with different concentrations. **(b)** Recovery rate and diffusion coefficient in each solution. Error bars show 95% confidence bounds.

Then we prepared GNP solutions with volume concentrations of glycerol of 0%, 10%, 20%, 30%, and 40%, respectively. These five samples had the same particle concentration, 120 pM, and were studied with PRAP sequentially. By fitting the PA recovery temporal profiles to Eq.

68

(1) (Figure 2.3(a)), the recovery rates k at different glycerol concentrations were derived (Fig. 3(b)). In addition, the diffusion coefficient D was calculated by

$$D = \frac{1}{4} w^2 k , \tag{2}$$

where w is the radius of the bleached area [66]. The results are shown in Figure 3.3(b). Here w was estimated to be 1.0 µm, half of the zero-point width of the main lobe of the optical focus. As expected, both the PA recovery rate k and the medium diffusion coefficient D decrease with an increase in glycerol concentration, indicating a slower particle diffusion rate in a medium of higher viscosity.

To validate the results acquired by PRAP, we used the fluorescence-based approach to re-measure the particle diffusion rate in a 40% glycerol solution. The experiment was performed on a laser scanning confocal microscope (Fluoview FV1000, Olympus) equipped with a FRAP module. We added Rhodamine 6G as a fluorescent indicator to the mixed glycerol aqueous solution. An area of the same size as in PRAP was photobleached, and the subsequent fluorescent recovery profile was recorded and analyzed by the fluorescence microscope. The diffusion coefficient measured by FRAP was 5.0×10^{-13} $m^2 s^{-1}$ for the 40% glycerol aqueous solution. Based on the Stokes-Einstein model [67], the diffusion rate is inversely proportional to the particle diameter. Here the diffusion rates measured by FRAP and PRAP varied by approximately 31 times (5.0×10^{-13} $m^2 s^{-1}$ versus 1.6×10-14 $m^2 s^{-1}$) while the particle sizes in the two cases varied by approximately 70 times (~1 nm versus ~70 nm). Therefore, the PRAP measurements correlated strongly with the expected diffusion dynamics of GNPs in solution.
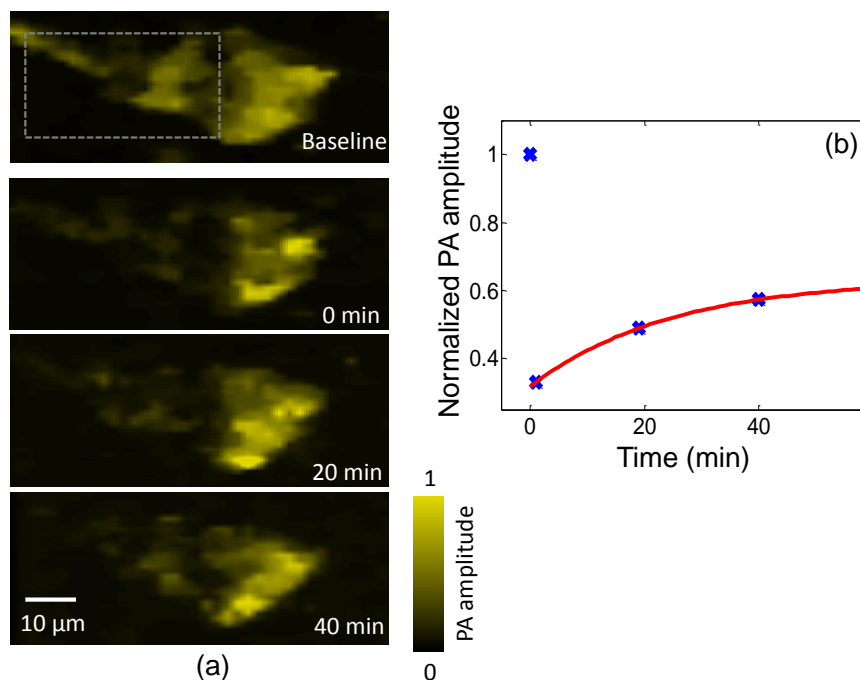
Figure 3.4. (a) PRAP in a cell over time. Dashed block shows the bleaching region. **(b)** PA amplitude of the bleached region measured before bleaching and during recovery.

Finally, to demonstrate PRAP in cell imaging applications, we loaded GNPs into an NIH 3T3 fibroblast cell and applied PRAP to measure the intracellular particle diffusion rate. The cell was raster scanned in the transverse plane to accomplish a C-scan. A region of interest was first chosen within a cell and photothermally bleached as shown in the top two frames of Figure 3.4(a). Then the PA signals from the bleached area were monitored over 40 minutes (Figures 3.4(a) and (b)). Here the PA signals were calculated by averaging all pixels within the bleached region. Since the bleached area covered ~50% of the cell, the conservation of unbleached particles within the cell results in that the final PA signal was recovered to only ~57% of the initial value. It is worth noting that the measured particle diffusion rate was relatively slow, attributed to the relatively large size of the bleached area. Additionally, the intracellular components form a filamentous meshwork, which restricts diffusion as a cytosolic sieve [68,69].

70

Moreover, the GNPs tend to aggregate upon cellular uptake [70]. The aggregation of GNPs increases particles' effective diameters and thereby slows down their diffusion. Depending on particle physicochemical properties (size, charge, coating, etc.) [71] and cellular biochemical conditions [72], the formed cluster size varies. This variation in cluster size may impact the quantitative analysis of PRAP. To overcome this problem, the GNPs can be delivered into cells through microinjection [73] instead of cellular endocytosis. Furthermore, when PRAP is performed outside of cells, such as on cell membranes, there is no aggregation, and therefore the analysis will not be affected.

To test their effect on living cells, all cells in a square area were entirely bleached by the PA and fluorescence methods, respectively. In PRAP, we used the same laser pulse energy as that in other PA cell imaging experiments. For the photobleaching of fluorescence dye, a 225 μW, 488 nm laser was utilized, and the scanning duration was 180 s. For a fair comparison, the cells were illuminated by the laser until they were fully bleached as that in PRAP. The cellular viability was tested by fluorescent staining. The results show that, with our experimental setup, 51% of cells were still viable after the PRAP experiment, compared to 5% after conventional FRAP (Figure 3.5). It is worth noting that the survival rate by FRAP here is significantly lower than that in other reported FRAP experiments because here the whole cell rather than a small cellular portion was photobleached.

Discussion We presented a new PA-imaging-based method, PRAP, for measuring intracellular diffusion rate. The experimental results demonstrated that PRAP has the capability to measure the mobility of particles in a viscous medium. In contrast to the conventional fluorescence-based approach, PRAP acquires high SNR images with negligible bleaching-induced artifacts during PA recovery.

71
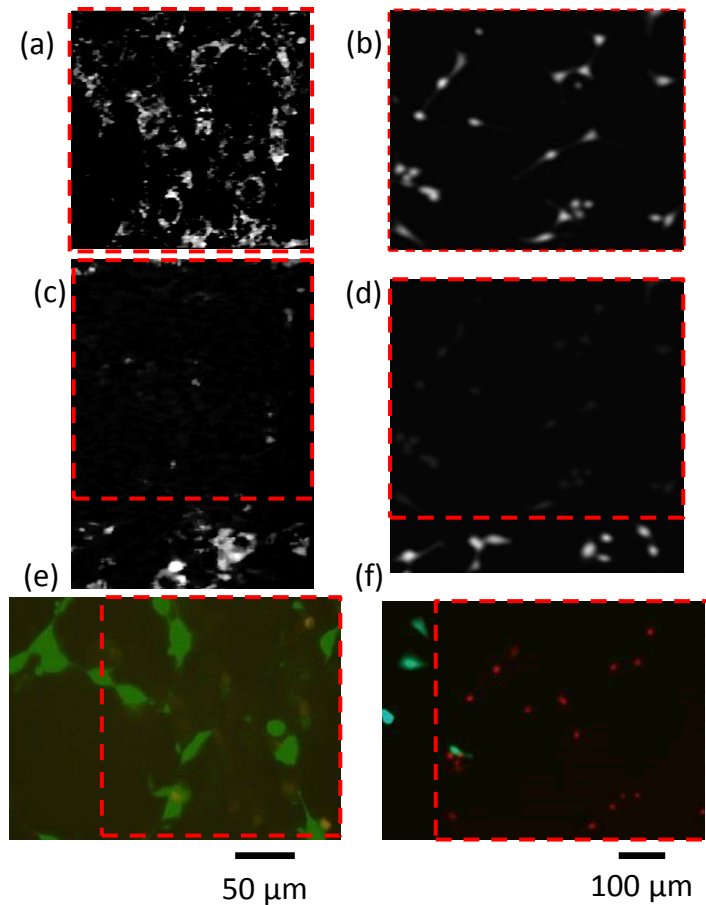
Figure 3.5. (a) PAM image of cells loaded with GNPs. **(b)** Confocal microscopy image of cells stained with calcein AM. **(c)** PAM images showing the same region as (a) was photothermally bleached. **(d)** Confocal microscopy image showing the same region as (b) was photobleached. **(e) (f)** Live/dead fluorescent staining of the cells in the bleached regions by PAM and confocal microscopy, respectively. Live cells emit green fluorescence while dead cells emit red. (a), (c), and (e) have the same scale. (b), (d), and (f) have the same scale.

PRAP has the potential to facilitate nontoxic biological studies of diffusion at different scales. In the presented cellular experiment, GNPs were used to indicate the motion of cytoplasm. In the future, GNPs can be tagged to specific molecules or organelles via controlled labeling [74], enabling studies of their intracellular diffusion. The performance of PRAP can be further improved by utilizing optimized PA contrast agents, such as silica-coated gold nanorods [75], which exhibit smaller size, less disturbance to a living system, and higher PA excitation

72

efficiency. Additionally, although not demonstrated here, PRAP can also be employed in biological tissues, allowing visualization and quantification of diffusive and kinetic processes at depths.

3.2 Photoacoustic Imaging of Nanosensors to Monitor Therapeutic Lithium *in Vivo*

Background Compared to conventional optical imaging, PAT is less affected by scattering in biological tissue and can achieve imaging depths up to several centimeters with acoustically defined spatial resolutions [5]. Although PAT has proven capable of imaging based on both endogenous contrast and exogenous contrast agents [76], most studies have been limited to measuring static or slowly-changing signals from samples. However, revealing many important fast-changing physiological processes *in vivo* requires continuous and noninvasive monitoring of analyte concentration levels in deep tissue over a long period of time.

Lithium is a standard and effective treatment for bipolar disorder, but it has a narrow therapeutic concentration range (0.6–1.2 mM) and a low toxic dose (~ 2 mM) [77] in humans. Blood sampling requires repeatedly acquiring blood drops from the patient to achieve semi-continuous monitoring for treatment management. Non-invasive and continuous monitoring of lithium concentration using PAT would simply this procedure and facilitate a steady therapeutic lithium concentration for effective and safe treatment.

In this work, we developed, characterized, and validated lithium-sensitive nanosensors for photoacoustic measurements *in vivo*. The nanosensors, modified based on well-established fluorescent nanosensors [78], could be tuned to respond to certain types of analyte at physiologically relevant concentration ranges.

73

Methods   Two photoacoustic tomography systems were used for this research. For *in vitro* phantom experiments, photoacoustic computed tomography (PACT) was used as detailed in [79, 80].   Briefly, a tunable optical parametric oscillator laser (basiScan 120, Spectra-Physics) pumped by an Nd:YAG laser (Brilliant b, Quantel) with a 10 Hz pulse repetition rate was used to excite photoacoustic waves. Light exiting the laser system was homogenized by an optical diffuser and then illuminated the sample. The photoacoustic waves were detected by a 512-element circular transducer array (Imasonic) with a 5 MHz central frequency. The imaging system had a 0.10 mm radial resolution and a 0.10-0.25 mm tangential resolution. The image was reconstructed based on the back projection algorithm.

For *in vivo* monitoring experiments, we used a deep reflection-mode photoacoustic tomography system detailed in [81]. Briefly, a dark-field focusing illumination was achieved through a series of optical elements from the same laser source as above. The optical fluence at the animal surface was controlled to be below the maximum permissible exposure of the American National Standards Institute [25]. A photodiode (SM05PD1A, Thorlabs) was used for monitoring and compensating the fluctuation of the laser energy. The excited ultrasound waves were detected by a 10 MHz central frequency focused transducer (V315, Panametrics-NDT), and the signals were then amplified by an amplifier (5072PR, Panametrics-NDT) and digitized by an oscilloscope (ZT4421, ZTEC Instruments). The imaging system was mounted on a linear translation stage (XY-6060, Danaher Motion) to acquire three-dimensional information. The spatial resolution of the system was about 0.17 mm and 0.29 mm in the axial and lateral directions, respectively.

For *in vitro* measurements, silicone tubing was filled with mixtures of nanosensors and lithium with different concentrations then sealed by rubber plugs at both ends. The sealed tubing was embedded in agar gel and covered by chicken breast tissue for imaging.

The mice used in this research were Hsd:Athymic Nude-Foxn1[nu] from Harlan Laboratories. Photoacoustic imaging experiments were conducted using the system described above. Animals were anesthetized with 1.5% isoflurane in oxygen, and 40 μL of nanosensors was injected intradermally into the mouse back. The animals were then imaged at excitation wavelengths 515 nm and 660 nm. Baseline raster scan images were acquired at both wavelengths, and continuous monitoring was done with both wavelengths along a line on the fast scanning axis and across the center of the nanosensor injection. Data points were acquired approximately every minute after an intraperitoneal injection of 38 mg/kg lithium (administered as lithium chloride in PBS, experimental group) or a matching volume of PBS (control group). Measurements were recorded every minute for approximately one hour. All animals were sacrificed after the experiments were completed.

For data analysis of each experiment, the photoacoustic amplitude from the 515 nm signal was divided by that from the 660 nm signal. These ratios were normalized to the first time point after lithium injection, and linearly interpolated to align time and intensity points before averaging measurements within each group.

Results The mechanism for lithium ion recognition and measurement by these nanosensors is based on the well-established optode approach [82–85]. Lithium is selectively extracted into a hydrophobic polymer core [86], shifting the pH in the nanosensor core. The spectral character of the nanosensor changes when its protonation state changes [Figure 3.6]. Therefore, the absorption spectrum of the nanosensors changes as a function of lithium concentration in the medium.
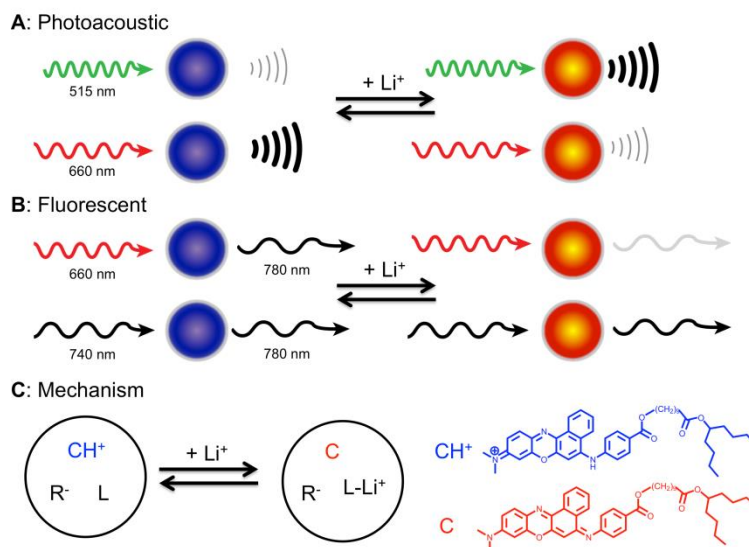
Figure 3.6. Nanosensors for lithium detection can be monitored with either PA **(A)** or fluorescence **(B)** imaging techniques. The approach uses multi-wavelength ratiometric imaging to generate a response that changes with lithium concentration. **(C)** The fundamental mechanism of the lithium response is lithium extraction by an ionophore (L) into the core of the nanosensor, which deprotonates a chromoionophore (CH+) and changes the optical properties of the nanosensor. An additive (R-) balances the charge inside the sensor.

Photoacoustic imaging is based on the absorption of photons by a molecule and the subsequent conversion to ultrasonic waves via the photoacoustic effect. When the absorption spectrum of the chromophore changes, its photoacoustic spectrum will also change [Figures 3.6(A), 3.7(A)]. As the lithium concentration increases, the absorbance and photoacoustic signal at 515 nm increase, and the absorbance and photoacoustic signal at 660 nm decrease. We can form a ratiometric measurement from these two wavelengths [Figure 3.7(B)] that increases linearly with lithium concentration but is not affected by common artifacts such as variations in nanosensor concentration. These nanosensors were also photoacoustically imaged under ~1.5 mm of chicken breast tissue [Figure 3.7(C)(D)]. The ratiometric values from the phantom remain linear over the physiologically relevant range of lithium.
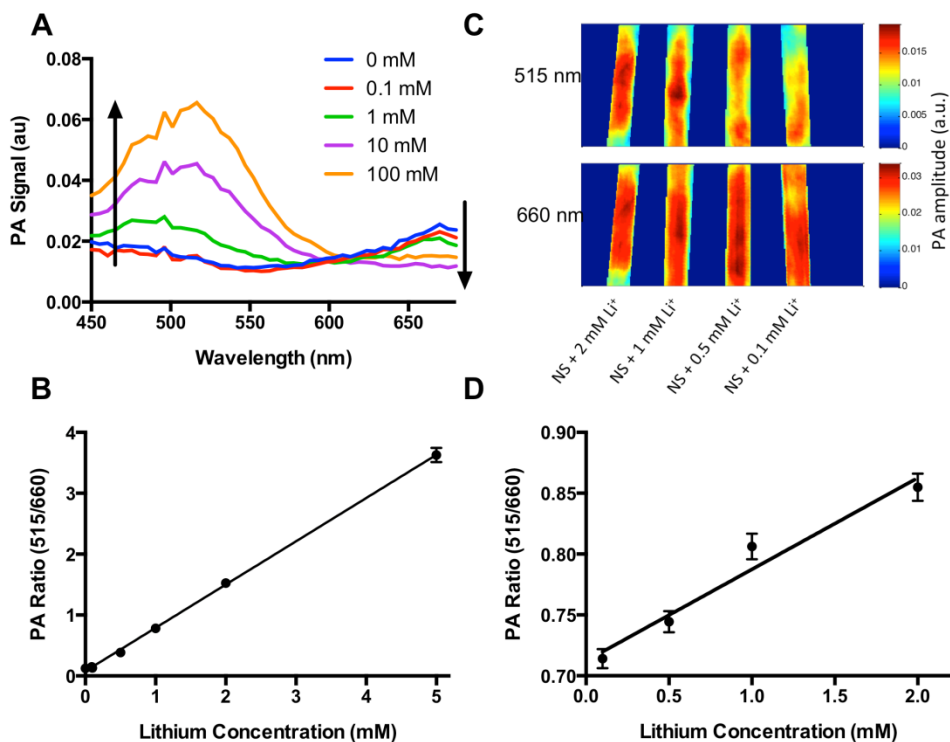
Figure 3.7. Photoacoustic nanosensors respond to lithium at physiological ranges. The photoacoustic spectrum **(A)** has two peaks centered at 515 and 660 nm. The 515 peak increases with lithium concentrations, and the 660 peak decreases. The ratio of these two signals **(B)** responds to lithium and is insensitive to common confounding factors such as the concentration of nanosensors. Photoacoustic imaging of nanosensors under a 1.5 mm thick layer of chicken tissue **(C)** shows signal attenuation of the 515 nm peak, while retaining the ratiometric lithium response **(D)**.

Lithium-selective nanosensors injected into the skin of mice can be imaged with photoacoustic tomography [Figure 3.8(A)], enabling data to be collected from the entire tissue volume [Figure 3.8(B)]. Importantly, the data collected is a result of the entire sensor injection, rather than just the nanosensors closest to the skin surface, as is the case with fluorescence imaging. Upon intraperitoneal administration of lithium to the animals at a physiological concentration of 200 mg/kg (~2 mM blood concentration), the nanosensor photoacoustic signal ratio increased as expected. Error bars for lithium dataset represent the standard deviations of three animals in the experimental group. The concentration response reached a peak at 14 minutes [Figure 3.8(C)],

compared with 2 hours for humans [87]. It is already known that lithium elimination pharmacokinetics are an order of magnitude more rapid in mice than in humans [88], so it is likely that the peak time is also faster due to these increased kinetics. Importantly, this data was acquired without blood sampling, and from the entire depth of the nanosensors. It measured sensors close to the capillary bed, which should minimize response lag time and more accurately reflect blood concentrations.
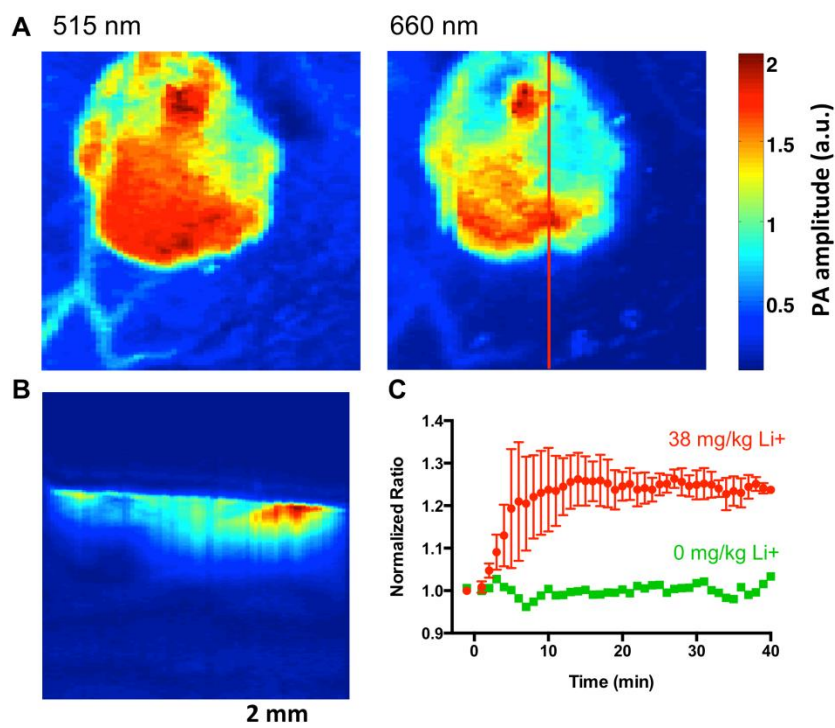
Figure 3.8. PA nanosensors imaged in mice. Dual wavelength images of the nanosensor injection using photoacoustic tomography **(A)** clearly show the boundary of the injection. A depth profile **(B)** taken along the red line in (A) shows the depth profile of the nanosensor injection. The response of nanosensors to systemic lithium administration **(C)** for three animals yields a time to maximum lithium concentration of 14 minutes (experimental group n=3, control group n=1).

Discussion   This is the first report of photoacoustic imaging to measure therapeutic drug concentrations *in vivo*. Imaging nanosensor injections in 3D solves several problems with current fluorescence-based approaches because the depth profile separately measures sensor responses in

regions closest to the capillary bed. For larger molecules such as glucose, the differences between values near the capillary bed and skin surface may be significant [89], and photoacoustic imaging may provide superior diagnostic power. For lithium concentration *in vitro* and lithium kinetics *in vivo*, photoacoustic measurements were similar to those from fluorescence imaging, demonstrating that the multimodal imaging does not alter the mechanism of the sensors and highlighting the robustness of the platform and earlier nanosensor development work.

A common limiting factor for temporal resolution in basic and clinical pharmacokinetic research is the need for blood sampling. This work demonstrates the first *in vivo* real time tracking of lithium levels without blood sampling. Lithium is a common and potent treatment for bipolar disorder, but its narrow therapeutic window and low toxic dose make it more difficult to dose than other pharmaceutical therapies. A minimally-invasive continuous monitor for blood lithium concentrations would be highly useful for dose administration and management [77]. Nanosensors produce a ratiometric photoacoustic signal that responds to lithium concentrations *in vivo*. These processed multi-wavelength signals are less affected by sensor concentration and sensor injection depth than single wavelength intensity measurements. In the larger context of continuous physiologic monitoring, this modular nanosensor platform translates directly to other electrolytes and to small molecules, such as histamine. The results herein show that photoacoustic imaging is a measurement mode for nanosensors that can provide previously unattainable measurement depths, an invaluable asset to chronic disease management.

Chapter 4: Summary

We have developed miniature and handheld PAE systems for various applications, including gastroesophageal tract imaging, abdomen cavity imaging, and urogenital system imaging.

We designed and implemented a dual-mode PA and US rigid probe for comprehensive use in human urogenital imaging [90], and demonstrated its endoscopic workability through animal experiments. The endoscopic probe enabled simultaneous PA and US imaging with a B-scan frame rate of 6.25 Hz, which was limited by the pulse repetition rate of the laser system; we also demonstrated that the mechanical rotation speed can exceed 20 Hz. Compared with previous micromotor-based endoscopes [7,8], the main difference in the probe design is that the locations of the US sensor and mechanical actuation source are switched, while the static mounting strategy of the light delivery and acoustic detection units is maintained. By relocating the mechanical source to the proximal part, a space restriction for the motor was eliminated at the distal end; thereby we were able to use a more powerful motor.

We also implemented the first OR-PAEM system with a full IVM imaging capability and achieved a transverse resolution as low as 10 µm, the finest among reported optical-resolution endoscopic PA images, and an SNR of 29 dB for a 3-µm diameter microsphere illuminated by a 500-nJ pulse energy in a beam of 9.2 µm in diameter [91]. Also, by using 532-nm and 559-nm wavelength laser, we acquired the first *in vivo* OR-PAEM image from a rat colorectum with tumor and produced a three-dimensional vasculature image with an apparent resolution of less than 30 µm. Then we analyzed oxygen saturation of the colorectal tumor. As the system can be utilized in small animals and also can potentially accommodate many other multi-functional

molecular probes, it could be a useful tool in many biological experiments. Moreover, the OR-PAEM's unique label-free imaging capability would enhance IVM's role in such clinical circumstances where the uses of contrast agents are undesired.

We have successfully implemented a prototype PAE system that has a 3.2-mm diameter and 2.5-m long catheter section, and demonstrated its endoscopic imaging ability through an *in vivo* rabbit esophagus imaging experiment [34]. The endoscopic system can produce PA images with a B-scan frame rate of ~5 Hz and A-line acquisition rate of 2 kHz. Most notably, the 3.2-mm diameter catheter is small enough to pass through the 3.7-mm diameter standard instrument channel of a clinical video endoscope. With this system, we imaged esophagi of human subjects.

To advance PA imaging, we presented a new PA-imaging-based method, PRAP, for measuring intracellular diffusion rate [92]. The experimental results demonstrated that PRAP has the capability to measure the mobility of particles in a viscous medium. In contrast to the conventional fluorescence-based approach, PRAP acquires high SNR images with negligible bleaching-induced artifacts during PA signal recovery.

We also performed the first work of photoacoustic imaging to measure therapeutic drug concentrations *in vivo* [93]. Imaging nanosensor injections in three-dimensions solves several problems with current fluorescence-based approaches because the depth profile separately measures sensor responses in regions closest to the capillary bed. The results herein show that photoacoustics is a measurement mode for nanosensors that can provide previously unattainable measurement depths, which can have profound effects on chronic disease management.

References

[1]   J. Yao, K. I. Maslov, Y. Zhang, Y. Xia, and L. V Wang, "Label-free oxygen-metabolic photoacoustic microscopy in vivo.," *J. Biomed. Opt.* **16**(7), 76003 (2011) [doi:10.1117/1.3594786].

[2]   L. Li, R. J. Zemp, G. Lungu, G. Stoica, and L. V Wang, "Photoacoustic imaging of lacZ gene expression in vivo.," *J. Biomed. Opt.* **12**(2), 20504 (2007) [doi:10.1117/1.2717531].

[3]   V. Ntziachristos and R. W. Ko, "Multispectral opto-acoustic tomography of deep-seated fluorescent proteins in vivo" (2009) [doi:10.1038/NPHOTON.2009.98].

[4]   J. Yao, J. Xia, K. I. Maslov, M. Nasiriavanaki, V. Tsytsarev, A. V Demchenko, and L. V Wang, "Noninvasive photoacoustic computed tomography of mouse brain metabolism in vivo.," *Neuroimage* **64**, 257–266, Elsevier Inc. (2013) [doi:10.1016/j.neuroimage.2012.08.054].

[5]   L. V. Wang and S. Hu, "Photoacoustic tomography: in vivo imaging from organelles to organs.," *Science (80-.).* **335**, 1458–1462 (2012) [doi:10.1126/science.1216210].

[6]   J.-M. Yang, K. Maslov, H.-C. Yang, Q. Zhou, K. K. Shung, and L. V. Wang, "Photoacoustic endoscopy.," *Opt. Lett.* **34**(10), 1591–1593 (2009).

[7]   J.-M. Yang, C. Favazza, R. Chen, J. Yao, X. Cai, K. Maslov, Q. Zhou, K. K. Shung, and L. V Wang, "Simultaneous functional photoacoustic and ultrasonic endoscopy of internal organs in vivo.," *Nat. Med.* **18**(8), 1297–1302, Nature Publishing Group (2012) [doi:10.1038/nm.2823].

[8]   J.-M. Yang, R. Chen, C. Favazza, J. Yao, C. Li, Z. Hu, Q. Zhou, K. K. Shung, and L. V Wang, "A 2.5-mm diameter probe for photoacoustic and ultrasonic endoscopy.," *Opt. Express* **20**(21), 23944–23953 (2012).

[9]   K. Jansen, A. F. W. van der Steen, H. M. M. van Beusekom, J. W. Oosterhuis, and G. van Soest, "Intravascular photoacoustic imaging of human coronary atherosclerosis.," *Opt. Lett.* **36**(5), 597–599 (2011) [doi:10.1364/OL.36.000597].

[10]   B. Wang, A. Karpiouk, D. Yeager, J. Amirian, S. Litovsky, R. Smalling, and S. Emelianov, "Intravascular photoacoustic imaging of lipid in atherosclerotic plaques in the presence of luminal blood," *Opt. Lett.* **37**(7), 1244–1246 (2012).

[11]   J. Menzel and W. Domschke, "Gastrointestinal miniprobe sonography: The current status," *Am. J. Gastroenterol.* **95**(3), 605–616 (2000) [doi:10.1016/S0002-9270(99)00891-6].

[12]   Z. Yaqoob, J. Wu, E. J. McDowell, X. Heng, and C. Yang, "Methods and application areas of endoscopic optical coherence tomography.," *J. Biomed. Opt.* **11**(6), 63001 (2011) [doi:10.1117/1.2400214].

[13] A. Jemal, F. Bray, and J. Ferlay, "Global Cancer Statistics," *CA A Cancer J. Clin.* **61**(2), 69–90 (2011) [doi:10.3322/caac.20107.Available].

[14] D. Hanahan and R. A. Weinberg, "Hallmarks of Cancer : The Next Generation," *Cell* **144**(5), 646–674, Elsevier Inc. (2011) [doi:10.1016/j.cell.2011.02.013].

[15] J. a Nagy, S.-H. Chang, S.-C. Shih, A. M. Dvorak, and H. F. Dvorak, "Heterogeneity of the tumor vasculature.," *Semin. Thromb. Hemost.* **36**(3), 321–331 (2010) [doi:10.1055/s-0030-1253454].

[16] O. Warburg, "On the Origin of Cancer Cells," *Science (80-.).* **123**(3191), 309–314 (1956).

[17] P. P. Hsu and D. M. Sabatini, "Cancer cell metabolism: Warburg and beyond.," *Cell* **134**(5), 703–707 (2008) [doi:10.1016/j.cell.2008.08.021].

[18] M. of Dimes, "2015 PREMATURE BIRTH REPORT CARD" (2015) [doi:10.1017/S1537592715001255].

[19] J. M. Gonzalez, Z. Dong, R. Romero, and G. Girardi, "Cervical remodeling/ripening at term and preterm delivery: The same mechanism initiated by different mediators and different effector cells," *PLoS One* **6**(11) (2011) [doi:10.1371/journal.pone.0026877].

[20] S. A. Cannistra and J. M. Niloff, "Cancer of the uterine cervix," *N. Engl. J. Med.* **334**(16), 1030–1038 (1996).

[21] M. A. Yaseen, S. A. Ermilov, H.-P. Brecht, R. Su, A. Conjusteau, M. Fronheiser, B. A. Bell, M. Motamedi, and A. A. Oraevsky, "Optoacoustic imaging of the prostate: development toward image-guided biopsy.," *J. Biomed. Opt.* **15**(2), 21310 (2013) [doi:10.1117/1.3333548].

[22] W. Xing, L. Wang, K. Maslov, and L. V Wang, "Integrated optical- and acoustic-resolution photoacoustic microscopy based on an optical fiber bundle.," *Opt. Lett.* **38**(1), 52–54 (2013).

[23] R. H. Hawes and P. Fockens, *Endosonography* (2010).

[24] C. Zhang, K. Maslov, J. Yao, and L. V Wang, "In vivo photoacoustic microscopy with 7 . 6-μm axial resolution using a commercial 125-MHz ultrasonic transducer transducer," *J. Biomed. Opt.* **17**(11) (2012) [doi:10.1117/1].

[25] Lasers Institute of America, *American National Standard for Safe Use of Lasers* (2007).

[26] D. Fukumura, D. G. Duda, L. L. Munn, and R. K. Jain, "Tumor microvasculature and microenvironment: Novel insights through intravital imaging in pre-clinical models," *Microcirculation* **17**(3), 206–225 (2010) [doi:10.1111/j.1549-8719.2010.00029.x].

[27] P. Amornphimoltham, A. Masedunskas, and R. Weigert, "Intravital microscopy as a tool to study drug delivery in preclinical studies," *Adv. Drug Deliv. Rev.* **63**(1–2), 119–128, Elsevier B.V. (2011) [doi:10.1016/j.addr.2010.09.009].

[28] G. M. Tozer, S. M. Ameer-Beg, J. Baker, P. R. Barber, S. A. Hill, R. J. Hodgkiss, R. Locke, V. E. Prise, I. Wilson, et al., "Intravital imaging of tumour vascular networks using multi-photon fluorescence microscopy," *Adv. Drug Deliv. Rev.* **57**(1 SPEC. ISS), 135–152 (2005) [doi:10.1016/j.addr.2004.07.015].

[29] R. Kiesslich, M. Goetz, M. Vieth, P. R. Galle, and M. F. Neurath, "Technology insight: confocal laser endoscopy for in vivo diagnosis of colorectal cancer.," *Nat. Clin. Pract. Oncol.* **4**(8), 480–490 (2007) [doi:10.1038/ncponc0881].

[30] P. Beard, "Biomedical photoacoustic imaging.," *Interface Focus* **1**(4), 602–631 (2011) [doi:10.1098/rsfs.2011.0028].

[31] X. Bai, X. Gong, W. Hau, R. Lin, J. Zheng, C. Liu, C. Zeng, X. Zou, H. Zheng, et al., "Intravascular optical-resolution photoacoustic tomography with a 1.1 mm diameter catheter.," *PLoS One* **9**(3), e92463 (2014) [doi:10.1371/journal.pone.0092463].

[32] B. Dong, S. Chen, Z. Zhang, C. Sun, and H. F. Zhang, "Photoacoustic probe using a microring resonator ultrasonic sensor for endoscopic applications," *Opt. Lett.* **39**(15), 4372 (2014) [doi:10.1364/OL.39.004372].

[33] K. Maslov, H. F. Zhang, S. Hu, and L. V Wang, "Optical-resolution photoacoustic microscopy for in vivo imaging of single capillaries.," *Opt. Lett.* **33**(9), 929–931 (2008).

[34] J.-M. Yang, C. Li, R. Chen, Q. Zhou, K. K. Shung, and L. V Wang, "Catheter-based photoacoustic endoscope.," *J. Biomed. Opt.* **19**(6), 66001 (2014) [doi:10.1117/1.JBO.19.6.066001].

[35] J. M. Cannata, T. a Ritter, W.-H. Chen, R. H. Silverman, and K. K. Shung, "Design of Efficient, Broadband Single-Element (20--80\,MHz) Ultrasonic Transducers for Medical Imaging Applications," *IEEE Trans. Ultrason. Ferroelectr. Freq. Control* **50**(11), 1548–1557 (2003).

[36] J. A. Jensen, D.- Lyngby, P. Medical, B. Engineering, and I. Technology, "Field : A Program for Simulating Ultrasound Systems Field : A Program for Simulating Ultrasound Systems," *Med. Biol. Eng.* **34**, 351–353 (1996).

[37] C. Li, J. Yang, R. Chen, Y. Zhang, Y. Xia, Q. Zhou, K. Kirk, and L. V Wang, "Photoacoustic endoscopic imaging study of melanoma tumor growth in a rat colorectum in vivo I- Endoscope," *Proc. SPIE* **8581**, 85810D (2013) [doi:10.1117/12.2005470].

[38] S. H. Yun, G. J. Tearney, B. J. Vakoc, M. Shishkov, W. Y. Oh, A. E. Desjardins, M. J. Suter, R. C. Chan, J. a Evans, et al., "Comprehensive volumetric optical microscopy in vivo.," *Nat. Med.* **12**(12), 1429–1433 (2006) [doi:10.1038/nm1450].

[39] Q. Zhou, X. Xu, E. J. Gottlieb, L. Sun, J. M. Cannata, H. Ameri, M. S. Humayun, P. Han, and K. K. Shung, "PMN-PT single crystal, high-frequency ultrasonic needle transducers for pulsed-wave Doppler application," *IEEE Trans. Ultrason. Ferroelectr. Freq. Control* **54**(3), 668–673 (2007) [doi:10.1109/TUFFC.2007.290].

[40] T. Ling, S.-L. Chen, and L. J. Guo, "Fabrication and characterization of high Q polymer micro-ring resonator and its application as a sensitive ultrasonic detector.," *Opt. Express* **19**(2), 861–869 (2011).

[41] L. Wang, C. Zhang, and L. V Wang, "Grueneisen Relaxation Photoacoustic Microscopy," 1–5 (2014) [doi:10.1103/PhysRevLett.113.174301].

[42] A. B. Karpiouk, B. Wang, and S. Y. Emelianov, "Development of a catheter for combined intravascular ultrasound and photoacoustic imaging," *Rev. Sci. Instrum.* **81**(1) (2010) [doi:10.1063/1.3274197].

[43] L. V. Wang, S. L. Jacques, and L. Zheng, "MCML-Monte Carlo modeling of light transport in multi-layered tissues," *Comput. Methods Programs Biomed.* **47**, 131–146 (1995).

[44] A. N. Bashkatov, E. A. Genina, V. I. Kochubey, and V. V Tuchin, "Optical properties of human skin, subcutaneous and mucous tissues in the wavelength range from 400 to 2000 nm," *J. Phys. D Appl. Phys* **38**, 2543–2555 (2005) [doi:10.1088/0022-3727/38/15/004].

[45] P. Lai, X. Xu, and L. V Wang, "Dependence of optical scattering from Intralipid in gelatin-gel based tissue-mimicking phantoms on mixing temperature and time.," *J. Biomed. Opt.* **19**(3), 35002 (2014) [doi:10.1117/1.JBO.19.3.035002].

[46] J. Zhang and D. Xing, "Intravascular photoacoustic detection of vulnerable plaque based on constituent selected imaging," *J. Phys. Conf. Ser.* **277**, 12049 (2011) [doi:10.1088/1742-6596/277/1/012049].

[47] E. Z. Zhang and P. C. Beard, "A miniature all-optical photoacoustic imaging probe," *Proc. SPIE* **7899**, 78991F–1–78991F–6 (2011) [doi:10.1117/12.874883].

[48] P. Hajireza, W. Shi, and R. Zemp, "Label-free in vivo GRIN-lens optical resolution photoacoustic micro-endoscopy," *Laser Phys. Lett.* **10**(5), 55603 (2013) [doi:10.1088/1612-2011/10/5/055603].

[49] J. Yao, C.-H. Huang, L. Wang, J.-M. Yang, L. Gao, K. I. Maslov, J. Zou, and L. V Wang, "Wide-field fast-scanning photoacoustic microscopy based on a water-immersible MEMS scanning mirror.," *J. Biomed. Opt.* **17**(8), 080505–1 (2012) [doi:10.1117/1.JBO.17.8.080505].

[50] E. a Reits and J. J. Neefjes, "From fixed to FRAP: measuring protein mobility and activity in living cells.," *Nat. Cell Biol.* **3**(6), E145-7 (2001) [doi:10.1038/35078615].

[51] J. Lippincott-Schwartz, E. Snapp, and a Kenworthy, "Studying protein dynamics in living cells.," *Nat. Rev. Mol. Cell Biol.* **2**(6), 444–456 (2001) [doi:10.1038/35073068].

[52] N. Klonis, M. Rug, I. Harper, M. Wickham, A. Cowman, and L. Tilley, "Fluorescence photobleaching analysis for the study of cellular dynamics," *Eur. Biophys. J.* **31**(1), 36–51 (2002) [doi:10.1007/s00249-001-0202-2].

[53] D. Axelrod, D. E. Koppel, J. Schlessinger, E. Elson, and W. W. Webb, "Mobility

measurement by analysis of fluorescence photobleaching recovery kinetics.," *Biophys. J.* **16**(9), 1055–1069, Elsevier (1976) [doi:10.1016/S0006-3495(76)85755-4].

[54]   G. H. Patterson and D. W. Piston, "Photobleaching in two-photon excitation microscopy.," *Biophys. J.* **78**(4), 2159–2162 (2000) [doi:10.1016/S0006-3495(00)76762-2].

[55]   R. Dixit and R. Cyr, "Cell damage and reactive oxygen species production induced by fluorescence microscopy: effect on mitosis and guidelines for non-invasive fluorescence microscopy," *Plant J.* **36**(2), 280–290 (2003) [doi:10.1046/j.1365-313X.2003.01868.x].

[56]   G. P. Luke, D. Yeager, and S. Y. Emelianov, "Biomedical applications of photoacoustic imaging with exogenous contrast agents.," *Ann. Biomed. Eng.* **40**(2), 422–437 (2012) [doi:10.1007/s10439-011-0449-4].

[57]   J. R. Cook, W. Frey, and S. Emelianov, "Quantitative photoacoustic imaging of nanoparticles in cells and tissues.," *ACS Nano* **7**(2), 1272–1280 (2013) [doi:10.1021/nn304739s].

[58]   S. Hu and L. V Wang, "Photoacoustic imaging and characterization of the microvasculature.," *J. Biomed. Opt.* **15**(1), 11101 (2010) [doi:10.1117/1.3281673].

[59]   C. Zhang, Y. S. Zhang, D.-K. Yao, Y. Xia, and L. V Wang, "Label-free photoacoustic microscopy of cytochromes.," *J. Biomed. Opt.* **18**(2), 20504 (2013) [doi:10.1117/1.JBO.18.2.020504].

[60]   D.-K. Yao, K. Maslov, K. K. Shung, Q. Zhou, and L. V Wang, "In vivo label-free photoacoustic microscopy of cell nuclei by excitation of DNA and RNA.," *Opt. Lett.* **35**(24), 4139–4141 (2010).

[61]   L. Gao, L. Wang, C. Li, A. Garcia-Uribe, and L. V Wang, "Photothermal bleaching in time-lapse photoacoustic microscopy.," *J. Biophotonics* **6**(6–7), 543–548 (2013) [doi:10.1002/jbio.201200184].

[62]   C. Zhang, K. Maslov, and L. V Wang, "Subwavelength-resolution label-free photoacoustic microscopy of optical absorption in vivo.," *Opt. Lett.* **35**(19), 3195–3197 (2010).

[63]   L. V. Wang, "Tutorial on Photoacoustic Microscopy and Computed Tomography," *IEEE J. Sel. Top. Quantum Electron.* **14**(1), 171–179 (2008) [doi:10.1109/JSTQE.2007.913398].

[64]   X. Yang and E. Stein, "Nanoparticles for photoacoustic imaging," *Wiley Interdiscip. ...* **1**(4), 360–368 (2009) [doi:10.1002/wnan.042].

[65]   K. T. Thurn, E. Brown, A. Wu, S. Vogt, B. Lai, J. Maser, T. Paunesku, and G. E. Woloschak, "Nanoparticles for applications in cellular imaging.," *Nanoscale Res. Lett.* **2**(9), 430–441 (2007) [doi:10.1007/s11671-007-9081-5].

[66]   H. G. Kapitza, G. McGregor, and K. a Jacobson, "Direct measurement of lateral transport

in membranes by using time-resolved spatial photometry.," *Proc. Natl. Acad. Sci.* **82**(12), 4122–4126 (1985).

[67] A. Einstein, "On the Movement of Small Particles Suspended in Stationary Liquids Required by the Molecular-Kinetic Theory of Heat," *Ann. Phys.* **17**, 549–560 (1905).

[68] K. Luby-Phelps, D. L. Taylor, and F. Lanni, "Probing the structure of cytoplasm.," *J. Cell Biol.* **102**(6), 2015–2022 (1986).

[69] R. Swaminathan, S. Bicknese, N. Periasamy, and a S. Verkman, "Cytoplasmic viscosity near the cell plasma membrane: translational diffusion of a small fluorescent solute measured by total internal reflection-fluorescence photobleaching recovery.," *Biophys. J.* **71**(2), 1140–1151, Elsevier (1996) [doi:10.1016/S0006-3495(96)79316-5].

[70] S. Y. Nam, L. M. Ricles, L. J. Suggs, and S. Y. Emelianov, "Nonlinear photoacoustic signal increase from endocytosis of gold nanoparticles.," *Opt. Lett.* **37**(22), 4708–4710 (2012).

[71] H. Y. Nam, S. M. Kwon, H. Chung, S.-Y. Lee, S.-H. Kwon, H. Jeon, Y. Kim, J. H. Park, J. Kim, et al., "Cellular uptake mechanism and intracellular fate of hydrophobically modified glycol chitosan nanoparticles.," *J. Control. Release* **135**(3), 259–267, Elsevier B.V. (2009) [doi:10.1016/j.jconrel.2009.01.018].

[72] H.-H. Chen, C.-C. Chien, C. Petibois, C.-L. Wang, Y. S. Chu, S.-F. Lai, T.-E. Hua, Y.-Y. Chen, X. Cai, et al., "Quantitative analysis of nanoparticle internalization in mammalian cells by high resolution X-ray microscopy.," *J. Nanobiotechnology* **9**(1), 14, BioMed Central Ltd (2011) [doi:10.1186/1477-3155-9-14].

[73] R. Lévy, U. Shaheen, Y. Cesbron, and V. Sée, "Gold nanoparticles delivery in mammalian live cells: a critical review.," *Nano Rev.* **1**, 1–18 (2010) [doi:10.3402/nano.v1i0.4889].

[74] H. Ba, J. Rodríguez-Fernández, F. D. Stefani, and J. Feldmann, "Immobilization of gold nanoparticles on living cell membranes upon controlled lipid binding.," *Nano Lett.* **10**(8), 3006–3012 (2010) [doi:10.1021/nl101454a].

[75] Y.-S. Chen, W. Frey, S. Kim, P. Kruizinga, K. Homan, and S. Emelianov, "Silica-coated gold nanorods as photoacoustic signal nanoamplifiers.," *Nano Lett.* **11**(2), 348–354 (2011) [doi:10.1021/nl1042006].

[76] W. Lu, Q. Huang, G. Ku, X. Wen, M. Zhou, D. Guzatov, P. Brecht, R. Su, A. Oraevsky, et al., "Photoacoustic imaging of living mouse brain vasculature using hollow gold nanospheres," *Biomaterials* **31**(9), 2617–2626, Elsevier Ltd (2010) [doi:10.1016/j.biomaterials.2009.12.007].

[77] R. H. Belmaker, "Bipolar disorder," *N.Engl.J.Med.* **351**(5), 476–486 (2004) [doi:10.1136/bmj.e8508].

[78] J. M. Dubach, E. Lim, N. Zhang, K. P. Francis, and H. Clark, "In vivo sodium concentration continuously monitored with fluorescent sensors.," *Integr. Biol. (Camb).*

3(2), 142–148 (2011) [doi:10.1039/c0ib00020e].

[79] J. Xia, M. R. Chatni, K. Maslov, Z. Guo, K. Wang, M. Anastasio, and L. V Wang, "Whole-body ring-shaped confocal photoacoustic computed tomography of small animals in vivo.," *J. Biomed. Opt.* **17**(5), 50506 (2012) [doi:10.1117/1.JBO.17.5.050506].

[80] J. Gamelin, A. Maurudis, A. Aguirre, F. Huang, P. Guo, L. V Wang, and Q. Zhu, "A real-time photoacoustic tomography system for small animals.," *Opt. Express* **17**(13), 10489–10498 (2009).

[81] K. H. Song and L. V Wang, "Deep reflection-mode photoacoustic imaging of biological tissue.," *J. Biomed. Opt.* **12**(6), 60503 (2007) [doi:10.1117/1.2818045].

[82] J. M. Dubach, S. Das, A. Rosenzweig, and H. a Clark, "Visualizing sodium dynamics in isolated cardiomyocytes using fluorescent nanosensors.," *Proc. Natl. Acad. Sci. U. S. A.* **106**(38), 16145–16150 (2009) [doi:10.1073/pnas.0905909106].

[83] K. J. Cash and H. A. Clark, "In vivo histamine optical nanosensors," *Sensors (Switzerland)* **12**(9), 11922–11932 (2012) [doi:10.3390/s120911922].

[84] E. Bakker, P. Buehlmann, and E. Pretsch, "Carrier-Based Ion-Selective Electrodes and Bulk Optodes. 1. General Characteristics.," *Chem. Rev. (Washington, D. C.)* **97**(8), 3083–3132 (1997) [doi:10.1021/CR940394A].

[85] P. Bühlmann, E. Pretsch, and E. Bakker, "Carrier-based ion-selective electrodes and bulk optodes. 2. Ionophores for potentiometric and optical sensors," *Chem. Rev.* **98**(4), 1593–1688 (1998) [doi:cr970113+ [pii]].

[86] K. Kimura, S. Kitazawa, and T. Shono, "Synthesis and Selectivity for Lithium of Lipophilic 14-Crown-4 Derivatives bearing Bulky Substituents or an Additional Binding Site in the Side Arm," 1945–1951 (1986).

[87] P. E. Keck and S. L. Mcelroy, "Clinical pharmacodynamics and pharmacokinetics of antimanic and mood-stabilizing medications," *J. Clin. Psychiatry* **63**(4), 3–11 (2001).

[88] A. J. Wood, G. M. Goodwin, R. De Souza, and A. R. Green, "The pharmacokinetic profile of lithium in rat and mouse; An important factor in psychopharmacological investigation of the drug," *Neuropharmacology* **25**(11), 1285–1288 (1986) [doi:10.1016/0028-3908(86)90149-8].

[89] B. P. Kovatchev, D. Shields, and M. Breton, "Graphical and numerical evaluation of continuous glucose sensing time lag.," *Diabetes Technol. Ther.* **11**(3), 139–143 (2009) [doi:10.1089/dia.2008.0044].

[90] C. Li, J.-M. Yang, R. Chen, C.-H. Yeh, L. Zhu, K. Maslov, Q. Zhou, K. K. Shung, and L. V Wang, "Urogenital photoacoustic endoscope.," *Opt. Lett.* **39**(6), 1473–1476 (2014).

[91] J. Yang, C. Li, R. Chen, B. Rao, J. Yao, C. Yeh, A. Danielli, K. Maslov, Q. Zhou, et al., "Optical-resolution photoacoustic endomicroscopy in vivo," 362–364 (2015) [doi:10.1364/BOE.6.000918].

[92]   C. Li, C. Zhang, L. Gao, A. Garcia-Uribe, and L. V. Wang, "Photothermal bleaching and recovery analysis in photoacoustic microscopy," A. A. Oraevsky and L. V. Wang, Eds., 89435Q (2014) [doi:10.1117/12.2040936].

[93]   K. J. Cash, C. Li, J. Xia, L. V Wang, H. A. Clark, and C. E. T. Al, "Optical Drug Monitoring : Photoacoustic Imaging of Nanosensors to Monitor Therapeutic Lithium in Vivo," *ACS Nano* **9**(2), 1692–1698 (2015).

Vita

Chiye Li

Degrees

Ph.D., Biomedical Engineering
Washington University in St. Louis
December 2016

B.S., Biophysics
University of Science and Technology of China
June 2011

Publications

1. P. Hai, J. Yao, G. Li, **C. Li**, and L. V. Wang, "Photoacoustic elastography," *Optics Letters*, **41**(4), 725-728 (2016).

2. J.-M. Yang, **C. Li**, R. Chen, B. Rao, J. Yao, C.-H. Yeh, A. Danielli, K. Maslov, Q. Zhou, K. K. Shung, and L. V. Wang, "Optical-resolution photoacoustic endomicroscopy *in vivo*," *Biomedical Optics Express* **23**(4), 362–364 (2015).

3. K. J. Cash, **C. Li**, J. Xia, L. V. Wang, and H. A. Clark, "Optical Drug Monitoring∶ Photoacoustic Imaging of Nanosensors to Monitor Therapeutic Lithium *in vivo*," *ACS Nano* **9**(2), 1692–1698 (2015).

4. J. Liang, L. Gao, P. Hai, **C. Li**, and L. V. Wang, "Encrypted Three-dimensional Dynamic Imaging using Snapshot Time-of-flight Compressed Ultrafast Photography," *Scientific Report* **5**, 15504 (2015).

5. Y. Zhou, G. Li, L. Zhu, **C. Li**, L. A. Cornelius, and L. V. Wang, "Handheld photoacoustic probe to detect both melanoma depth and volume at high speed *in vivo*," *Journal of Biophotonics*, 1-7 (2015).

6. P. Hai, Y. Zhou, J. Liang, **C. Li**, and L. V. Wang, "Photoacoustic tomography of vascular compliance in humans," *Journal of Biomedical Optics*, **20**(12), 126008 (2015).

7. **<u>C. Li</u>**, J.-M. Yang, R. Chen, C.-H. Yeh, L. Zhu, K. I. Maslov, Q. Zhou, K. K. Shung, and L. V. Wang, "Urogenital photoacoustic endoscope," *Optics Letters* **39**(6), 1473–1476 (2014).

8. J.-M. Yang, **<u>C. Li</u>**, R. Chen, Q. Zhou, K. K. Shung, and L. V. Wang, "Catheter-based photoacoustic endoscope," *Journal of Biomedical Optics* **19**(6), 066001 (2014).

9. L. Gao, J. Liang, **<u>C. Li</u>**, and L. V. Wang, "Single-shot compressed ultrafast photography at one hundred billion frames per second," *Nature* **516**(7529), 74–77 (2014).

10. J. Yao, L. Wang, **<u>C. Li</u>**, C. Zhang, and L. V. Wang, "Photoimprint photoacoustic microscopy for three-dimensional label-free subdiffraction imaging," *Physical Review Letters* **112**(1), 014302 (2014).

11. L. Gao, L. Zhu, **<u>C. Li</u>**, and L. V. Wang, "Nonlinear light-sheet fluorescence microscopy by photobleaching imprinting," *Journal of the Royal Society Interface* **11**, 20130851 (2014).

12. J. Liang, L. Gao, **<u>C. Li</u>**, and L. V. Wang, "Spatially Fourier-encoded photoacoustic microscopy using a digital micromirror device," *Optics Letters,* **39**, 430-433 (2014).

13. A. Danielli, K. Maslov, A. Garcia-Uribe, A. M. Winkler, **<u>C. Li</u>**, L. Wang, Y. Chen, G. W. Dorn, and L. V. Wang, "Label-free photoacoustic nanoscopy.," *Journal of Biomedical Optics*, **19**(8), 86006 (2014).

14. **<u>C. Li</u>**, C. Zhang, L. Gao, A. Garcia-Uribe, and L. V. Wang, "Photoacoustic recovery after photothermal bleaching in living cells," *Journal of Biomedical Optics* **18**(10), 106004 (2013).

15. **<u>C. Li</u>**, L. Gao, Y. Liu, and L. V. Wang, "Optical sectioning by wide-field photobleaching imprinting microscopy," *Applied Physics Letters* **103**(18), 183703 (2013).

16. L. Gao, C. Zhang, **<u>C. Li</u>**, and L. V. Wang, "Intracellular temperature mapping with fluorescence assisted photoacoustic thermometry," *Applied Physics Letters* **102**(19), 193705 (2013).

17. L. Gao, A. Garcia-Uribe, Y. Liu, **<u>C. Li</u>**, and L. V. Wang, "Photobleaching imprinting microscopy: seeing clearer and deeper," *Journal of Cell Science* **126**(23), 142943 (2013).

18. L. Gao, L. Wang, **<u>C. Li</u>**, A. Garcia-Uribe, and L. V. Wang, "Photothermal bleaching in time-lapse photoacoustic microscopy," *Journal of Biophotonics* **6**(6-7), 543–548 (2013).

19. C. Zhang, Y. Zhou, **<u>C. Li</u>**, and L. V. Wang, "Slow-sound photoacoustic microscopy," *Applied Physics Letters* **102**(16), 163702 (2013).

20. J. Liang, Y. Zhou, A. W. Winkler, L. Wang, K. I. Maslov, **C. Li**, and L. V. Wang, "Random-access optical-resolution photoacoustic microscopy using a digital micromirror device," *Optics Letters* **38**(15), 2683–2686 (2013).

21. J.-M. Yang, R. Chen, C. Favazza, J. Yao, **C. Li**, Z. Hu, Q. Zhou, K. K. Shung, and L. V. Wang, "A 2.5-mm diameter probe for photoacoustic and ultrasonic endoscopy," *Optics Express* **20**(21), 23944–23953 (2012).

22. L. Gao, L. Wang, **C. Li**, Y. Liu, H. Ke, C. Zhang, and L. V. Wang, "Single-cell photoacoustic thermometry," *Journal of Biomedical Optics* **18**(2), 026003 (2012).